THE HONG KONG
POLYTECHNIC UNIVERSITY
香港理工大學
Pao Yue-kong Library
包玉剛圖書館

## Copyright Undertaking

This thesis is protected by copyright, with all rights reserved.

**By reading and using the thesis, the reader understands and agrees to the following terms:**

1. The reader will abide by the rules and legal ordinances governing copyright regarding the use of the thesis.
2. The reader will use the thesis for the purpose of research or private study only and not for distribution or further reproduction or any other purpose.
3. The reader agrees to indemnify and hold the University harmless from and against any loss, damage, cost, liability or expenses arising from copyright infringement or unauthorized usage.

If you have reasons to believe that any materials in this thesis are deemed not suitable to be distributed in this form, or a copyright owner having difficulty with the material being included in our database, please contact lbsys@polyu.edu.hk providing details. The Library will look into your claim and consider taking remedial action upon receipt of the written requests.

Pao Yue-kong Library, The Hong Kong Polytechnic University, Hung Hom, Kowloon, Hong Kong

http://www.lib.polyu.edu.hk

# MICROWAVE PROPERTIES OF BARIUM STRONTIUM TITANATE THIN FILMS

SUBMITTED BY

**CHENG YIN LAI**

A THESIS SUBMITTED IN PARTIAL FULFILMENT OF THE REQUIREMENTS FOR THE DEGREE OF MASTER OF PHILOSOPHY IN PHYSICS

AT

**THE DEPARTMENT OF APPLIED PHYSICS**

**THE HONG KONG POLYTECHNIC UNIVERSITY**

JULY 2003

Pao Yue-kong Library
PolyU • Hong Kong

# CERTIFICATE OF ORIGINALITY

I hereby declare that this thesis is my own work and that, to the best of my knowledge and belief, it reproduces no material previously published or written nor material which has been accepted for the award of any other degree or diploma, except where due acknowledgement has been made in the text.

________________________(Signed)

CHENG YIN LAI (Name of student)

# Abstract


In recent years, barium strontium titanate (abbreviated as BST) thin films have attracted extensive research interest because their relative permittivity can be tuned by the application of an external bias field and can be used in agile microwave devices. In this work, $Ba_{0.7}Sr_{0.3}Ti_{0.95}O_3$ and $Ba_{0.5}Sr_{0.5}TiO_3$ thin films prepared by the sol-gel and magnetron sputtering methods have been studied.

X-ray diffraction (XRD) and atomic force microscopy (AFM) observations revealed that the films were well crystallized with uniform thickness. Coplanar electrodes were then deposited by magnetron sputtering and patterned by standard photolithography and wet chemical etching techniques.

The processing-structure-property relationship of BST thin film–based interdigital capacitors was investigated and compared with the conventional parallel plate capacitors and consistent results have been obtained. The films annealed at higher temperature possessed larger relative permittivity and the relative permittivity was also found to be dependent on the film thickness. The films prepared under optimized conditions exhibited good dielectric properties at microwave frequencies.

To find the properties of BST thin films with interdigital capacitors structure at high frequency, a simple measurement technique has been developed to remove the

parasitic capacitance. Several technical issues in the characterization of interdigital capacitors are discussed.

The dielectric tunability of BST thin films in interdigital capacitors was characterized. Under a 20 MV/m electric field, the tunability of BST on LAO substrate was found to be about 31%. Many processing factors were found to have influences on the tunability of the films. The relative permittivity and tunability of BST exhibited a strong dependence on film thickness.

BST film-based microwave devices, such as resonators and phase shifters were prepared and tested. The performance of ring resonator with different structures (substrates and film thicknesses) were investigated and studied with the aid of a commercial simulation software IE3D. Also, a BST thin film-based phase shifter under dc bias has been developed and preliminary measurement results have been obtained.

# Acknowledgements


I would like to acknowledge the support from Prof. Helen Chan, my supervisor, for her advice and supervision during the period of my study.

I would like to express my thanks to Dr. N. Chong for his assistance in the design and compliation of the program for calculating the permittivity from IDE measurements. His helpful suggestions are also appreciated.

I would like to express my appreciation to Dr. Y. Wang for the technical and theoretical assistance in my research work.

I would like to thank Dr. J. Z. Liu for his technical help in the microwave measurements and the assistance in the IE3D simulation on the ring resonators.

I would like to give my thanks to colleagues and friends in AP for their help and assistance.

This study was supported by the Centre For Smart Materials of The Hong Kong Polytechnic University.

# Acronyms

| | |
|---|---|
| XRD | X-ray diffraction |
| AFM | Atomic force microscopy |
| PLD | Pulsed laser ablation deposition |
| CVD | Chemical vapour deposition |
| CSD | Chemical solution deposition |
| PVD | Physical vapour deposition |
| RF | Radio frequency |
| PSPD | Position-sensitive photodetector |
| ISS | Impedance standard substrates |
| DUT | Device under test |
| RTP | Rapid thermal processor |
| VLF | Very low frequency |
| LF | Low frequency |
| MF | Medium frequency |
| HF | High frequency |
| VHF | Very high frequency |
| UHF | Ultra high frequency |
| SHF | Super high frequency |
| EHF | Extra high frequency |
| IR | Infrared |

# Table of contents

**Abstract** ........ i

**Acknowledgements** ........ iii

**Acronyms** ........ iv

**Table of contents** ........ v

**List of figures** ........ x

**List of tables** ........ xv

**Chapter 1 Introduction** ........ 1-1

1.1 Background and motivation ........ 1-1

1.2 Methodology ........ 1-2

1.3 Scope and outline of the thesis ........ 1-4

1.4 Original contributions ........ 1-5

**Chapter 2 Literature review** ........ 2-1

2.1 Introduction ........ 2-1

2.2 Ferroelectricity ........ 2-2

2.3 Structure and property of BST ........ 2-5

2.3.1 Bulk BST ........ 2-5

2.3.2 BST thin films ........ 2-8

2.3.2.1 Thin film fabrication ........ 2-8

2.3.2.2 Compositional dependence .............................. 2-8

2.3.2.3 Extrinsic influences on BST structure and properties .............................................. 2-10

2.4 Introduction to microwave technology .................................. 2-11

**Chapter 3 Fabrication and characterization of BST thin films and electrode patterning** .................................................. 3-1

3.1 Introduction ............................................................... 3-1

3.2 Thin film deposition ..................................................... 3-2

3.2.1 Radio frequency magnetron sputtering .......................... 3-2

3.2.1.1 Setup ........................................................ 3-2

3.2.1.2 Structural characterization ............................... 3-6

3.2.2 Sol gel deposition ................................................ 3-12

3.2.2.1 Process flow ............................................... 3-12

3.2.2.2 Structural characterization ............................... 3-14

3.3 Electrode patterning ..................................................... 3-16

3.3.1 Electrode deposition .............................................. 3-16

3.3.2 Photolithography .................................................. 3-17

3.3.2.1 Basic tool for the photolithography ..................... 3-17

3.3.2.2 Process of the photolithography ........................ 3-19

3.4 Summary ................................................................... 3-22

5.3 Typical value of dielectric tunability of BST and factors that affect the tunability .......... 5-11

5.3.1 Assessment of the dielectric tunability of BST .......... 5-11

5.3.2 Factors affecting the tunability of BST .......... 5-13

5.3.2.1 Substrate effect .......... 5-13

5.3.2.2 Dielectric tunability of BST prepared by the sol-gel method .......... 5-17

5.3.2.3 Tunability as a function of electrode spacing .......... 5-18

5.4 Dependence of BST tunability on film thickness .......... 5-20

5.5 Summary .......... 5-22

**Chapter 6 BST thin film-based microwave devices** .......... 6-1

6.1 Introduction .......... 6-1

6.2 Issues on microwave measurement .......... 6-2

6.2.1 Important issues before calibration .......... 6-2

6.2.2 Calibration of the system .......... 6-2

6.2.3 S-parameters .......... 6-3

6.3 Microwave devices .......... 6-6

6.3.1 Ring resonator .......... 6-6

6.3.1.1 Basic principle .......... 6-6

6.3.1.2 Ring resonator on a single crystal substrate .......... 6-8

6.3.1.3 Resonant frequency vs film thickness .......... 6-11

6.3.2 Phase shifter .......... 6-15

6.3.2.1 Basic principle.............................................. 6-15

6.3.2.2 Phase shifter on BST thin film............................ 6-17

6.4 Summary.............................................................. 6-19

**Chapter 7 Conclusions**.............................................. 7-1

7.1 Conclusions.......................................................... 7-1

7.2 Suggestions for future work.................................... 7-4

**References**.............................................................. R-1

**List of publications**................................................... P-1

**Appendix**................................................................. A-1

# List of figures

| | | Page |
|---|---|---|
| Figure 2.2.1 | Categories of dielectrics. | 2-3 |
| Figure 2.2.2(a) | Structure of $BaTiO_3$ above $T_c$. | 2-4 |
| Figure 2.2.2(b) | Structure of $BaTiO_3$ below $T_c$. | 2-4 |
| Figure 2.3.1 | Schematic lattice structure of $(Ba, Sr)TiO_3$. | 2-6 |
| Figure 2.3.2(a) | Lattice symmetry of BST as a function of Ba:Sr ratio. | 2-7 |
| Figure 2.3.2(b) | Curie temperature of BST as a function of Ba:Sr ratio. | 2-7 |
| Figure 2.3.3(a) | Lattice parameters against x in $Ba_xSr_{1-x}TiO_3$ for film and bulk ceramics. | 2-9 |
| Figure 2.3.3(b) | Curie temperature against x in $Ba_xSr_{1-x}TiO_3$ for film (triangle) and bulk ceramics (circle). | 2-10 |
| Figure 2.4.1 | The electromagnetic spectrum. | 2-12 |
| Figure 2.4.2 | Top view of the thin film-based device. | 2-13 |
| Figure 2.4.3 | Results of the thin film-based resonator under a dc bias. | 2-13 |
| Figure 3.2.1(a) | Schematic setup of the magnetron sputtering system. | 3-3 |
| Figure 3.2.1(b) | Photograph of the magnetron sputtering system. | 3-4 |
| Figure 3.2.2 | Schematic diagram of the basic principle of XRD. | 3-7 |
| Figure 3.2.3 | Schematic diagram of the basic principle of AFM. | 3-8 |
| Figure 3.2.4(a) | XRD of the as-deposited BST film. | 3-9 |
| Figure 3.2.4(b) | AFM micrograph of the as-deposited BST film. | 3-9 |
| Figure 3.2.5(a) | XRD of the annealed BST film. | 3-10 |
| Figure 3.2.5(b) | AFM micrograph of the annealed BST film. | 3-10 |
| Figure 3.2.6 | XRD of the BST film without substrate heating during deposition. | 3-11 |
| Figure 3.2.7 | AFM morphology of the BST film with 1100°C annealing. | 3-12 |
| Figure 3.2.8 | Flow chart of the sol gel method. | 3-14 |

Figure 3.2.9(a) XRD of BST film on Pt/Si annealed at 550°C. 3-15

Figure 3.2.9(b) XRD of BST film on Pt/Si annealed at 650°C. 3-15

Figure 3.3.1 Structure of the sample after electrode deposition. 3-17

Figure 3.3.2 Photograph of the mask used in the photolithography. 3-19

Figure 3.3.3 Process flow of the photolithographic technique. 3-19

Figure 3.3.4 Schematic diagram of the sample at each step. 3-21

Figure 3.3.5 Side and top views of the sample. 3-22

Figure 4.2.1(a) Schematic structure of an interdigital electrode (IDE). 4-4

Figure 4.2.1(b) Schematic structure of the open reference. 4-4

Figure 4.2.1(c) Schematic structure of the short reference. 4-4

Figure 4.2.2 Measurement instruments: network analyzer and probe station. 4-5

Figure 4.2.3 Equivalent circuit of the IDE with the parasitics to be de-embedded. 4-7

Figure 4.2.4 A planar view of an IDC for the partial capacitance technique. 4-9

Figure 4.2.5 Schematic diagram of the partial capacitance technique for a multilayer sample. 4-10

Figure 4.2.6(a) A periodical structure of IDC. 4-11

Figure 4.2.6(b) A periodical structure of IDC transfer to Z-plane. 4-11

Figure 4.2.6(c) A periodical structure of IDC: Z-plane to T-plane. 4-11

Figure 4.2.6(d) A periodical structure of IDC: T-plane to W-plane. 4-11

Figure 4.2.7 Considerations for the end capacitors. 4-12

Figure 4.3.1(a) Raw data |Z| of open, short references and IDE of BST/LAO as a function of frequency. 4-14

Figure 4.3.1(b) Capacitance of the main IDC of BST/LAO as a function of frequency. 4-14

Figure 4.3.2 Relative permittivity of BST film as a function of frequency. 4-16

| | | |
|---|---|---|
| Figure 4.3.3(a) | Cross-sectional views of the sample: IDC-Z. | 4-17 |
| Figure 4.3.3(b) | Cross-sectional views of the sample: parallel plate capacitor. | 4-17 |
| Figure 4.3.4 | Relative permittivity of BST as a function of annealing temperature at 10 MHz. | 4-18 |
| Figure 4.3.5 | The influence of film thickness on the relative permittivity of BST on $ZrO_2$ and Pt-Si at 10 MHz. | 4-20 |
| Figure 4.4.1 | Layered structure and parameters for the calculation. | 4-21 |
| Figure 4.4.2 | The changes of the capacitance due to the change in electrode thickness. | 4-22 |
| Figure 4.4.3 | The dependence of the geometric factor on the finger gap in the IDCs. | 4-23 |
| Figure 4.4.4 | The dependence of capacitance on the film thickness in the IDCs. | 4-24 |
| Figure 5.1.1(a) | Dependence of $\varepsilon$ on dc bias in ferroelectric materials below $T_c$. | 5-2 |
| Figure 5.1.1(b) | Dependence of $\varepsilon$ on dc bias in ferroelectric materials above $T_c$. | 5-2 |
| Figure 5.2.1 | BST film-based IDC under test. | 5-6 |
| Figure 5.2.2 | Extraction of the capacitance of the ferroelectric film. | 5-7 |
| Figure 5.2.3(a) | The C-E dependence of interdigital capacitors of IDE/BST/LAO. | 5-8 |
| Figure 5.2.3(b) | The C-E dependence of interdigital capacitors of IDE/LAO. | 5-9 |
| Figure 5.2.3(c) | The C-E dependence of interdigital capacitors of IDE/film (virtual). | 5-9 |
| Figure 5.3.1(a) | Typical dielectric behaviour of BST in the capacitor IDE/BST/LAO: the relative permittivity. | 5-11 |
| Figure 5.3.1(b) | Typical dielectric behaviour of BST in the capacitor IDE/BST/LAO: the tunability. | 5-12 |

Figure 5.3.2 The experimental data (line) vs the calculated results (square dots). 5-12
Figure 5.3.3 The dielectric tunability of BST on different substrates: LAO and MgO. 5-14
Figure 5.3.4(a) XRD of BST on MgO. 5-16
Figure 5.3.4(b) XRD of BST on LAO. 5-16
Figure 5.3.5 The dielectric tunability of sol-gel BST (50/50) on LAO. 5-17
Figure 5.3.6(a) BST tunability in IDE/BST/LAO with different electrode spacings under different dc bias voltages. 5-19
Figure 5.3.6(b) BST tunability in IDE/BST/LAO with different electrode spacings under different electric fields. 5-19
Figure 5.4.1(a) Influence of film thickness on the relative permittivity of BST in IDE/BST/LAO. 5-21
Figure 5.4.1(b) Influence of film thickness on the tunability of BST in IDE/BST/LAO. 5-21
Figure 6.2.1(a) Photograph of the GSG microprobe. 6-4
Figure 6.2.1(b) Photograph of the GSG microprobe tips. 6-4
Figure 6.2.1(c) Photograph of the GSG microprobe marks on the contact substrate. 6-4
Figure 6.2.2 Two-port network analyzer model (Forward Model). 6-4
Figure 6.2.3 Different calibration steps: microprobe placed on different standard substrates: (open→load→short→thru). 6-4
Figure 6.2.4 Detail information of S-parameters and device characterization. 6-5
Figure 6.3.1 A ring resonator. 6-6
Figure 6.3.2(a) Cross section of the sample. 6-8
Figure 6.3.2(b) Top view of the sample. 6-8
Figure 6.3.3 Experimental setup of the ring resonator measurement. 6-9

| | | |
|---|---|---|
| Figure 6.3.4 | S-parameter against frequency of resonators on LAO and MgO. | 6-9 |
| Figure 6.3.5 | Calculated relative permittivity at different resonant frequencies. | 6-11 |
| Figure 6.3.6 | Film thickness dependence of the resonant frequency. | 6-12 |
| Figure 6.3.7 | Experimental data and simulation results of ring resonator on the 300 nm sputtered BST thin film/LAO/Au. | 6-14 |
| Figure 6.3.8 | Schematic diagram of the eight coupled microstrip phase shifter design (W = 25μm and s = 8μm). | 6-16 |
| Figure 6.3.9 | A coupled microstrip ferroelectric phase shifter. The E-fields are drawn for odd mode propagation [49]. | 6-16 |
| Figure 6.3.10 | Phase shift vs frequency for different dc bias. | 6-18 |
| Figure 6.3.11 | Differential phase shift vs dc bias at different frequencies. | 6-18 |

# List of tables

| | | Page |
|---|---|---|
| Table 2.1 | Dielectric properties of BST thin film on LAO and MgO substrates. | 2-11 |
| Table 3.1 | Lattice parameters and thermal expansion coefficients of BST and the substrates. | 3-5 |
| Table 3.2 | Conditions of the BST deposition. | 3-5 |
| Table 3.3 | Conditions of the gold deposition. | 3-16 |
| Table 5.1 | Calculated tunability from two different methods. | 5-10 |
| Table 5.2 | Lattice parameter (a) and thermal expansion coefficients ($\alpha$) of bulk BST and the substrates. | 5-15 |
| Table 5.3 | Dielectric properties of BST films with different thicknesses. | 5-20 |
| Table 6.1 | Resonant frequencies of several modes. | 6-10 |
| Table 6.2 | Several resonant modes. | 6-12 |

# Chapter 1

# Introduction

## 1.1 Background and motivation

Barium strontium titanate ($Ba_xSr_{1-x}TiO_3$, abbreviated as BST) is a solid solution of barium titanate ($BaTiO_3$) and strontium titanate ($SrTiO_3$). BST ceramics have been studied and used in ceramic capacitors for several decades. [1-13] BST thin films have also attracted extensive research interest particularly in recent years because of their potential applications in tunable microwave devices [1-6] for wireless communications. The explosion in wireless communication has fueled and is fueling the study and development of BST thin films and devices.

The most important feature of BST thin films is that, in certain BST compositions, their dielectric property is very sensitive to the presence of external electric field, a characteristics called “dielectric tunability”. This tunability is an intrinsic property of BST and can be observed in BST at frequencies up to the microwave regime. Because of this feature, capacitive devices using BST thin films can be conveniently “tuned” by changing the applied dc bias voltage. For example, the centre frequency of a BST filter can be shifted by simply changing the dc bias voltage. Comparing with conventional technology which uses several filters with

fixed-frequency components, the use of BST tunable filters can lower the cost. Naturally the thin film technology is also critically important because it provides a higher level of integration and miniaturization than that can be achieved with discrete components.

Although it is known that BST thin films are well suited for tunable microwave circuit, the successful deployment of the devices in commercial systems still requires a better understanding of the mechanisms that govern their microwave properties in order to improve the device performance. It is equally important to develop test procedures and device configurations to provide accurate information about the film properties at high frequencies.

This thesis focusses on the development and the microwave characterization of BST thin films and BST-based devices such as resonators and phase shifters.

## 1.2 Methodology

BST thin films were mainly prepared by two techniques: the radio frequency magnetron sputtering and sol gel methods. The phase and orientation of the films were characterized by X-ray diffraction (XRD) and the morphology was measured using atomic force microscopy (AFM). Standard microelectronic fabrication

techniques including photolithography and chemical etching were used to define the electrode patterns for the samples and devices under test.

In this study, the compositions of the BST thin film used were $Ba_{0.5}Sr_{0.5}TiO_3$ and $Ba_{0.7}Sr_{0.3}Ti_{0.95}O_3$. Both $Ba_{0.5}Sr_{0.5}TiO_3$ and $Ba_{0.7}Sr_{0.3}Ti_{0.95}O_3$ thin films have paraelectric phase at room temperature. $Ba_{0.5}Sr_{0.5}TiO_3$ thin film was suitable for high frequency applications because of its outstanding dielectric properties [3-5]. On the other hand, the relative permittivity of $Ba_{0.7}Sr_{0.3}Ti_{0.95}O_3$ thin film showed little dependence on the magnitude of external ac field (obtained from dielectric tests on parallel plate capacitors). This feature [14] is important for the investigation of the processing-structure-property relationship of BST thin film-based interdigital capacitor (details are given in Chapter 4). Because a strong ac field dependence of the relative permittivity in the film will increase the complexity in the dielectric tests.

The samples for microwave measurements have two different configurations: 1) conventional parallel plate capacitor and 2) coplanar capacitor. The major part of work in this thesis rested on the second structure because most microwave devices have coplanar structures. Interdigital electrodes are important electrode forms. Devices with other electrode patterns such as ring resonators and phase shifters have also been fabricated and tested.

To characterize the properties of BST thin films and devices at microwave frequencies, an Agilent 8720ES network analyzer (Agilent, USA) together with a RF-1 Microwave Probe Station (Cascade Microtech, USA) were used in the measurement. From the measurement results, the material properties and the device performance at microwave frequencies were extracted.

## 1.3 Scope and outline of the thesis

The main objective of our study was to fabricate and characterize BST thin films and related microwave devices. The microwave properties of BST thin film were first extracted which helped to optimize the film fabrication process. Also, the structure-property relationship of the BST thin film-based interdigital capacitor was studied. Based on these results, devices such as ring resonators were fabricated and characterized.

Chapter 2 presented a short literature review. Fundamental of ferroelectricity, structure and property of BST and introduction to microwave technology were outlined in this Chapter.

In Chapter 3, the processes of BST thin film depositions and the electrode patterning were described.

Chapter 4 focussed on the dielectric characterization of BST thin films. Extraction of the relative permittivity of BST thin film using a coplanar capacitor structure was described.

Chapter 5 focussed on the dielectric tunability of BST thin films in the coplanar capacitors. The influences of substrate, film thickness and electrode sizes on the tunability were discussed.

Chapter 6 demonstrated the structures and performances of BST thin film-based microwave devices.

Chapter 7 gave a summary and suggestions for future work.

## 1.4 Original contributions

In this thesis, original contributions are:

(1) Investigations on the processing-structure-property relationship in the BST thin film-based interdigital capacitors and comparing the results with the conventional parallel plate capacitors. As the field distribution in the films of a coplanar device is quite different from that in a parallel plate capacitor. Our work provides a good reference

for the study and development of novel ferroelectric film-based coplanar devices.

(2) Extraction of the dielectric properties of BST thin films at microwave frequencies by interdigital capacitors. Most of the literatures focussed on the low frequency range with the conventional parallel plate capacitor structure.

(3) A simple measurement technique (equivalent circuits of interdigital electrode, open and short references) has been developed for removing the parasitic capacitance of the interdigital electrode structure at high frequency measurements to obtain the dielectric properties of the BST thin films.

# Chapter 2

# Literature review

## 2.1 Introduction

In recent years, there has been considerable research interest in the fabrication and characterization of barium strontium titanate ($Ba_xSr_{1-x}TiO_3$, abbreviated as BST)) thin films mainly due to their potential applications in tunable microwave components and devices [3-5]. The special feature of BST for these applications is that the relative permittivity of BST is sensitive to external dc bias i.e., the capacitance of a BST-based capacitor can be electrically tuned. Hence the performance (e.g., the resonant frequency) of an electronic circuit using such capacitors, particularly those used at microwave frequency in communications can be optimised. As a matter of fact, the explosion in wireless communication in the last decade has been an important driving force for the extensive study and development of BST thin films and devices.

The research and development of BST thin films and devices in the literature generally included two categories: 1) The synthesis of high quality BST films and the study of structure-property relationships. 2) The design, fabrication and characterization of BST-based devices. While the study and application of BST

ceramics over the past decade may serve as a good reference, the application of BST thin films still have to face many problems, e.g. the substrate effect etc. These effects are very important for thin films but contribute little influence in bulk materials. Therefore in the literature over the last decade, there have been more efforts to reveal and interpret those phenomena and effects in BST thin films. Another important concern in the literature is the processing development and optimization. Many thin film deposition techniques have been adopted in the fabrication of BST thin films and the properties of BST are reported to be strongly dependent on the processing techniques. As matter of fact, there still exists a diversity and poor consistency amongst different literatures. Apart from the above, only a small fraction of the literature has focussed on BST devices.

This Chapter briefly described the fundamental of ferroelectricity. A short review of the literature on the studies of BST was given to understand the structure-property relationship. Finally a brief introduction to microwave technology was included.

## 2.2 Ferroelectricity

Crystals can be classified into 32 point groups [15]. These point groups can be divided into two classes: with and without a centre of symmetry. There are 21 point

groups that do not have a centre of symmetry and 20 of these point groups are piezoelectrics. Figure 2.2.1 shows the categories of various dielectrics. As a matter of fact, not every dielectric is ferroelectric. From the Figure, it is seen that all pyroelectric and ferroelectric materials are piezoelectric but the converse is not necessary true.

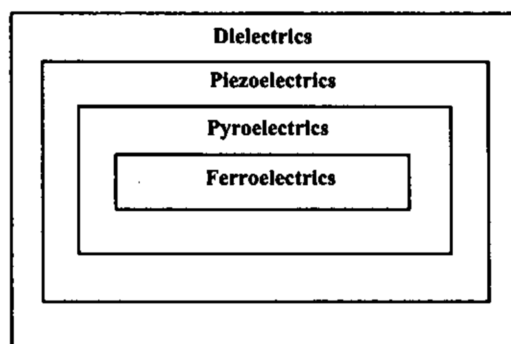


Figure 2.2.1 Categories of dielectrics.

Dielectric materials are electrically insulating (nonmetallic). In a piezoelectric material, charges are generated when appropriate stresses are applied, or vice versa. Pyroelectricity describes the temperature dependence of the spontaneous polarization. In a ferroelectric material, the spontaneous polarization can be reversed by an external electric field and also exhibits a hysteresis behaviour which is known as the polarization-electric field (PE) loop [16].

Ferroelectricity was discovered in 1921 by Valasek in Rochelle salt and it has

attracted much research interest. Piezoelectric and pyroelectric materials are called "smart materials" because the input of heat or stress can produce an electric field (voltage). Figure 2.2.2 shows schematic diagrams of $BaTiO_3$ [16]. At high temperature above its Curie temperature $T_c$, the Ti ion has higher energy to keep at the centre of the surrounding oxygen ions. The structure is cubic with no spontaneous polarization (paraelectric state). When the temperature decreases ($<T_c$) the energy of Ti ion decreases and it cannot keep in the central position of the unit cell. As the Ti ion displaces from the original central position, spontaneous polarization occurs. In addition, when an external electric field is applied and is lager than the coercive field, there is a switching of the orientation of the spontaneous polarization (ferroelectric state). The crystal undergoes a phase transition with the change of temperature. Also, it exhibits the piezoelectric effect in the ferroelectric phase, while in the paraelectric phase, it is non-piezoelectric and exhibits only electrostrictive effect.

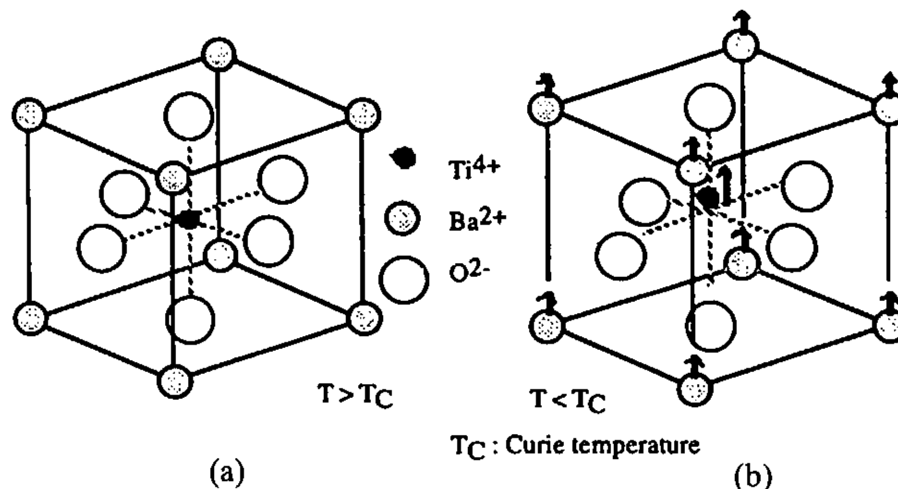


Figure 2.2.2 Structure of $BaTiO_3$ (a) above $T_c$ and (b) below $T_c$ [16].

## 2.3 Structure and property of BST

### *2.3.1 Bulk BST*

Barium strontium titanate is a continuous solid solution of barium titanate ($BaTiO_3$ or BTO) and strontium titanate ($SrTiO_3$ or STO) over the entire range of concentration. As schematically shown in Figure 2.3.1, BST has a perovskite ($ABO_3$) structure and can be regarded as the substitution of Sr atoms in the Ba-sites of the barium titanate lattice. Both BTO and STO are typical ferroelectric materials, but at room temperature STO is in the paraelectric state. The ferroelectric-to-paraelectric phase transition occurs at about 125°C for BTO and -233°C for STO. Correspondingly, the Curie temperature for BST has approximately a linear relationship with the content of BTO and STO in the solid solution (i.e., the Ba:Sr ratio). The structure-property relationship of bulk BST has been well established in the literature [17-19]. Figure 2.3.2 shows the room temperature lattice parameters and the Curie temperature of BST with different ratio of Ba to Sr.

Variations of the structure and properties of BST with Ba:Sr ratio provides a way to modify the BST properties through changing the composition to meet different application requirements. For example, BST for pyroelectric applications [20-21] is often chosen around Ba : Sr = 65 : 35 to make BST works around its Curie temperature and thus presents the largest pyroelectric coefficient. BST for high

frequency applications is often chosen around the composition of Ba : Sr = 50 : 50 [3-5]. At room temperature, BST(50/50) is in a paraelectric state and has a relatively high relative permittivity and high dielectric tunability. BST for devices used in aerospace applications is often chosen to have a composition which is very close to pure STO to obtain a high relative permittivity and tunability at that particular temperature for a specific application.

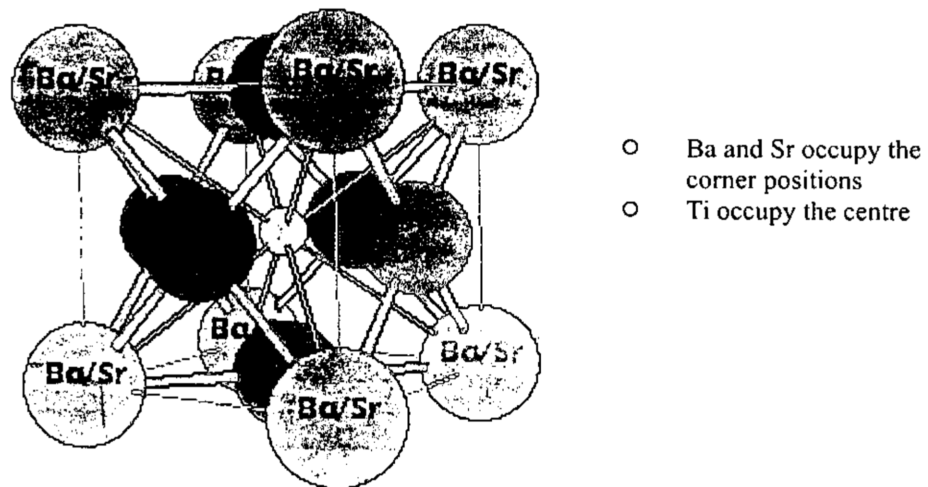


Figure 2.3.1 Schematic lattice structure of $(Ba, Sr)TiO_3$.

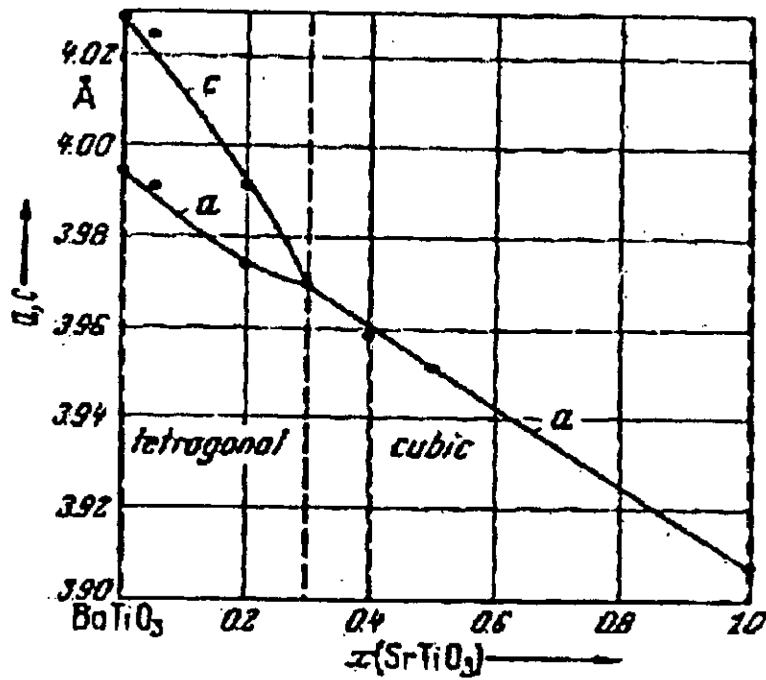


(a)

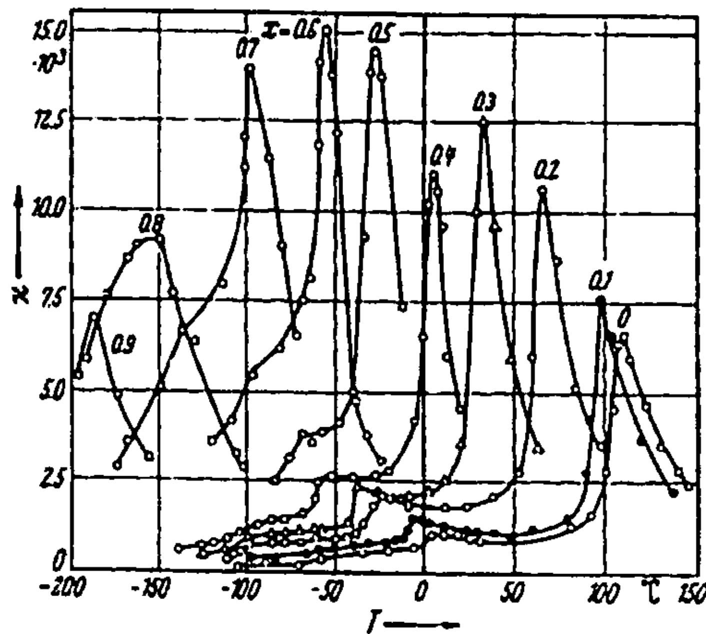


(b)

Figure 2.3.2 (a) Lattice symmetry and (b) Curie temperature of BST as a function of Ba:Sr ratio [17].

### *2.3.2 BST thin films*

BST thin films are practically more attractive for use in microwave devices than bulk materials mainly due to the lower operation voltages, smaller sizes and higher level of integration, etc. The followings are several issues on the fabrication and structure-property relationship of BST thin films reported in the literature.

#### *2.3.2.1 Thin film fabrication*

A number of deposition techniques have been employed in the fabrication of BST thin films as given in the literature [22], including the sol-gel methods, radio frequency magnetron sputtering, pulsed laser ablation deposition (PLD), chemical vapour deposition (CVD) etc. In the literature, the PLD method is the most popular method presumably due to its high deposition rate and good control of material composition. However, films prepared by PLD often exhibit a poor uniformity, making it unsuitable for device fabrication. Comparatively, magnetron sputtering and CVD method are much better choices for making large area, highly uniform films for devices although the composition control is much more difficult.

#### *2.3.2.2 Compositional dependence*

Similar to bulk BST materials, BST thin films exhibit a variation of structure and property on the Ba:Sr ratio [18]. Figure 2.3.3 shows the lattice parameters and the phase transition temperatures in BST thin films and ceramics as a function of Ba:Sr ratio. Both the films and bulk BST show a very similar trend despite the absolute

values may be different from each other. One important technical issue is that the precise control of the composition in BST thin films is not always possible and the compositional analysis is very difficult, therefore it must be very careful in analyzing the compositional dependence of BST thin films.

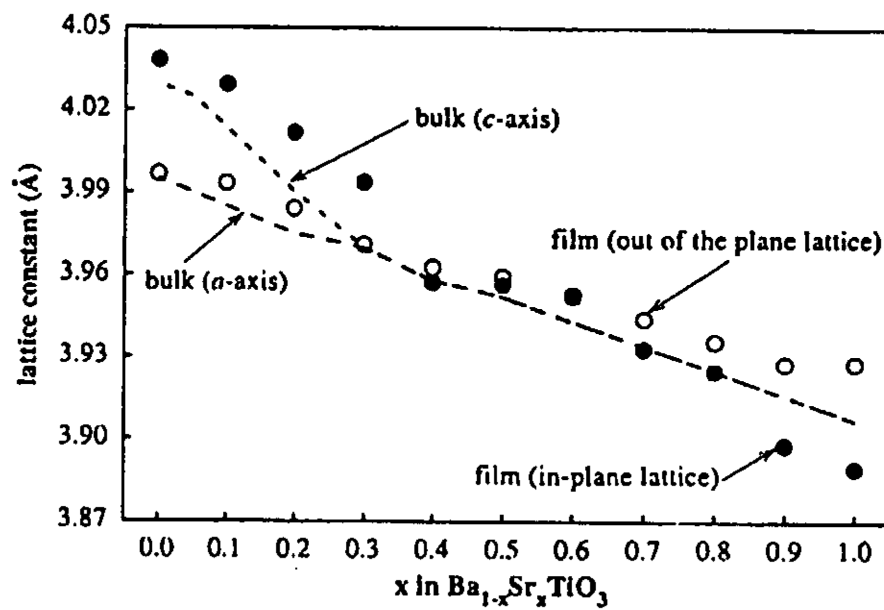


(a)

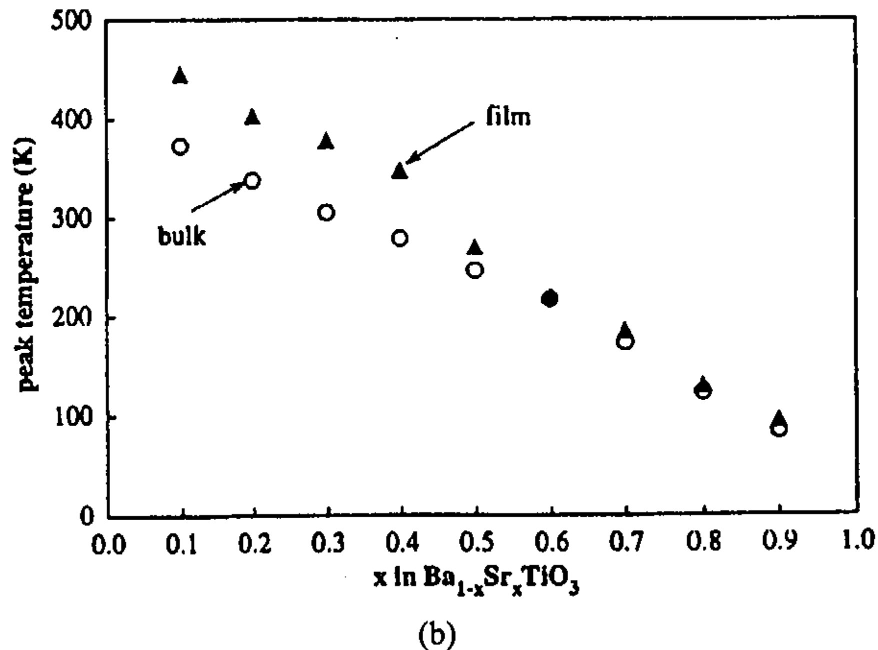


(b)

Figure 2.3.3 (a) Lattice parameters and (b) Curie temperature against x in $Ba_xSr_{1-x}TiO_3$ for film (triangle in (b)) and bulk ceramics (circle in (b)) [18].

*2.3.2.3 Extrinsic influences on BST structure and properties*

While the Ba:Sr ratio may be regarded as an intrinsic factor that determines the dielectric properties of BST thin films, some other factors such as the substrate etc., are also found to have significant influences on their structure and properties. Table 2.1 shows the dielectric properties of BST thin films on different substrates [23]. The measured capacitance of BST thin films on lanthanum aluminum oxide (LAO) single crystal is larger than that on magnesium oxide (MgO) single crystal because of different lattice mismatch. These extrinsic factors are the major reasons why BST thin films perform differently from bulk materials.

Table 2.1 Dielectric properties of BST thin film on LAO and MgO substrates [23].

| | Electric field [kV/cm] | BST on MgO | | BST on LAO | |
|---|---|---|---|---|---|
| | | as-deposited | annealed | as-deposited | annealed |
| Capacitance [pF] | 0 | 0.775±0.193 | 0.387±0.035 | 0.440±0.028 | 1.281±0.161 |
| | 67 | 0.418±0.121 | 0.253±0.031 | 0.354±0.039 | 0.594±0.098 |

## 2.4 Introduction to microwave technology

Nowadays microwave techniques have been increasingly adopted in diverse applications such as radio astronomy, long-distance communications, space navigation, radar systems, medical equipment and missile electronic systems. There is an accelerated rate of growth of microwave technology in research and industry, including techniques in the characterization and applications of materials at microwave frequencies.

In general, the microwave region begins above the UHF region, at 900 or 1000 megahertz (MHz) and below the infrared (IR) range [24] as shown in Figure 2.4.1.

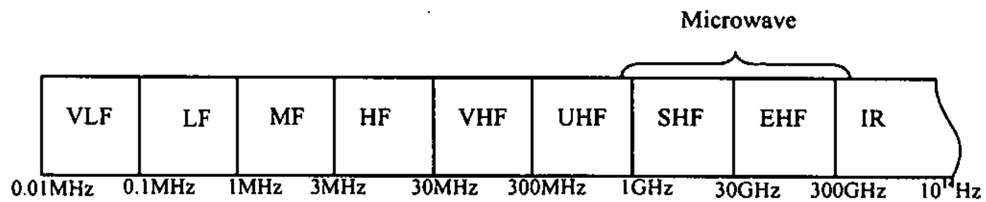


Figure 2.4.1 The electromagnetic spectrum.

There are interest in the fabrication and chararcterization of thin film-based devices using materials such as STO and BST because of their tunable dielectric property. For example, in a tunable ring resonator as shown in Figure 2.4.2 [25], the structure is Au/STO/LAO. The ring was designed to satisfy the condition $2\pi R = 3\lambda$, where R is the mean radius of the ring and λ is the wavelength. Figure 2.4.3 shows the results of the tunable device in which the resonant frequency shifted under a dc bias for microwave application. The presence of the thin film can decide the position of the resonant frequency which depends on its relative permittivity and its thickness. This shows one example of a thin-film microwave device.

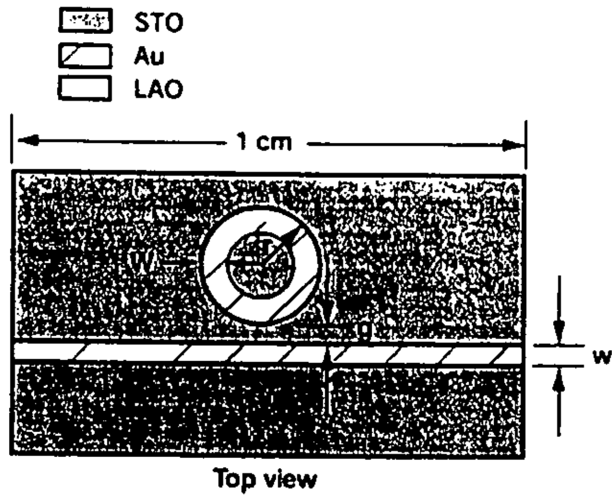


Figure 2.4.2 Top view of the thin film-based device.

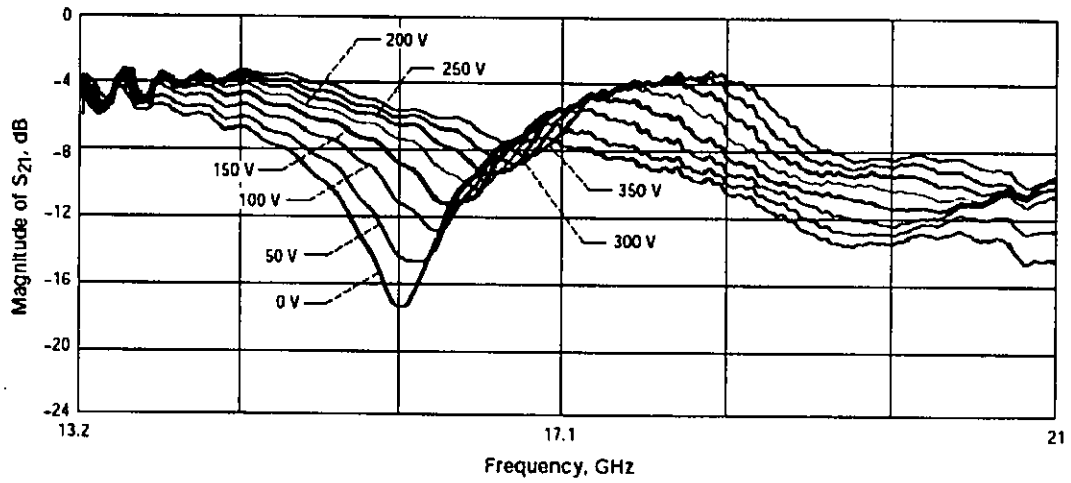


Figure 2.4.3 Results of the thin film-based resonator under a dc bias [25].

# Chapter 3

# Fabrication and characterization of BST thin films and electrode patterning

## 3.1 Introduction

The techniques for fabricating thin film can generally be divided into three categories: chemical solution deposition (CSD), physical vapour-deposition (PVD) and chemical vapour-deposition (CVD). Because these techniques have different advantages and disadvantages, the technique of choice will be dictated by property requirement. For example, CSD techniques offer a relatively simple and low cost approach to the fabrication of thin film that is compatible with commercial processing equipment and techniques such as spin coating and photolithography. For higher performance applications such as tunable microwave devices, PVD and CVD are better suited to heteroepitaxial film growth.

In this thesis, CSD and PVD methods are used. The sol gel method is a CSD method in which the fabrication cost is relatively low. It is easy to implement and the most important advantage is the excellent compositional control, which is critical for stoichiometric systems. On the other hand, radio frequency magnetron sputtering is the PVD method used. This method permits the fabrication of large area films with

good uniformity. These two techniques are commonly used in the deposition of high quality thin films. The electrode patterning by the standard photolithography is also introduced in this Chapter.

## 3.2 Thin film deposition

### *3.2.1 Radio frequency magnetron sputtering*

#### *3.2.1.1 Setup*

The basic principle of magnetron sputtering is that when an electrical power is applied, the energetic ion beam supplies kinetic energy to the target atoms. They leave the target and are deposited on the substrate. A magnet is used to provide a crossed magnetic field which induces the ions to move in a cycloidal path. It can increase the gas injection probability and reduce the bombardment to the substrate, thereby increasing the yield. The requirements in the sputtering ions are that they must be chemically inert and argon is a common choice. For insulating films, in our case, BST, rf sputtering must be used.

Figure 3.2.1(a) is the schematic setup of the magnetron sputtering system. The target and the substrate are mounted in a vacuum chamber. A mechanical pump is used to evacuate the chamber first followed by the use of a turbo-molecular pump to achieve a higher vacuum. The mechanical pump and the turbo-molecular pump are then operated simultaneously. Figure 3.2.1(b) shows a photograph of the magnetron sputtering system used in this work.

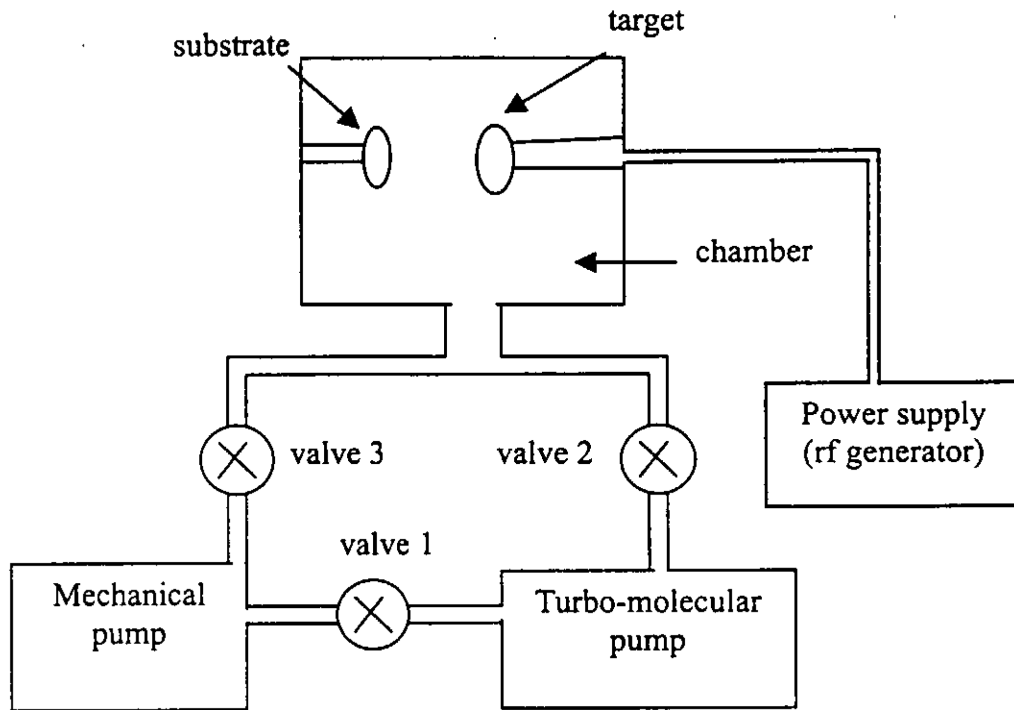


(a)

(b)

Figure 3.2.1 (a) Schematic setup and (b) Photograph of the magnetron sputtering system.

The substrates used in sputtering are LAO and MgO single crystals. Their lattice parameters, as shown in Table 3.1, are similar to that of BST. The lattice mismatch is small which is necessary for orientation control and for the growth of high quality films. Silicon wafers with platinum (Pt) electrodes, LAO and zirconia ($ZrO_2$) single crystals were also used as substrates in the sol-gel preparation of BST.

Table 3.1 Lattice parameters and thermal expansion coefficients of BST and the substrates.

| | Bulk BST (50/50) | LAO | MgO |
|---|---|---|---|
| Lattice constant ($10^{-10}$m) | 3.947 | 3.787 | 4.213 |
| Lattice mismatch | - | ~4.1% | ~-6.7% |
| Thermal expansion coefficients ($10^{-6}$/°C) | 10.5 | 10.0 | 13.8 |

Table 3.2 Conditions of the BST deposition.

| Target | Stoichiometric $(Ba_{0.5}Sr_{0.5})TiO_3$ ceramic |
|---|---|
| Sputtering power | 90W |
| Substrate temperature | 450°C |
| Gas pressure for deposition | 5 Pa |
| Gas flow rate ($Ar:O_2$) | 9:1 |

BST films were sputtered from a stoichiometric $(Ba_{0.5},Sr_{0.5})TiO_3$ target ( Kurt L. Lester) onto the LAO or MgO substrates with conditions as shown in Table 3.2. The parameters listed above is very important, for example, the gas flow rate of the

mixture of argon and oxygen will affect the deposition rate and vary the final composition of the BST thin films. A high gas pressure is beneficial for better composition control but causes a low deposition rate. The importance of controlling these parameters have been discussed in the literature [26, 27].

After BST film deposition, the samples were then put into a tube furnace for annealing at 1000°C for 3 hours.

*3.2.1.2 Structural characterization*

The phase and microstructure of the BST films were investigated by X-ray diffraction (XRD) and atomic force microscopy (AFM), respectively.

X-ray diffraction (XRD) is used to characterize the crystallization of the BST thin films. In an XRD measurement, the X-ray was incident on the thin film surface and the detector was scanned to receive the signal as shown in Figure 3.2.2. The path difference x is equal to d sin θ. For constructive interference, the total path difference should be equal to the multiple of the wavelength,

$$n\lambda = 2d\sin\theta \qquad (3.2.1)$$

which is the Bragg's law and λ=0.154nm is the wavelength of the X-ray (Cu Kα radiation) and d is the lattice spacing. A diffraction peak is formed when the Bragg

condition is satisfied. An XRD spectrometer (X'pert System, Philips Electronic Instruments) was used to measure the x-ray spectra of the BST samples.

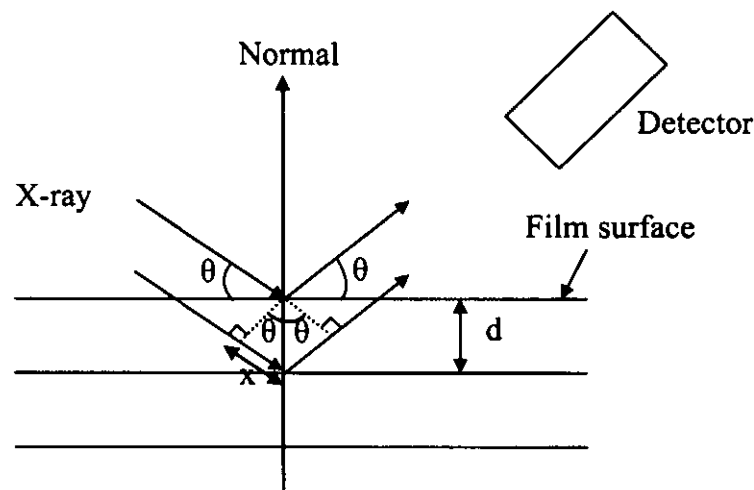


Figure 3.2.2 Schematic diagram of the basic principle of XRD.

AFM is used to determine the roughness of the BST thin film. Figure 3.2.3 shows the principle of the AFM. As the scanner gently traces the tip across the sample, the contact force causes the cantilever to bend to accommodate the changes in topography. A laser beam then bounces off the back of the cantilever onto a position-sensitive photodetector (PSPD). The laser beam on the detector will shift if the cantilever bends. The PSPD itself can measure displacements of light as small as 10 angstrom. The ratio of the path length between the cantilever and the detector to

the length of the cantilever itself produces a mechanical amplification. As a result, the system can detect sub-angstrom vertical movement of the cantilever tip. The AFM Met. 2000NC, Burleigh was used in the present study.

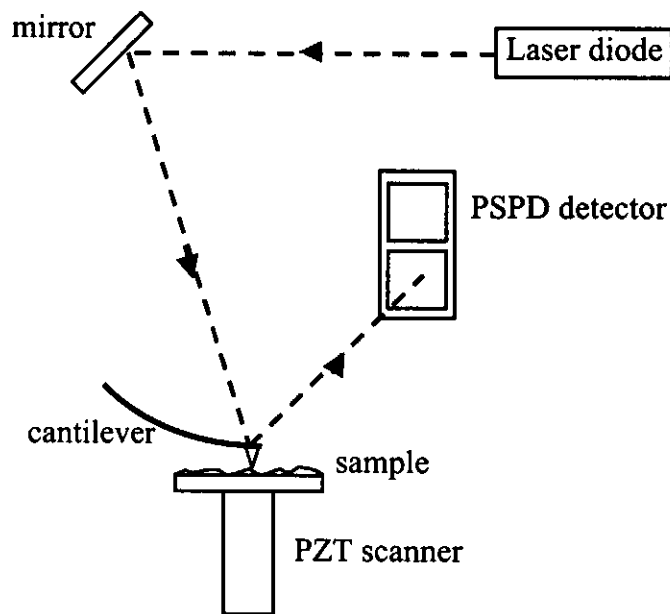


Figure 3.2.3 Schematic diagram of the basic principle of AFM.

Figure 3.2.4 shows the XRD spectrum and the AFM micrograph of the as-deposited BST film. It is seen that the film was still amorphous and the particle size is quite small. After it was annealed at 1000°C for 3 hours, typical perovskite peaks were observed in the XRD pattern and the grain size and roughness increased with post-annealing as shown in Figure 3.2.5.

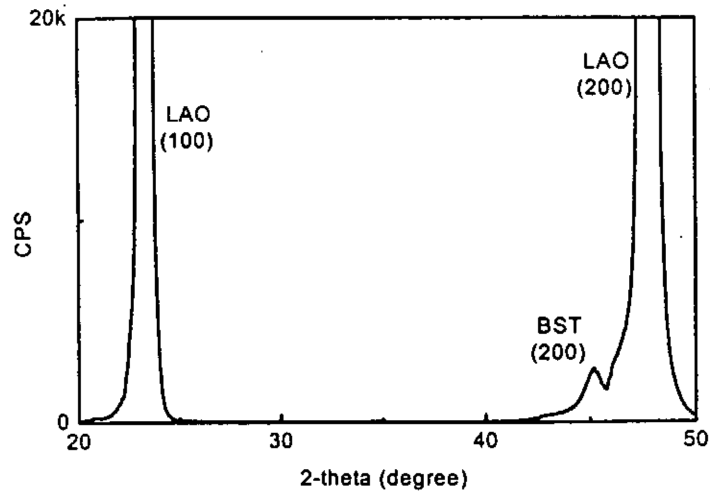


(a)

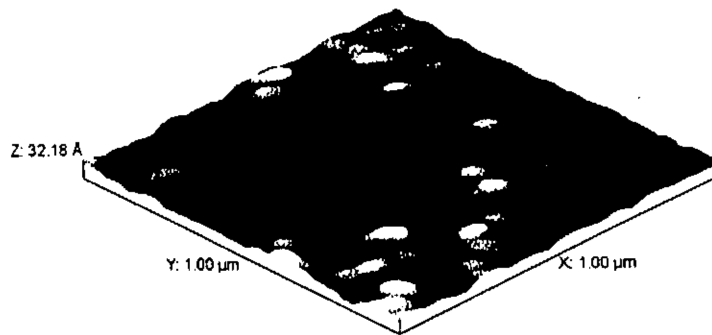


(b)

Figure 3.2.4 (a) XRD and (b) AFM micrograph of the as-deposited BST film.

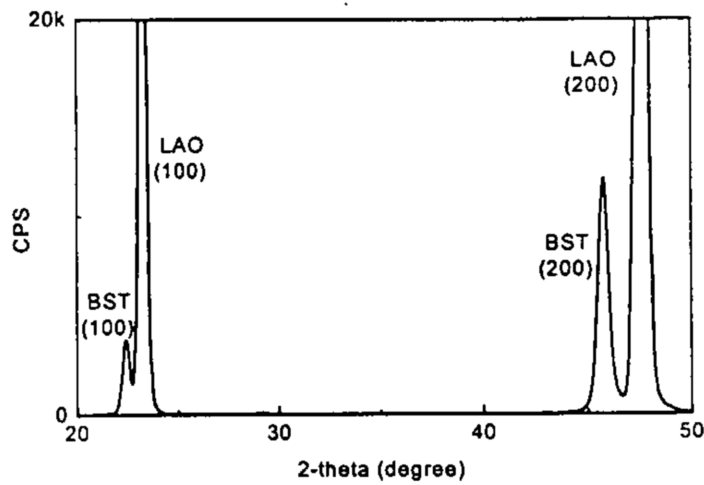


(a)

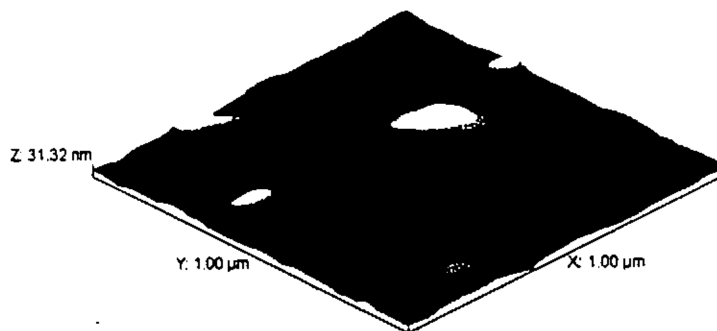


(b)

Figure 3.2.5 (a) XRD and (b) AFM micrograph of the annealed BST film.

Some parameters are critical to the BST sputtering as mentioned before. Figure 3.2.6 shows the XRD of BST film deposited without substrate heating. The film is deposited following the conditions listed in Table 3.2, except that the substrate temperature is at room temperature and followed by 1000°C annealing. The film has

relatively poor crystallization. It is because the ions coming out of the target have relatively high energy, when they land onto a heated substrate and have enough energy to re-orientate, they can form some stacking close to the structure of the crystal. Such films are easier to crystallize upon annealing. But if there is no substrate heating, the ions will have to stay where they are, therefore the whole film would be amorphous. Such amorphous film is hard to crystallize during annealing and higher temperature may be required.

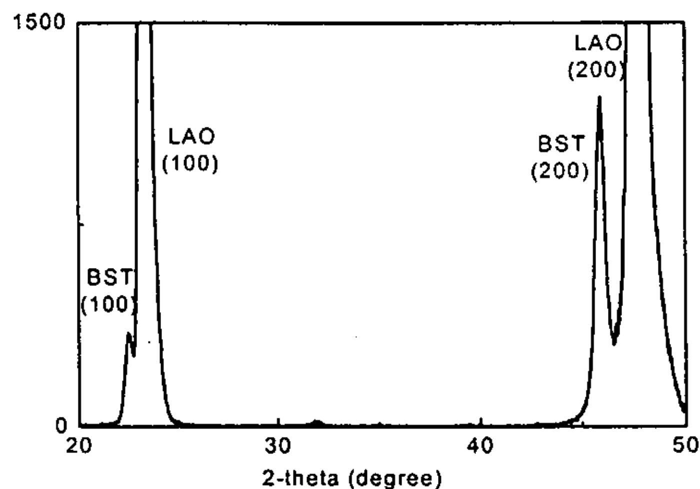


Figure 3.2.6 XRD of the BST film without substrate heating during deposition.

Figure 3.2.7 shows the AFM morphology of BST with 1100°C annealing for 3 hours. The deposition conditions are the same as shown in Table 3.2. The problem of annealing at relatively high temperature is the overgrown of the grain size and the film has poor uniformity. The film surface is not smooth and is less transparent.

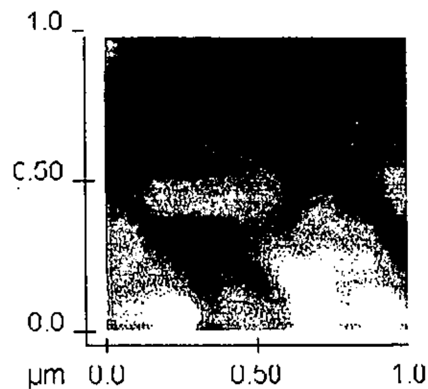


Figure 3.2.7 AFM morphology of the BST film with 1100°C annealing.

### *3.2.2 Sol gel deposition*

#### *3.2.2.1 Process flow*

The basic steps in sol gel fabrication are to prepare appropriate solution containing elements of the desired compound, then polymerize the solution to form a gel, followed by dry and fire this gel to remove the organic components to form a final inorganic oxide. In general, these films are heat-treated using a two-step process: the low-temperature step is used to pyrolyze the organics and the higher temperature step is used to crystallize the film.

The starting BST sol-gel solution ($Ba_{0.7}Sr_{0.3}Ti_{0.95}O_3$ and $Ba_{0.5}Sr_{0.5}TiO_3$) were commercial solutions (Mitsubishi Materials Co., Japan). First the substrates (Pt/Si, $ZrO_2$ and LAO single crystals) were cleaned in an ultrasonic bath using 2-propanol and acetone as cleaning agents. The substrates were fixed on the spin coater by a

vacuum. The BST solution was injected onto the substrate surface and spun at 3000 rpm for 30 seconds. The coated film was then put on a hot plate (at ~250°C) for 5 minutes to remove the organic solvent (pyrolyzing). The pyrolyzed films have amorphous structures, and post-deposition annealing was necessary to crystallize the films. The crystallization was performed using a rapid thermal processor (RTP):

1) For $Ba_{0.7}Sr_{0.3}Ti_{0.95}O_3$ on Pt/Si and $ZrO_2$ substrates:

Held at 350 °C for 5 minutes and then heated up to 550°C-750°C to anneal for 30 minutes in the flow of oxygen.

2) For $Ba_{0.5}Sr_{0.5}TiO_3$ on LAO substrates:

Held at 350 °C for 5 minutes and then heated up to 750°C to anneal for 30 minutes in the flow of oxygen. When the desired thickness of the film was obtained, it was annealed in a tube furnace at 1000°C for 3 hours.

To obtain the desired thickness of the films, the coating, pyrolyzing and annealing steps were repeated. Figure 3.2.8 shows the flow chart of the sol gel method described above.

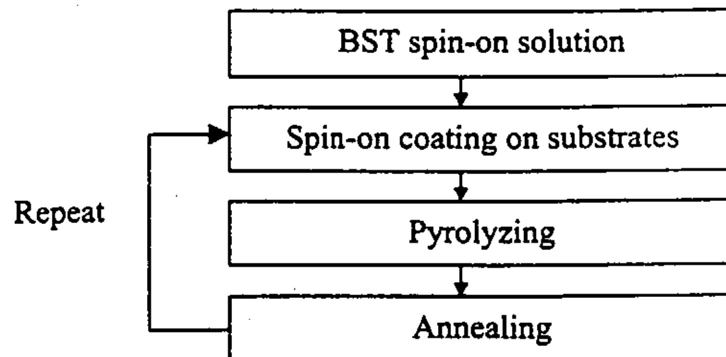


Figure 3.2.8 Flow chart of the sol gel method.

*3.2.2.2 Structural characterization*

Figure 3.2.9(b) shows the XRD patterns of BST annealed at 650°C, there is an improvement in the crystallization of the film when comparing with the film annealed at 550°C (Figure 3.2.9(a)). The perovskite peaks (arrows) became very sharp after the film was annealed at 650°C.

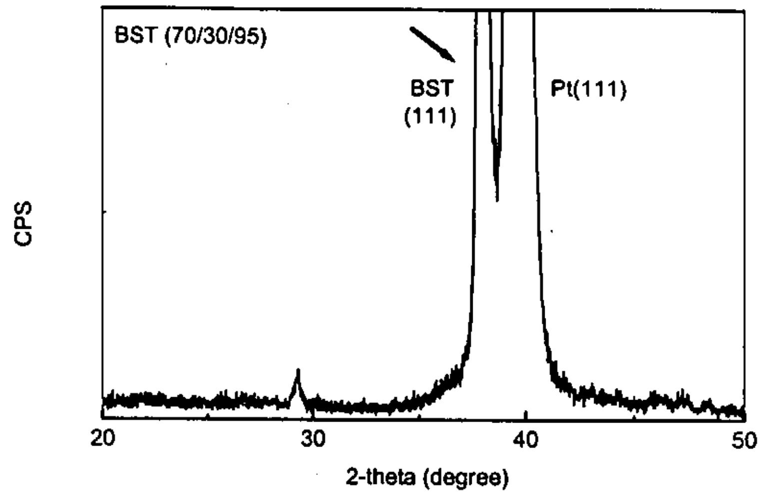


(a)

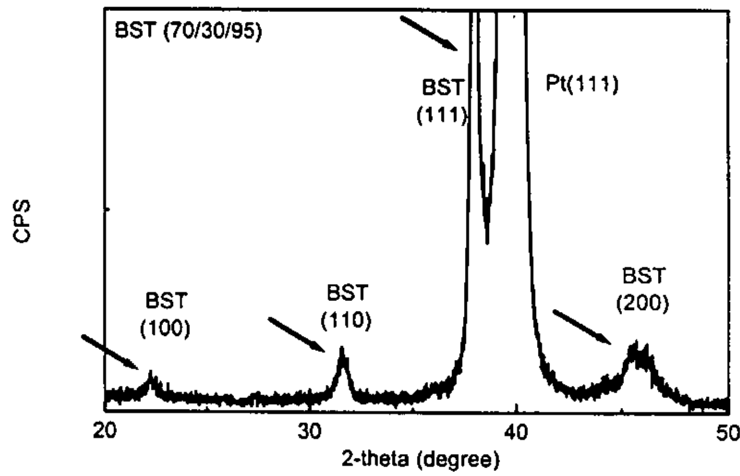


(b)

Figure 3.2.9 XRD of BST film on Pt/Si annealed at (a) 550°C and (b) 650°C.

## 3.3 Electrode patterning

### *3.3.1 Electrode deposition*

After thin film deposition, gold electrode was formed on the top of the thin film by magnetron sputtering. Table 3.3 shows the conditions of the sputtering. The substrate temperature was 200°C to enhance the adhesion between the gold electrode and the film. The thickness of the gold electrode was about 250 nm to 400 nm. The sample structure is shown in Figure 3.3.1.

Table 3.3 Conditions of the gold deposition.

| Target: | Gold |
|---|---|
| Sputtering power: | 70W |
| Substrate temperature: | 200°C |
| Gas pressure for deposition: | 1 Pa |
| Gas flow rate of Ar: | 10 sccm |

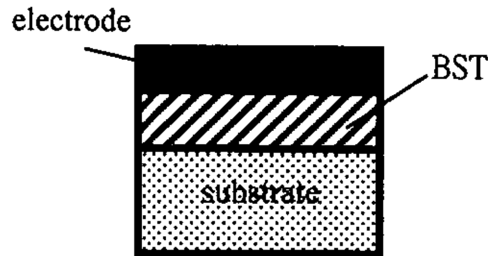


Figure 3.3.1 Structure of the sample after electrode deposition.

### *3.3.2 Photolithography*

Photolithography is the basic technique used to define the shape of micromachined structure. The technique is essentially the same as that used in the microelectronics industry.

#### *3.3.2.1 Basic tool for the photolithography*

Firstly a mask was produced. The electrode pattern was designed and drawn by an AutoCad software. Then the file was converted to a L-Edit type file by a LinkCad software because the manufacturer (Microelectronic Fabrication Facility of HKUST) only support this type of file for mask fabrication. The smallest size for the mask pattern fabrication was 1 μm. Actually, the mask was a chromium pattern on a glass plate as shown in Figure 3.3.2.

Photoresist is a polymer which is sensitive to ultraviolet light. There are two types of photoresists, termed positive and negative. When the ultraviolet light strikes a positive photoresist it weakens the polymer, so that when the image is developed the photoresist at locations where it has been exposed to light will be washed away. When ultraviolet light strikes a negative photoresist it strengthens the polymer. So when developed the photoresist that has not been exposed to the ultraviolet light will be washed away, a negative image of the mask is then transferred to the photoresist.

An optical aligner was used to align the mask and the sample and it also provided the ultraviolet light for exposure. As mentioned before, the photoresists were removed after development. The developer used in the development was used to remove the unwanted photoresist.

A suitable chemical solution was then used to remove the material which was not protected by the photoresist. The chemical used is dependent on the materials. The process of wet chemical etching is the removal of material by immersing the wafer in a liquid bath of the chemical etchants. There are two types of wet etchants: isotropic etchants and anisotropic etchants. Isotropic etchants attack the materials being etched at the same rate in all directions. Anisotropic etchants attack the silicon wafer at different directions with different rates, and so there is more control on the shapes produced. In our case, isotropic etchants were used in this study.

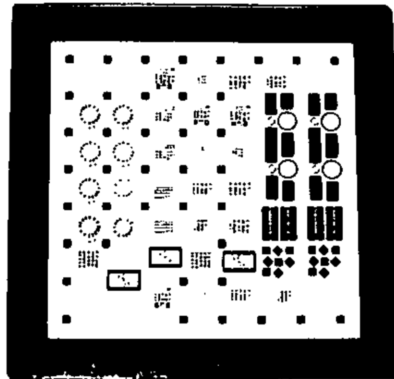

Figure 3.3.2 Photograph of the mask used in the photolithography.

### *3.3.2.2 Process of the photolithography*

Figure 3.3.3 shows the conditions and the process flow of photolithography.

Spin photoresist
□ spin speed : 4500 rpm for 60 seconds

Baking
□ 10 minutes at 80°C

UV exposure
□ exposure time 16~18 seconds

Development
□ rinse in developer for about 1-2 minutes

Wet etching
□ rinse in chemicals for about 1-2 minutes

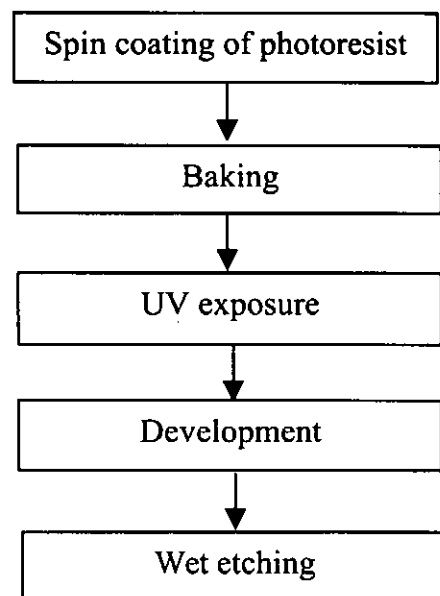


Figure 3.3.3 Process flow of the photolithographic technique.

The positive photoresist (AZ3100, Clariant (China) Ltd) was first spun onto the top of the electrode by a spin coater, then it was placed into the furnace for baking to remove the solvent. After that, an aligner (model no.: JKG-2A, Shanghi Optical Machinery Works) was used to align the sample and the mask for UV exposure. This step must be performed in a room with sodium yellow lighting. Because a positive photoresist was used, the exposed part can be removed by the developer (AZ300, Clariant (China) Ltd). After being developed for about one to two minutes and followed by wet etching, the pattern of electrode was formed. The solution for etching the gold is a combination of the chemicals of KI, $I_2$ and $H_2O$.

There are some important parameters in these steps, e.g. UV exposure time and development time. Especially the length of time for the gold etching, it will be over-etched if the time is too long, leading to the partial detachment of the electrode pattern. All the parameters must be well-controlled. Figure 3.4.4 shows the schematic diagram of the sample.

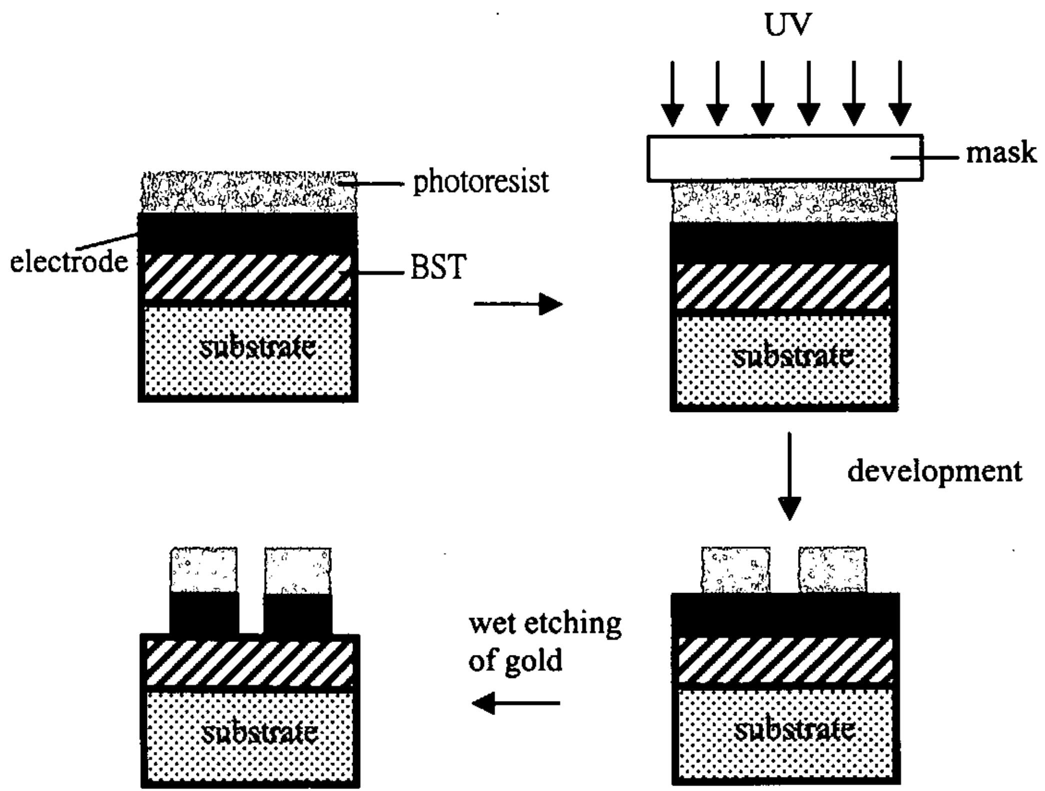


Figure 3.3.4 Schematic diagram of the sample at each step.

Finally, the photoresist on the top has transformed into a very long-chain polymer after the process of development and heat treatment and it cannot be removed by the acetone. Using an oxygen plasma is the preferred way. Plasmas for etching are formed by applying a radio-frequency electric field to a gas held at low pressure in a vacuum chamber. Because the energy of the electron in the plasma is much higher than the chemical bond energy, molecules in a plasma are essentially randomized, breaking down by recombination with electron. Figure 3.3.5 shows the final structure of the sample with an interdigital electrode pattern.

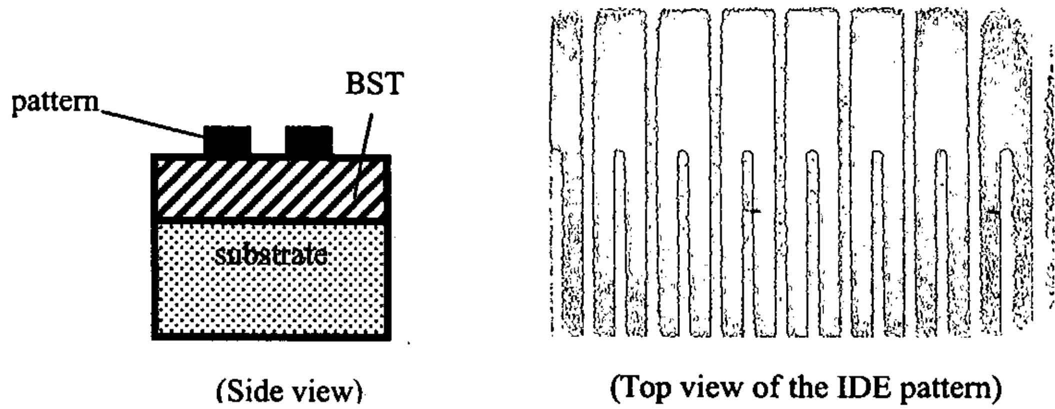


Figure 3.3.5 Side and top views of the sample.

## 3.4 Summary

In this Chapter, BST thin film depositions by the rf magnetron sputtering and sol gel methods were introduced followed by the structural characterization of the thin films by XRD and AFM. The process of standard photolithography to pattern the electrode (e.g. IDE) was also discussed.

# Chapter 4

# Dielectric characterization of BST thin films in coplanar capacitors

## 4.1 Introduction

Compared with conventional ferroelectric film-based parallel plate capacitors, the coplanar capacitors with a structure of electrode/film/substrate are different in many aspects. In a coplanar capacitor, for example, the film is grown directly on the substrate, therefore the film quality and the orientation could be better controlled than that in a parallel plate capacitor. Moreover, when an external electric field is applied to the sample, the field distribution in the film of a coplanar capacitor is quite different from that in a parallel plate capacitor. These differences lead to the needs of systematic investigations on the processing-structure-property relationship in the ferroelectric film-based coplanar capacitor so as to improve the overall performance. Technically, at microwave frequency measurements, the dielectric characterization of ferroelectric thin films in a coplanar capacitor is difficult and complicated because of:

1) The parasitic capacitance of the electrodes [28] are not negligible at high frequencies. Therefore the "real" capacitance of BST cannot be directly obtained from the instrument readings.
2) Microwave devices are often made to have a coplanar capacitor structure,

i.e., both electrodes are on top of the thin film. Therefore the relationship of the capacitance (C) and the relative permittivity (ε) of BST cannot be described by the traditional C~ε equation for parallel plate capacitors.

To solve these technical problems and obtain accurate dielectric data for the BST film, various theoretical and technical efforts have been reported in the literature on this issue. With reference to the literature and also based on our experience, we demonstrate our approach on the extraction of the relative permittivity over a wide frequency range from BST film-based interdigital electroded capacitors (IDCs). The characterization procedure basically includes three steps:

Step 1: Dielectric measurement of the IDC by a two-step calibration.

Step 2: Extraction of the pure capacitive part of the IDC by using an equivalent circuit (removal of parasitics based on the data of step 1).

Step 3: Calculation of the relative permittivity of BST from the capacitance.

In this Chapter, the procedure of dielectric characterization of ferroelectric thin films using IDCs is described.

## 4.2 The procedure of dielectric characterization

### *4.2.1 Geometrical description of an IDC*

The structure of an interdigital electrode is schematically shown in Figure 4.2.1(a). A set of geometrical parameters such as the electrode finger "width", "gap", "length" and "number" are needed to describe the electrode.

An IDC can be divided into two parts: interdigital electrode "fingers" (the group of parallel lines) and two electrode "arms" with the "pads". The "fingers" part may be regarded as the "main" interdigital electrodes and the other parts are for the convenience of measurement. For an IDC measured at high frequency, the "arms" and "pads" contribute to a parastatic capacitance which is an interference to the characterization of the "main" IDC and the thin film. To remove the parasitic capacitance, two more patterns which are called "open" and "short" references (schematically shown in Figure 4.2.1(b) and Figure 4.2.1(c)) were fabricated on the same thin film/substrate structure. The properties of the references are to be used in the calculation of parasitics removal.

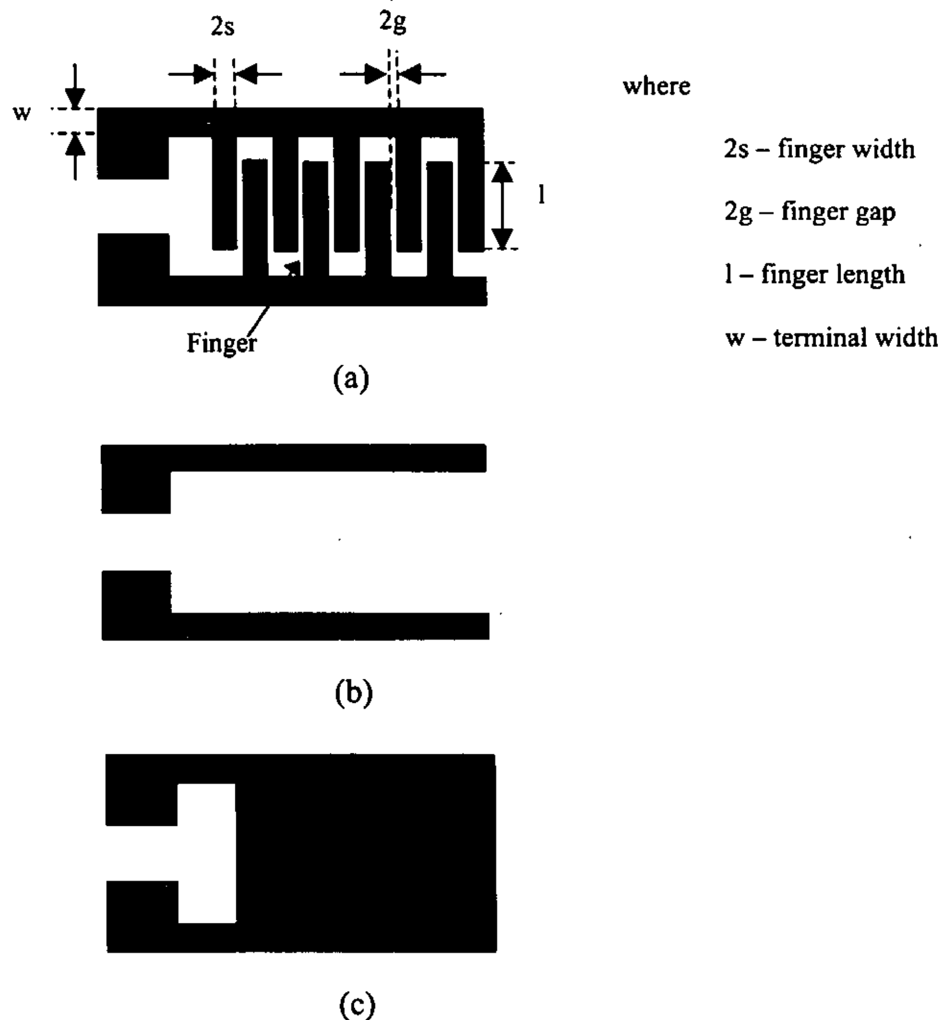


Figure 4.2.1 Schematic structure of: a) an interdigital electrode (IDE), b) the open reference and c) the short reference.

### *4.2.2 High frequency dielectric measurements*

The high frequency dielectric measurement system includes a network analyzer 8720ES (Agilent, USA) connected with a standard probe station Microtech RF-1 (Cascade, USA). The experimental setup is shown in Figure 4.2.2.

The dielectric measurement was usually carried out at room temperature. Before the measurement, the instruments were switched on and warmed up sufficiently followed by a very careful 2-step calibration.

(1) Standard calibration of the instruments: The network analyzer and probe station were first calibrated. This step aimed to remove the parasitics of the probes and connection wires. The impedance standard substrates (ISS) with "short", "open" and "load" standards provided by the probe station manufacturer were used in the calibration, which was carried out following the operation instructions. Details of the calibration are available in the operation manual of the instruments.

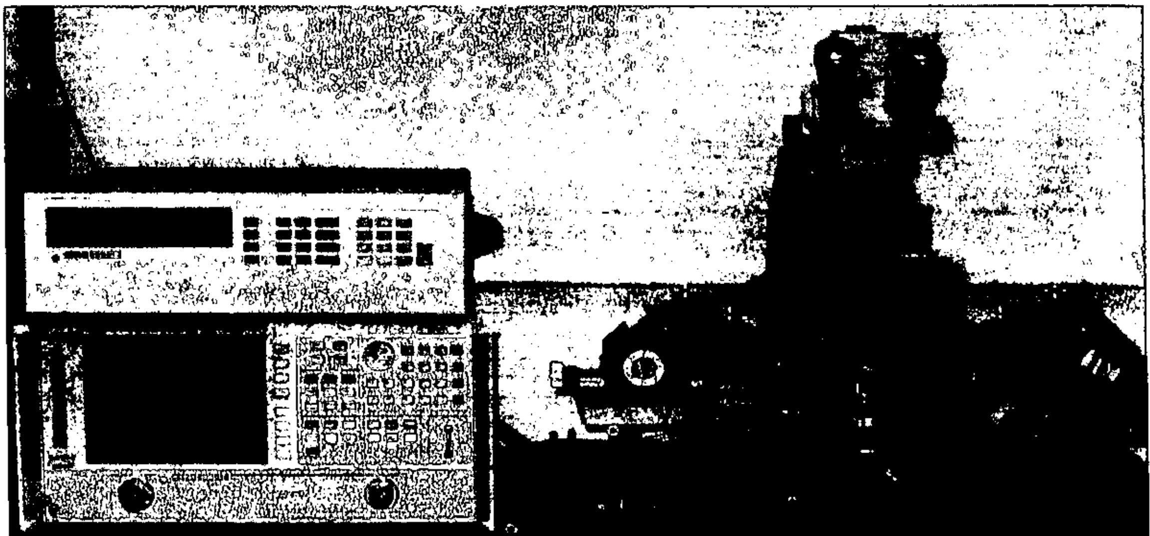

Figure 4.2.2 Measurement instruments: network analyzer and probe station.

(2) Calibration for the removal of parasitic capacitance in the IDE. This part of calibration included the measurement of the parasitic capacitance i.e. the impedance

of the open and short reference capacitors shown in Figure 4.2.1(b) and Figure 4.2.1(c).

In practical measurements, the reflection coefficient ($S_{11}$) rather than the capacitance was measured on the network analyzer. From $S_{11}$, the input impedance (Z) could be obtained using [28]:

$$Z = Z_0 \times \frac{1 + S_{11}}{1 - S_{11}} \tag{4.2.1}$$

where $Z_0$ is the characteristic impedance of the network analyzer. By the above steps, the impedance of the short, open and interdigital capacitors (named as $Z_{short}$, $Z_{open}$ and $Z_{IDE}$) were obtained.

### *4.2.3 Removal of the parasitic capacitance*

Based on the measured data ($Z_{short}$, $Z_{open}$ and $Z_{IDE}$) as described above, we model an equivalent circuit for each electrode pattern (the interdigital electrode IDE, open reference and short reference) was used to remove the parasitics. For example, the equivalent circuit for the IDE pattern ( Figure 4.2.1(a) ) is shown in Figure 4.2.3. In the circuit, $Z_{line}$ is the impedance of the pad and arm electrodes, $Z_p$ the parasitics between pads and electrodes, $Z_s$ the impedance due to the IDC "finger" and $Z_{DUT}$ is the impedance of actual device under test (DUT) which represents the group of

parallel fingers. The aims in this part are to obtain the "main " capacitance of the IDC ($Z_{DUT}$).

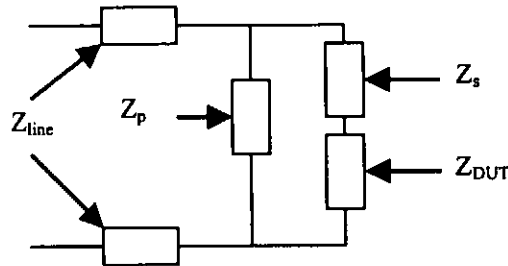


Figure 4.2.3 Equivalent circuit of the IDE with the parasitics to be de-embedded.

By analyzing the equivalent circuit, we have:

$$Z_{IDE} = 2 \times Z_{line} + \frac{1}{\frac{1}{Z_p} + \frac{1}{Z_s + Z_{DUT}}} \tag{4.2.2}$$

Also, similar work will be applied to both the open and short references,

$$Z_{short} = 2 \times Z_{line} + \frac{1}{\frac{1}{Z_p} + \frac{1}{Z_s}} \tag{4.2.3}$$

$$Z_{open} = 2 \times Z_{line} + Z_p \tag{4.2.4}$$

By solving (4.2.2), (4.2.3) and (4.2.4) and assuming $Z_{line}$=0 (valid below 10 GHz), the

impedance of the actual device under test (DUT) is:

$$Z_{DUT} = \frac{Z_{IDE} \times Z_{open}}{Z_{open} - Z_{IDE}} - \frac{Z_{short} \times Z_{open}}{Z_{open} - Z_{short}} \qquad (4.2.5)$$

$Z_{DUT}$ is then fitted to a parallel resistor-capacitor model,

$$\frac{1}{Z_{DUT}} = \frac{1}{R} + j\omega C \qquad (4.2.6)$$

where R is the resistance, ω the angular frequency and C is the capacitance. Finally, the "main" capacitance from an IDC can be obtained.

### *4.2.4 Extraction of relative permittivity of the film*

Among various models in the literature describing the relationship of the IDC capacitance and the material properties, Gevorgian's model [29-31] gives a clear physical picture and relatively simple mathematical formula and it has been chosen in our calculation. The main ideas of the model are important for the understanding of the extraction procedure:

(1) The partial capacitance techniques [29]: Since the dimensions of the IDC are much less than the wavelength in the microwave devices, there is no capacitance contribution from nonadjacent fingers. The capacitance (C) of an IDC with n fingers

may be presented as the sum of capacitance from a three-finger capacitor (one-half of both sides) $C_3$, and the capacitances of periodical (n-3) structures $C_n$ and a correction term for the fringing fields of the ends of the finger, $C_{end}$ as shown in Figure 4.2.4:

$$C = C_3 + C_n + C_{end} \tag{4.2.7}$$

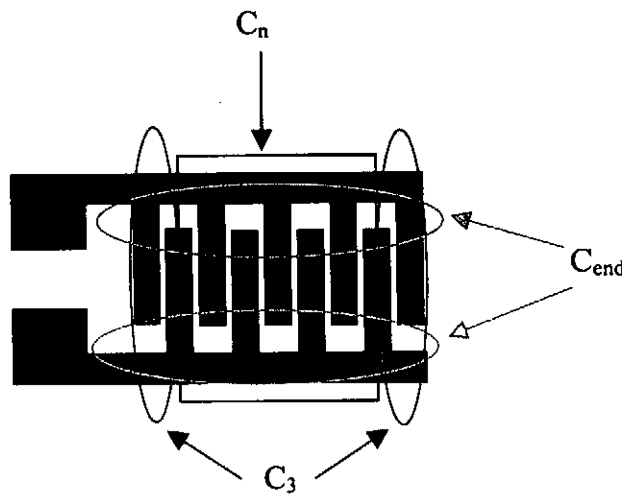


Figure 4.2.4 A planar view of an IDC for the partial capacitance technique.

On the other hand, a coplanar capacitor with multiple dielectric layers can be regarded as a sum of several single layer coplanar capacitor with the relative permittivity properly modified as shown in Figure 4.2.5.

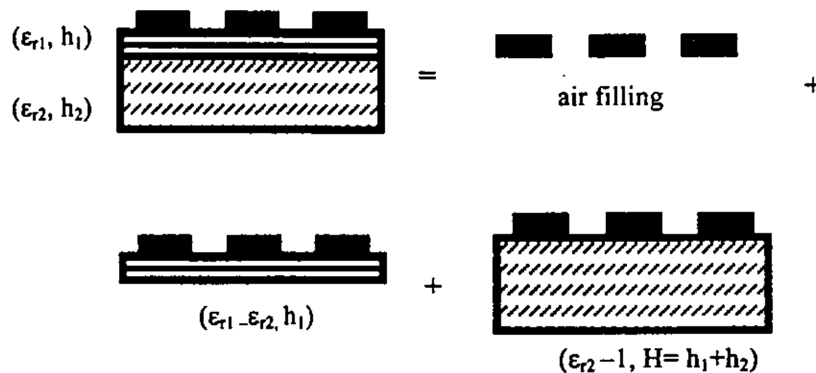


C (total) = $\Sigma$ (capacitance of each layer)

= C (capacitance with air filling)
+ C (relative layer with equivalent permittivity [$\varepsilon_{r2}$-1] and thickness H )
+ C (relative layer with equivalent permittivity [$\varepsilon_{r1}$-$\varepsilon_{r2}$] and thickness $h_1$)

Figure 4.2.5 Schematic diagram of the partial capacitance technique for a multilayer sample.

(2) Conformal mapping transformation [32]: Conformal mapping method is widely used in physics to solve the problems concerning materials and devices with complex shapes. In Gevorgian's model, this method was employed to transform the coplanar capacitor to a parallel plate capacitor. Figure 4.2.6 demonstrates the transformation of a single layer IDC (from original coplanar structure → finally a parallel plate capacitor in W-plane).

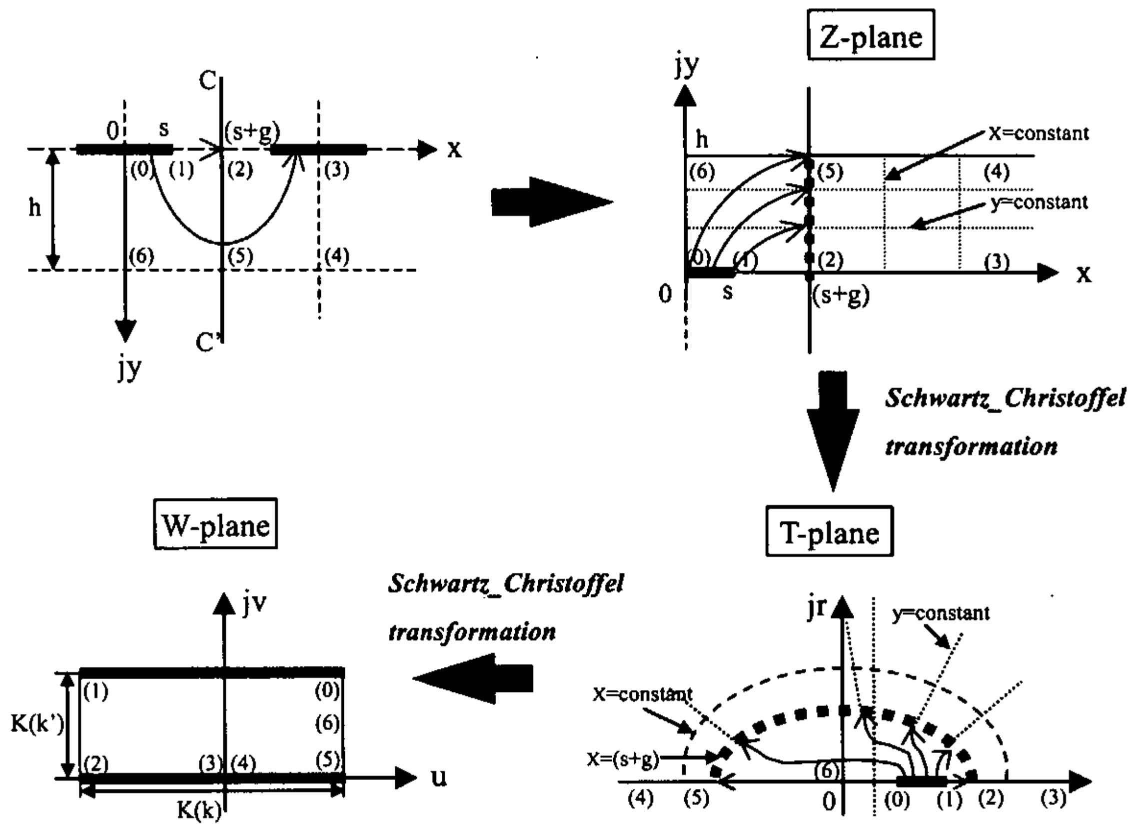


Figure 4.2.6 A periodical structure of IDC (a), and its mapped planes: (b) transfer to Z-plane, (c) Z plane to T-plane and (d) T plane to W-plane [29].

Details of the principles of the mapping techniques are available in reference [29] and will not be discussed here. The important point is that the above transformation has changed the shape and the dimension of the capacitor but has not led to any change in the capacitance. Therefore the capacitance of the original coplanar capacitor is equal to the capacitance of the parallel plate capacitor shown in the W-plane. Finally, it can be written as:

$$C_n = \frac{1}{2}\varepsilon\varepsilon_0 \frac{K(k)}{K(k')} \qquad (4.2.8)$$

The parameters K(k) and K(k') are the elliptic integrals and functions of s and g etc.

Apart from the "parallel-finger" part, the end of each finger and its neighbouring electrode "arm" will also form end capacitors. The calculation is possible by considering the end capacitor as a combination of a "dot" region with a regular field distribution at the end of the finger and two non-regular "dash" regions near the corners as shown in Figure 4.2.7. Formulae for the calculation of the capacitance under such consideration are available in reference [29]. In practice, however, the capacitance of the end capacitors is often neglected because it is only a small fraction of the total capacitance for an IDC with fingers much longer than the width (which is true for most real devices).

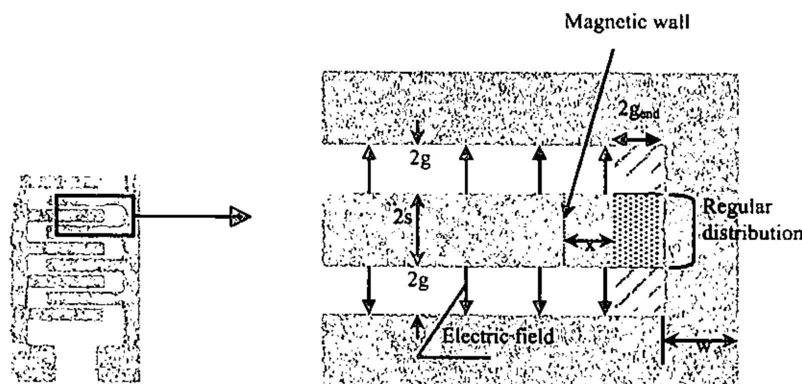


Figure 4.2.7 Considerations for the end capacitors [29].

Based on Gevorgian's model, a program (in Appendix) was developed for calculating the relative permittivity of the thin film from the capacitance of an IDC. The input data include relative permittivity of each layer except for the unknown material, the geometrical parameters of the IDC such as the finger "length", "width", "gap" and "finger number", the gap of the finger end, etc.

## 4.3 Dielectric properties of BST film

### *4.3.1 Dielectric characterization of BST in IDE/BST/LAO configuration*

The dielectric characterization of a typical sample, IDE/BST/LAO, is described as an example to demonstrate the procedure discussed in the previous section.

The fabrication of sample has been described in Chapter 3. Briefly, the BST layer was deposited by rf sputtering followed by annealing at 1000 $^{o}$C. The top electrodes (IDE, open and short references) were deposited by dc sputtering and patterned by standard photolithography and wet-chemical etching. Some geometric parameters of the IDC are:

BST film thickness: 200 nm

Substrate LAO: thickness ~ 500 μm, area = 1 cm by 1 cm

Interdigital electrodes: finger numbers = 20, finger width = 4 μm,

finger gap = 2 μm, finger length = 200 μm

After the 2-step calibration and the removal of the parasitic capacitance, the "main" IDC capacitance was obtained as shown in Figure 4.3.1(b). The raw data of magnitude of impedance |Z| for open, short references and IDE are shown in Figure 4.3.1(a).

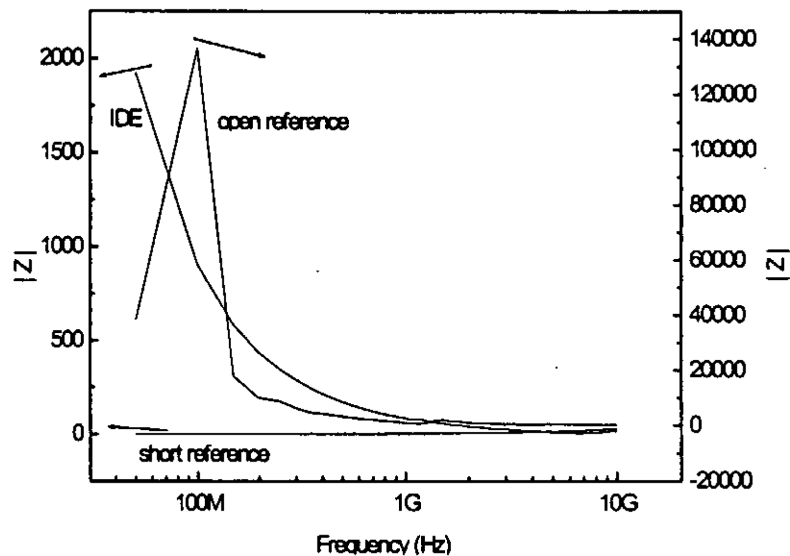


(a)

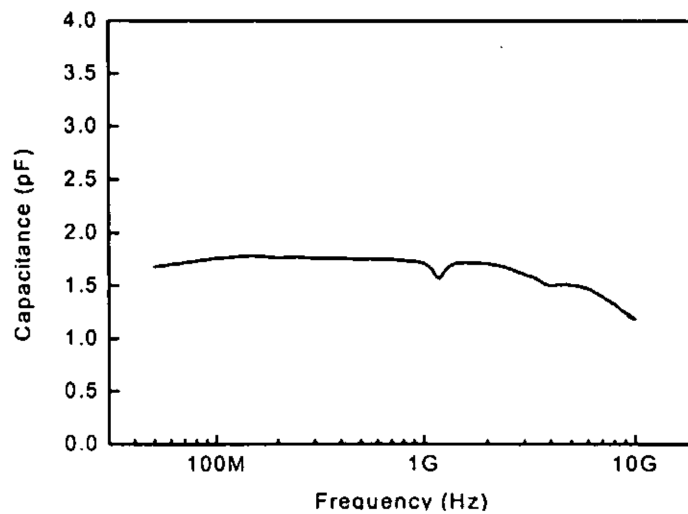


(b)

Figure 4.3.1 (a) Raw data |Z| of open, short references and IDE and (b) capacitance of the main IDC of BST/LAO as a function of frequency.

The relative permittivity of BST vs frequency was extracted and plotted in Figure 4.3.2. It is observed that the relative permittivity is about 400 and is quite constant when the frequency is below 2 GHz. A roll–off "V-shaped" shown around 1.3 GHz is very likely resulted from a weak resonance of the test circuit. When the frequency increases, the relative permittivity of BST gradually decreases until reaching the value of about 270 at 10 GHz.

Despite bulk $(Ba_{0.5}Sr_{0.5})TiO_3$ exhibits a high relative permittivity at room temperature (around 3000), the BST thin films often has a much lower relative permittivity due to various reasons such as defects, substrate clamping etc. Typical values of BST (50/50) thin films in the literature range from 200 to about 600, depending on the fabrication process and the substrate. Our result of $\varepsilon$ (BST (50/50)) = 400 can be regarded as in good agreement with the literature results [33]. The decrease of the relative permittivity at higher frequencies is also consistent with the dielectric relaxation phenomena that have been extensively reported in the literature [34].

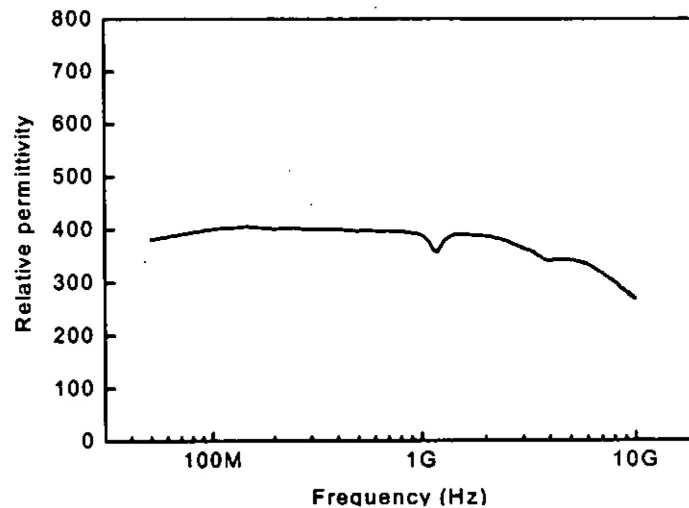


Figure 4.3.2 Relative permittivity of BST film as a function of frequency.

### *4.3.2 Influence of annealing temperature on the dielectric properties of BST*

The dielectric property of a ferroelectric thin film is dependent on the crystallinity of the material. A conventional method to investigate such relationship is to prepare the samples at different temperatures.

In our work, two different samples were prepared and measured by an Impedance/Material analyzer HP4291B at 10 MHz: i) IDC-Z: IDE/BST/$ZrO_2$ (the substrate is zirconia single crystal) and ii) Au/Cr/BST/Pt-Si (parallel plate capacitor). The structures of the samples are schematically shown in Figure 4.3.3.

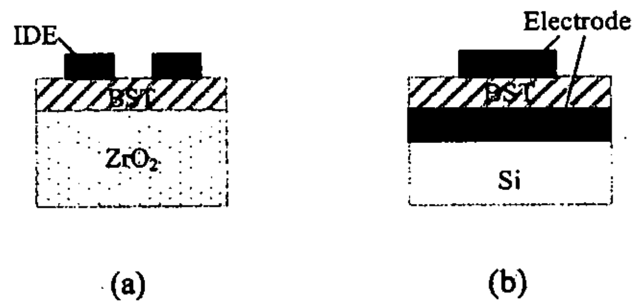


Figure 4.3.3 Cross-sectional views of the samples (a) IDC-Z and (b) parallel plate capacitor.

The samples were fabricated by conventional sol gel methods and patterning processes (details were given in Chapter 3). Two important technical issues are noted: 1). The composition of the film is $(Ba_{0.7}Sr_{0.3})Ti_{0.95}O_3$. The film is paraelectric at room temperature with its relative permittivity (obtained from dielectric tests on parallel plate capacitors) being insensitive to external ac field. This feature is important for this work because a strong ac field dependence of relative permittivity in the film will increase the complexity in the dielectric analysis. 2). The sol-gel technique was used in the sample preparation because this method ensures a good composition control of the films and the convenience of fabrication.

Figure 4.3.4 demonstrates the relative permittivity of BST as a function of annealing temperature. The common trend for both samples is that the relative permittivity increases with the annealing temperature. In the parallel plate capacitor,

BST annealed at 550 °C has a very low relative permittivity (around 100) but after being annealed at 650 °C, the relative permittivity became 370. For BST grown on $ZrO_2$ subjected to the same annealing temperature change, the relative permittivity increased from 240 to 380. The increase in relative permittivity with annealing temperature in our samples is a result of the improved crystallinity at higher temperatures [35]. For the same mechanism, a longer annealing time also increases the relative permittivity in all the samples.

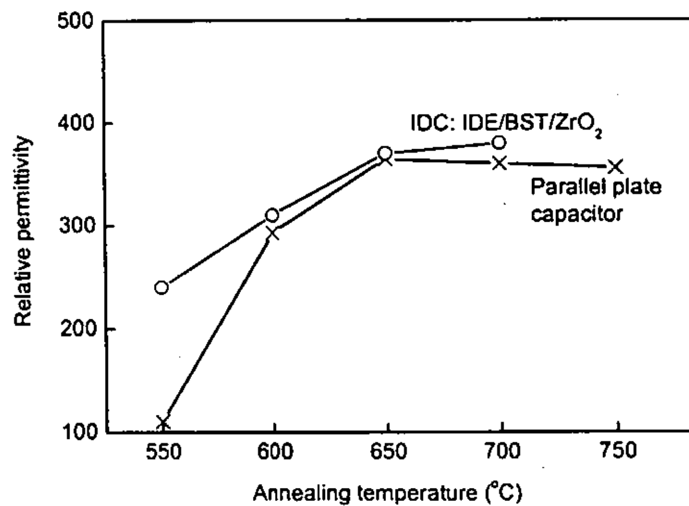


Figure 4.3.4 Relative permittivity of BST as a function of annealing temperature at 10 MHz.

### *4.3.3 Influence of film thickness on the dielectric properties of BST*

It is often observed in BST film-based parallel plate capacitors that the relative permittivity of BST is a function of the film thickness – the thicker the film, the larger the relative permittivity. This dependence is often explained as the result of the interface effect [36]. Because of the mismatch in composition and microstructure of BST and the substrate, there is an intermediate layer formed between "bulk" BST and the substrate after thermal treatment. The interface layer, having a much lower relative permittivity than the "bulk" BST is connected with BST in series and thus leads to the decrease in the relative permittivity of the whole capacitor. The thicker the whole film, the less influential the interface layer is. To demonstrate this phenomena, different thickness of samples were fabricated by the same method described in 3.2.2. From Figure 4.3.5, a similar thickness effect has also been observed in both of our parallel plate and interdigital capacitors. In the parallel plate capacitors, the relative permittivity was found to change from 280 for the 150 nm thick BST to 480 for a 300 nm thick BST. For BST/$ZrO_2$, the relative permittivity was found to change from 380 for the 150 nm thick BST to 540 for a 300 nm thick BST. Nevertheless, we are not sure if the thickness effects in the two different electrode configurations are based on the same mechanism. More work on the thickness effect in the IDCs as well as structural analysis will be carried out in the future to reveal the mechanism.

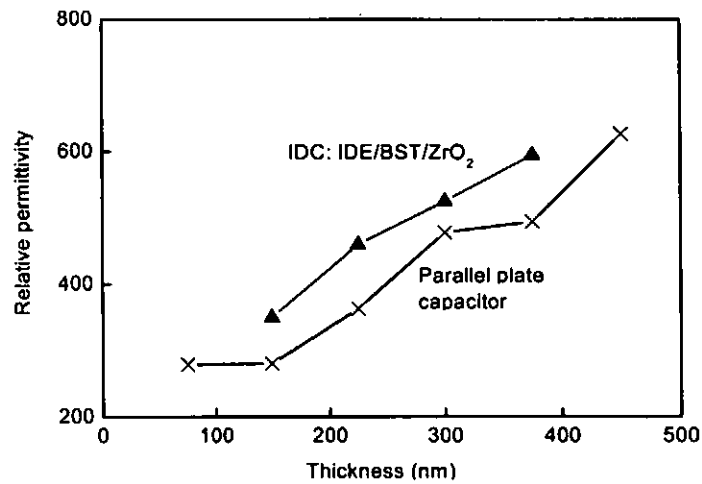


Figure 4.3.5 The influence of film thickness on the relative permittivity of BST on $ZrO_2$ and Pt-Si at 10 MHz.

## 4.4 Further discussion on IDC characterization

As mentioned before, the capacitance of an IDC has a very complicated relationship with the sizes of electrodes and the properties of the materials. In this section, such relationship will be discussed for the understanding and characterization of IDCs.

### *4.4.1 Influence of the air-filled capacitor*

In the partial capacitance techniques, the air-filled capacitor is considered as one contributor to the total capacitance of an IDC. This is one of the important difference

between an IDC and a parallel plate capacitor. For the parallel plate capacitor, it is not a capacitance contributor.

The following calculation by a program developed based on Gevorgian's model demonstrates the air-filled capacitor could affect the total device properties. The sample has a layered structure as shown in Figure 4.4.1.

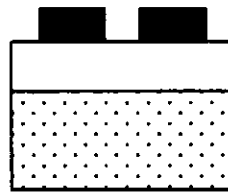

finger: width=10μm and gap=10μm

film: ε =280 and thickness=500nm

substrate: ε =25 and thickness=500μm

Figure 4.4.1 Layered structure and parameters for the calculation.

The parameter ΔC/C is the comparison of the IDC capacitance of any given electrode thickness with the capacitance of the standard IDC that has an electrode thickness = 10 nm. As shown in Figure 4.4.2, the capacitance of the IDC increases as the electrode thickness increases. The capacitance of the capacitor with 10 μm thick electrode is about 10 % larger than the capacitance of the capacitor with 1 μm thick electrode. Obviously the air-filled capacitor is the only part responsible for this change because the other parts of the device remained unchanged.

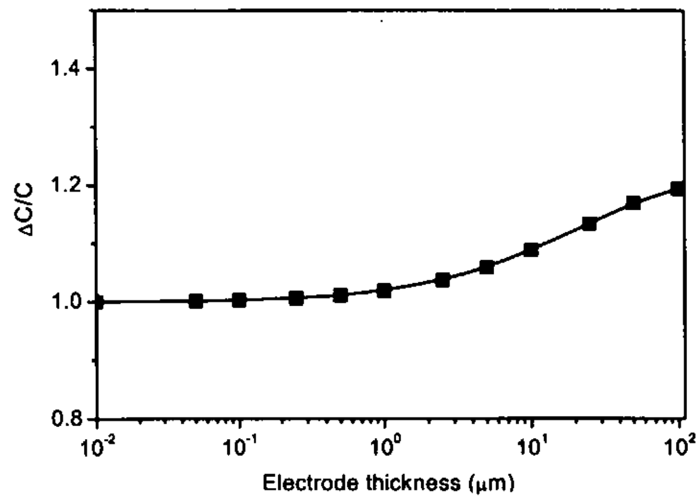


Figure 4.4.2 The changes of the capacitance due to the change in electrode thickness.

### *4.4.2 Dependence of capacitance on electrode size*

One possible way to improve the accuracy in the dielectric characterization of BST film is through the measurement and calculation of a series of samples with different electrode sizes. Usually the finger gap is the preferred parameter to be changed. Four samples with different finger gaps were prepared and measured. It is seen that the IDC capacitance increases as the finger gap decreases because in IDC with small finger gap, the effective electric field acting on the film increases and also less field can penetrate into the substrate. In Figure 4.4.3, the curves for the IDC with various film relative permittivity was calculated based on the program and plotted (line). Then the experimental data points (triangle) were inserted into the curve which showed that they fit well to the graph of $\varepsilon = 350$. We thus conclude that the relative permittivity of the BST film is 350.

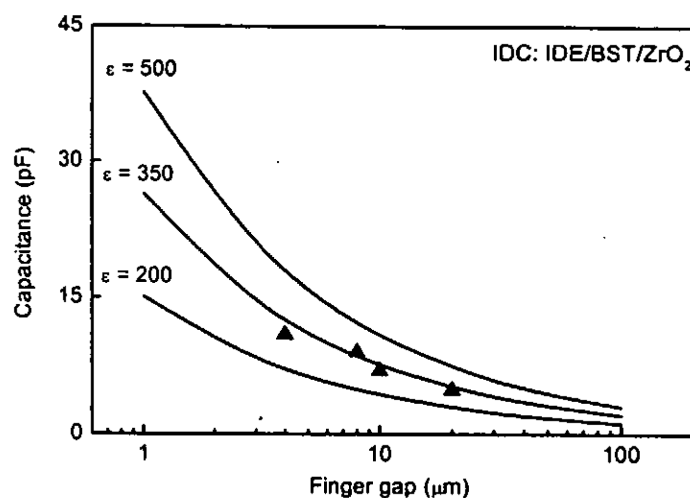


Figure 4.4.3 The dependence of the geometric factor on the finger gap in the IDCs.

### *4.4.3 Dependence of capacitance on film thickness*

Figure 4.4.4 shows the capacitance of IDC as a function of the film thickness. The results in the plot are calculated by a program developed based on Gevorgian's model. Some important parameters are:

Finger: width = 5μm

Film: ε = 350

Substrate: ε = 25, thickness = 500μm

In Figure 4.4.4, the capacitance of IDC increases as the film thickness increases because the thicker the film, more field lines pass through the film and the contribution from the film increases. Also, for the curves of different finger gaps, the

trends are similar because more field lines pass through the film when the gap is smaller.

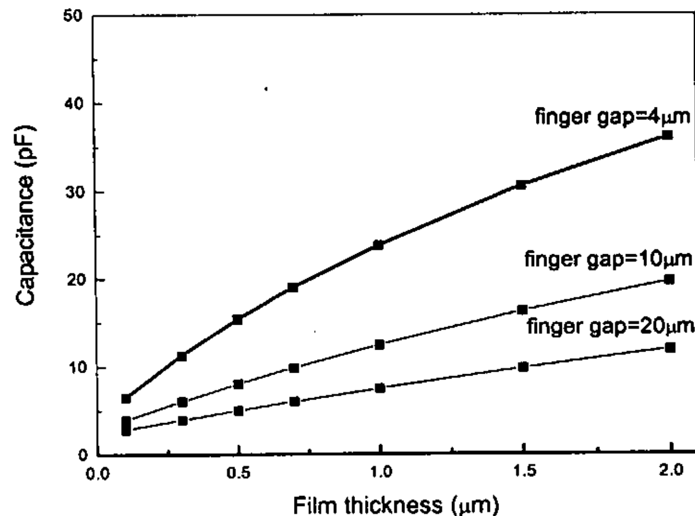


Figure 4.4.4 The dependence of capacitance on the film thickness in the IDCs.

## 4.5 Summary

In summary, the techniques and the procedure for the microwave dielectric characterization of BST thin film-based interdigital capacitors have been discussed. It was found that the relative permittivity of BST grown on LAO exhibited a relative permittivity of around 400. Also, several technical issues in the characterization of interdigital capacitors were discussed and compared with the conventional

ferroelectric thin film-based parallel plate capacitors. The observations were consistent with the values reported in the literature. Other issues on IDC characterization such as the dimensions of the IDC, electrode and film thickness have been discussed.

# Chapter 5

# The dielectric tunability of BST thin films

## 5.1 Introduction

The relative permittivity of ferroelectric materials is usually found to be strongly dependent on external electric field and it can be observed in two different ways: 1) By keeping the ferroelectric sample free of external dc bias, then it can be observed that the relative permittivity and the loss tangent increase with the test field (ac field) strength. 2) By keeping constant the measurement ac field amplitude and frequency, the relative permittivity and loss tangent will be found to decrease with the external dc bias. The dielectric tunability of ferroelectric thin films in most literature usually refers to the second case.

The dependence of the relative permittivity ε on the dc bias in ferroelectric materials is also a function of temperature. At temperature below $T_c$ (ferroelectric state), the ε-E dependence often exhibits a dual-peak as shown in Figure 5.1.1(a). When observed above $T_c$ (paraelectric state), the ε-E dependence is a single-peak as shown in Figure 5.1.1(b). Correspondingly the dielectric tunability is often defined differently as:

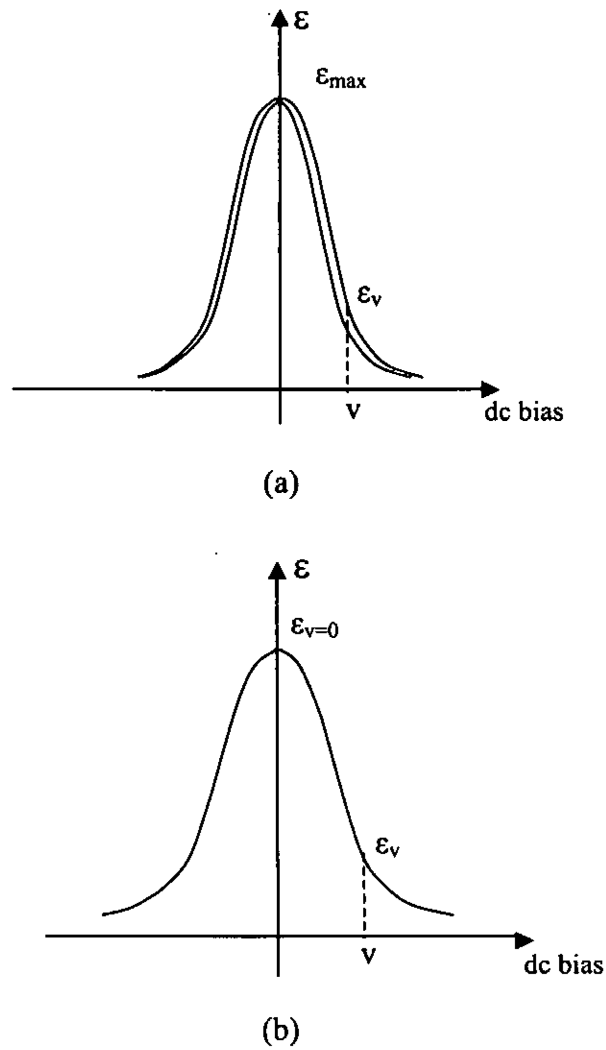


Figure 5.1.1 Dependence of ε on dc bias in ferroelectric materials: (a) below $T_c$ and (b) above $T_c$.

$$\text{Ferroelectric: } Tunability = \frac{\varepsilon_{max} - \varepsilon_{v}}{\varepsilon_{max}} \quad (5.1.1)$$

$$\text{Paraelectric: } Tunability = \frac{\varepsilon_{v=0} - \varepsilon_{v}}{\varepsilon_{v=o}} \quad (5.1.2)$$

where $\varepsilon_{V=0}$ is the relative permittivity of the material tested under zero dc bias, $\varepsilon_v$ the relative permittivity of the material tested under a dc bias voltage V, and $\varepsilon_{max}$ is the maximum relative permittivity. The material in a ferroelectric state always exhibits a larger dielectric loss than that in the paraelectric state. Therefore practically the materials for capacitive applications at high frequencies are often required to work in the paraelectric state. This is why most discussions on BST thin films for microwave devices in the literature have been focused on the single-peak case.

The origin of the dielectric tunability in ferroelectric materials has been discussed in the literature [37,38]. In thermodynamical theory, the behaviour of a ferroelectric crystal can be obtained by considering the form of the expansion of the free energy as a function of the polarization P,

$$F(P,T) = F_o + \left(\frac{1}{2}\right)\alpha P^2 + \left(\frac{1}{4}\right)\beta P^4 + \left(\frac{1}{6}\right)\gamma P^6 + \ldots \tag{5.1.3}$$

where $F_o$ is the zero field free energy density and the coefficients α, β and γ depend on the temperature. The powers of P are even because the free energy of the crystal will not change with polarization reversal. The equilibrium polarization in an electric field E satisfies the condition:

$$E = \frac{\partial F}{\partial P} = \alpha P + \beta P^3 + \gamma P^5 + ... \tag{5.1.4}$$

In ferroelectric state, α is negative while in the paraelectric state it is positive. α is dependent on the temperature,

$$\alpha = \frac{(T - T_0)}{\varepsilon_0 C} \tag{5.1.5}$$

where $T_0$ is equal to or lower than the actual transition temperature $T_c$ (Curie temperature) and C is a positive constant called the Curie-Weiss constant. The incremental relative permittivity in an electric field E is:

$$\frac{1}{\varepsilon_r(T,E)} \cong \varepsilon_0 \left(\frac{\partial E}{\partial P}\right)_T = \frac{(T - T_0)}{C} + 3\varepsilon_0 \beta P^2 + 5\varepsilon_0 \gamma P^4 + ... \tag{5.1.6}$$

the term $\frac{(T - T_0)}{C}$ is the incremental relative permittivity in the absence of a dc electric field. Using Equations (5.1.4) and (5.1.6), Johnson [38] proposed an expression for the relative permittivity in terms of the electric field as:

$$\varepsilon_r(T,E) = \frac{\varepsilon_r(T,0)}{\left\{1 + [\varepsilon_0 \varepsilon_r(T,0)]^3 B(T) E^2\right\}^{1/3}} \tag{5.1.7}$$

where B(T) is a phenomenological constant. Although these models were originally developed for ferroelectric crystals working at low frequencies, they are still good references for the understanding of the high-frequency dielectric behaviours of either ferroelectric or paraelectric BST thin films under dc bias.

The dielectric tunability of BST thin films in a parallel plate capacitor has been extensively investigated in the literature [39,40]. For BST thin films in coplanar capacitors, those techniques and results in the literature may serve as good references. In this Chapter, the high frequency dielectric tunability of BST thin films in interdigital capacitors was characterized and its relationship with structural factors, such as the film thickness and substrate was discussed.

## 5.2 Sample descriptions, dielectric measurements and data treatment

The samples for the tests have a regular interdigital capacitor structure, i.e. IDE/BST/substrate. In order to obtain a relatively high electric field, the capacitors were made to have an electrode gap of 2 μm (unless otherwise specified). The dielectric measurement was performed by a Hewlett Packard Impedance/Material analyzer HP 4291B (1MHz – 1.8GHz). The nominal electric field E, which is defined as the ratio of the voltage over the electrode finger gap of IDC, in our case: 40V/2μm is 20 MV/m. The nominal field E is schematically shown in Figure 5.2.1.

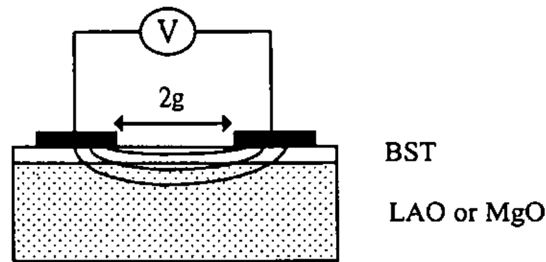


Figure 5.2.1 BST film-based IDC under test.

The dielectric measurements were carried out at room temperature. The measurement frequency was 800 MHz and the amplitude of the ac signal was always kept constant while the dc bias changed continuously.

For a parallel plate capacitor, the capacitance is proportional to the relative permittivity of the material. Therefore the dielectric tunability of the ferroelectric thin film is obtained by comparing the capacitances of the sample that are measured with/without a dc bias, i.e. $\Delta C/C$ (capacitor) = $\Delta\varepsilon/\varepsilon$ (ferroelectric film). For a coplanar capacitor, however, the dielectric tunability of the ferroelectric film is not equivalent to the relative capacitance change of the capacitor. This is because the substrate also contributes to the capacitance of the whole device. To remove the contribution of the substrate and obtain the dielectric tunability "purely" coming from the ferroelectric material, the programs based on Gevorgian's model was first used to calculate the relative permittivity. But the data treatment was time-consuming because each point on the C-E curve must be calculated individually. Therefore, a second simplified

method in data treatment was developed to calculate the tunability of BST as follows:

Step 1: The C-E dependences of both IDE/BST/LAO and IDE/LAO were obtained by the measurements.

Step 2: Under each particular dc bias V, the dielectric tunability of BST was obtained by comparing the capacitance as:

$$\frac{\Delta\varepsilon}{\varepsilon}(BST) = \frac{C_{IDE/BST/LAO(V=0)} - C_{IDE/BST/LAO(V)}}{C_{IDE/BST/LAO(V=0)} - C_{IDE/LAO}} \quad (5.2.1)$$

The validity of the Equation can be proven by the application of the partial-capacitance technique discussed in Chapter 4. As schematically shown in Figure 5.2.2, ($C_{IDE/BST/LAO}$ - $C_{IDE/LAO}$) represents the capacitance of a virtual capacitor, IDE/film, where the relative permittivity of the film equals to the term ($\varepsilon_{BST}$ - $\varepsilon_{LAO}$). As $\varepsilon_{BST}$ is always much larger than $\varepsilon_{LAO}$, therefore we have assumed that $\varepsilon_{BST} - \varepsilon_{LAO} \approx \varepsilon_{BST}$.

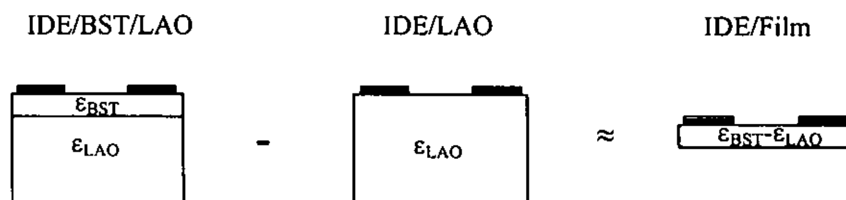


Figure 5.2.2 Extraction of the capacitance of the ferroelectric film.

Figure 5.2.3 demonstrates a practical example of the treatment procedure. Two samples were prepared: IDE/BST/LAO and IDE/LAO. BST film was fabricated by sputtering and its thickness was 300 nm. The electrode sizes for both capacitors are: electrode spacing = 2 μm, electrode width = 5 μm, finger number = 21. The C-E dependences of IDE/BST/LAO and IDE/LAO are shown in Figure 5.2.3(a) and (b), respectively. Obviously LAO does not exhibit any dielectric tunability in the measurement range. The difference between C(IDE/BST/LAO) and C(IDE/LAO) is shown in Figure 5.2.3(c). As previously analyzed, the data in Figure 5.2.3(c) is proportional to the ε-E dependence of BST and also using Equation (5.2.1), the dielectric tunability of BST can be obtained.

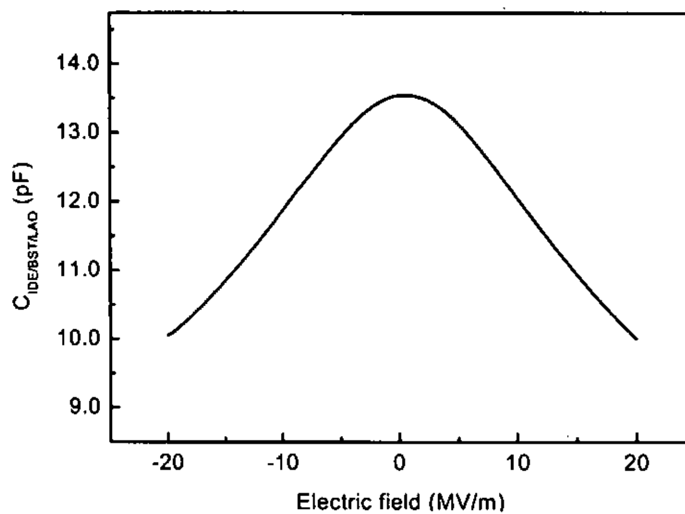


(a)

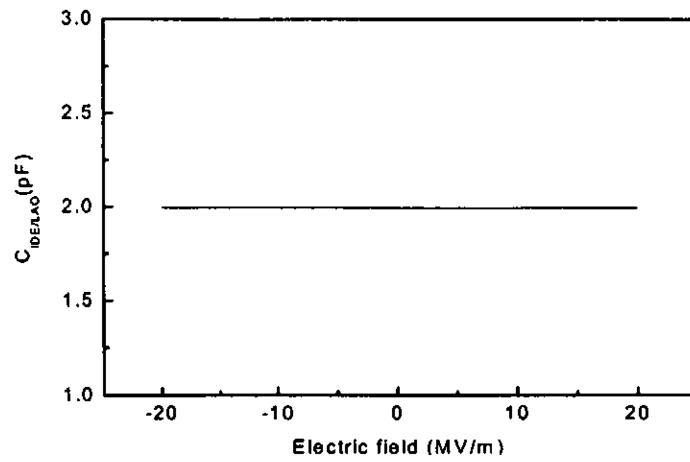


(b)

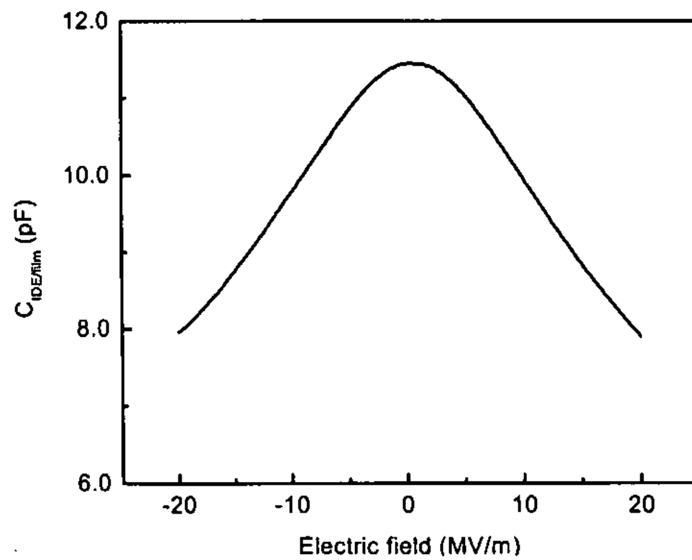


(c)

Figure 5.2.3 The C-E dependence of interdigital capacitors: (a) IDE/BST/LAO, (b) IDE/LAO and (c) IDE/film (virtual).

Table 5.1 shows the results of tunability of two samples: 220nm BST on LAO and 300nm BST on LAO calculated by different methods:

(1) The conventional method: $Tunability = \frac{\Delta\varepsilon}{\varepsilon}$

(2) $Tunability = \frac{C_{IDE/BST/LAO(V=0)} - C_{IDE/BST/LAO(V)}}{C_{IDE/BST/LAO(V=0)} - C_{IDE/LAO}}$

The percentage errors ($\frac{T1-T2}{T1} \times 100\%$) for both samples are within 2%. This method produces a convenient way to calculate the tunability in high accuracy and is less time consuming for data treatment.

Table 5.1 Calculated tunability from two different methods.

| BST film thickness | Calculated tunability from (1): at 20MV/m (T1) | Calculated tunability from (2): at 20MV/m (T2) | Percentage Error |
|---|---|---|---|
| 220nm | 26.22% | 26.24% | -2% |
| 300nm | 30.28% | 30.7% | -1.06% |

# 5.3 Typical value of dielectric tunability of BST and factors that affect the tunability

### *5.3.1 Assessment of the dielectric tunability of BST*

Figure 5.3.1 demonstrates the typical dielectric behaviour of BST thin films in the structure of IDE/BST/LAO. The relative permittivity shows a strong dependence on the dc bias with a value of 597 under zero dc bias. The maximum value of the tunability is about 31 % under a 20 MV/m electric field.

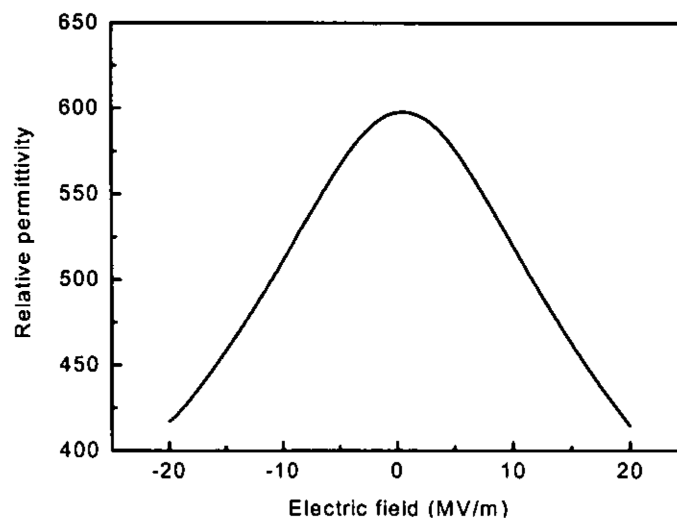


(a)

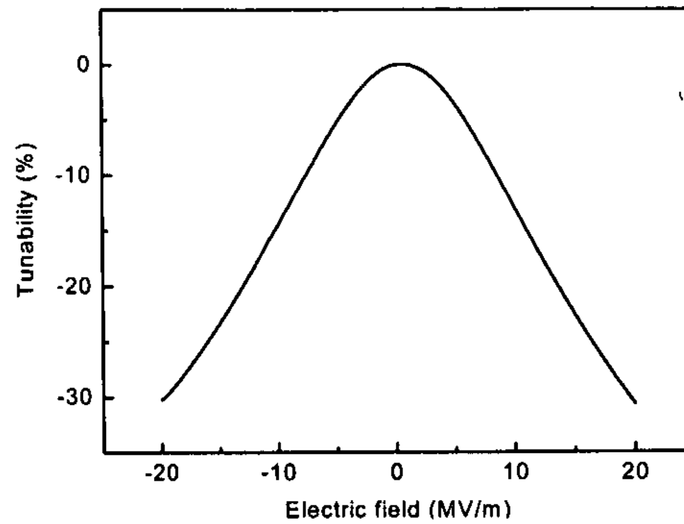


(b)

Figure 5.3.1 Typical dielectric behaviour of BST in the capacitor IDE/BST/LAO: (a) The relative permittivity and (b) the tunability.

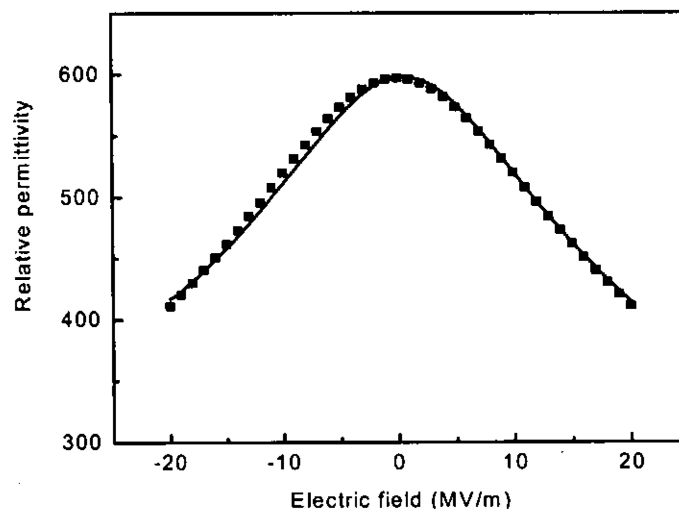


Figure 5.3.2 The experimental data (line) vs the calculated results (square dots).

The experimental data shown in Figure 5.3.1(a) are fitted to Equation (5.1.7). As shown in Figure 5.3.2, when $B = 3.5\times10^{10}$, the experimental data are well-fitted to the calculated results based on Equation (5.1.7). Both relative permittivity and the tunability of BST on LAO are comparable with literature data [40, 41]. Liu and co-workers have observed a tunability of BST about 16% at 20 MV/m with IDC structure [41].

### *5.3.2 Factors affecting the tunability of BST*

#### *5.3.2.1 Substrate effect*

Ferroelectric thin films are often found to be strongly dependent on the substrates mainly due to: 1) Stress is induced in the film due to the lattice mismatch and thermal mismatch between the film and the substrate. 2) The crystalline orientations of the films are largely controlled by the substrate. 3) Defects are formed near the interface region. As a matter of fact, the substrate effect in coplanar devices should be more significant because the ferroelectric thin films are directly grown on the substrates.

In this Section, the strong substrate dependence of the BST dielectric tunability was demonstrated. Two different samples were made and characterized in this experiment: IDE/BST/LAO and IDE/BST/MgO. The thickness of BST was 220 nm for both samples. The fabrication and characterization processes and the IDE sizes for both samples were kept exactly the same. As shown in Figure 5.3.3, BST on MgO

exhibits a much larger tunability (~46%) than BST on LAO (~26%) under the same electric field.

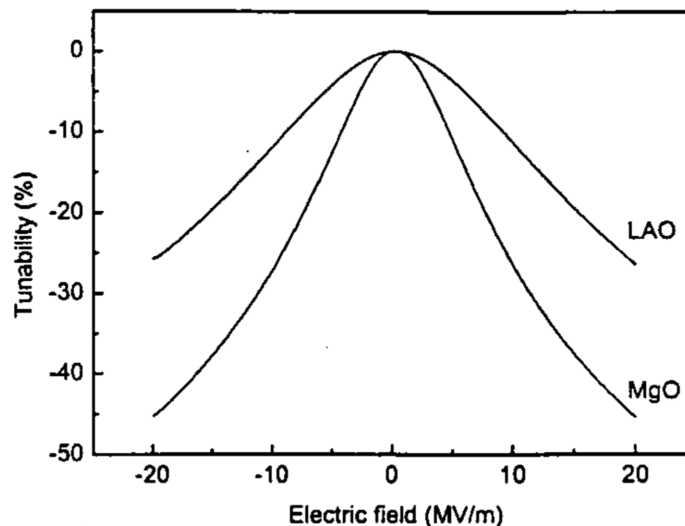


Figure 5.3.3 The dielectric tunability of BST on different substrates: LAO and MgO.

The mechanism responsible for the difference in the dielectric tunability of BST may be related to several microstructural factors. For BST on MgO, the lattice of MgO is about 7 % larger than BST and therefore BST tends to expand its lattice to match that of MgO. On the other hand, the thermal expansion coefficient of MgO is larger than BST, BST may be subject to a considerable stress due to the thermal mismatch. For BST/LAO, the case is exactly the opposite: the LAO lattice is smaller than BST and LAO has a thermal expansion coefficient slightly smaller than BST. The data of the three materials are shown in Table 5.2. Actually, it is hard to conclude how these factors may affect the structure and properties of BST. X-ray diffraction

(Figure 5.3.4) on the samples shows that the lattice of BST on MgO is larger than that of BST on LAO, indicating that the overall effect of the substrate is that BST on MgO is to a certain extent "expanded". Both of the films were highly oriented in the out-of-plane direction. Moreover, the BST thin film on MgO was subjected to the tensile stress because of the difference in thermal expansion coefficient. These could be the reasons why BST on MgO exhibited a larger tunability than BST on LAO. A more detailed discussion cannot be made until more microstructural analysis has been conducted.

Table 5.2 Lattice parameter (a) and thermal expansion coefficients (α) of bulk BST and the substrates.

| | LAO | MgO | Bulk BST (50/50) |
|---|---|---|---|
| a ($10^{-10}$m) | 3.787 | 4.213 | 3.947 |
| α ($10^{-6}$/°C) | 10.0 | 13.8 | 10.5 |

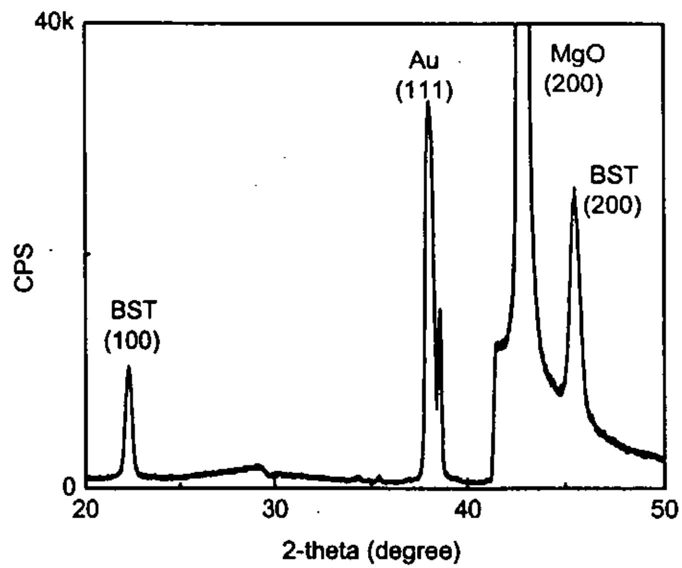


(a)

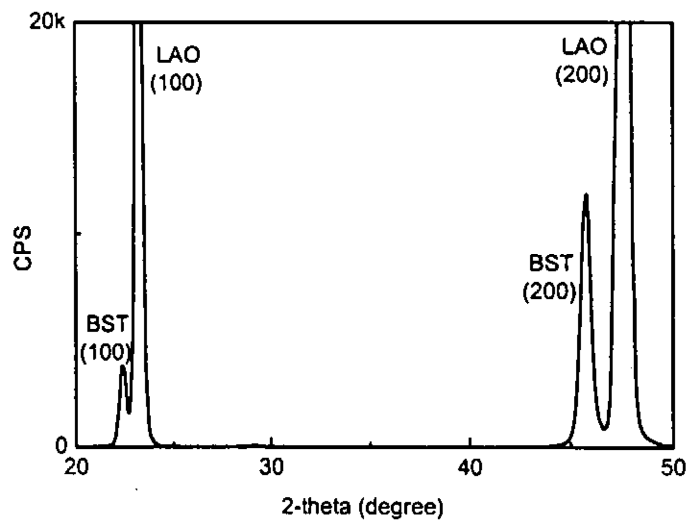


(b)

Figure 5.3.4 XRD of BST on (a) MgO and (b) LAO.

### *5.3.2.2 Dielectric tunability of BST prepared by the sol-gel method*

Although most of the BST thin films in this study were prepared by rf magnetron sputtering, the sol-gel techniques were also employed in the preparation of some of the BST thin films for comparison. Figure 5.3.5 demonstrates the dielectric tunability of a BST (50/50) thin film grown on LAO by the sol-gel technique. The film was annealed at 1000 °C for 3 hours and the film thickness was about 350 nm. The dielectric measurement was carried out at 800 MHz. As shown in Figure 5.3.5, the dielectric tunability (-37%) of sol-gel BST is quite similar to that of BST prepared by rf magnetron sputtering.

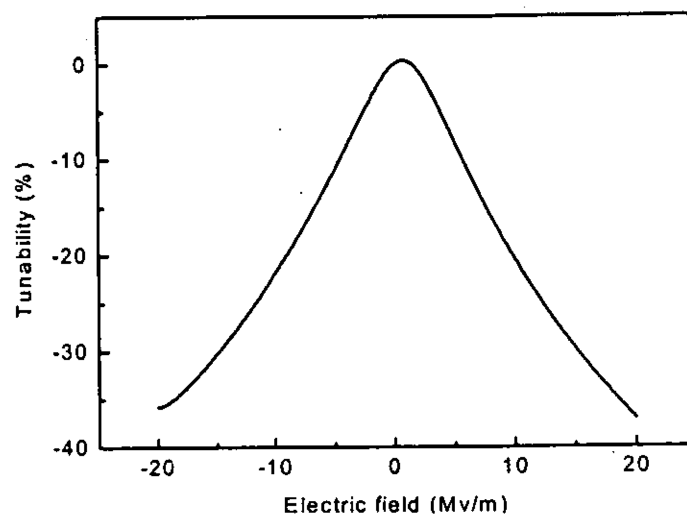


Figure 5.3.5 The dielectric tunability of sol-gel BST (50/50) on LAO.

Sol-gel BST films have a relatively poor morphology than that of films prepared by rf magnetron sputtering. The defect density and roughness on the sol-gel BST film surface is often too high for the electrode deposition. It becomes difficult to pattern the relatively small electrode spacing of the interdigital electrodes. Hence, the sol-gel method is not a favorable technique for making BST films for IDC devices.

*5.3.2.3 Tunability as a function of electrode spacing*

The electrode spacing was found to have an influence on the tunability of BST in an IDC. Figure 5.3.6(a) shows a typical experimental result. The tunability of BST in different samples was compared under the same dc bias voltage, the IDC with a larger electrode spacing exhibits a smaller tunability. When compared under the same nominal electric field, as shown in Figure 5.3.6(b), the tunability of BST in the 3-μm-spacing sample is larger than that in the 2-μm-spacing but almost the same as that in the 5-μm-spacing sample. The origin of the electrode spacing dependence of the tunability in IDCs is obviously related to the uneven distribution of the electric field in the ferroelectric thin film. Therefore the actual electric field strength in the film is much smaller than the nominal field strength, especially in the samples with small electrode spacing. Such effect is improved as the electrode spacing gets larger. To reach a certain required tunability, the driving field should be adjusted in terms of the electrode spacing of the device.

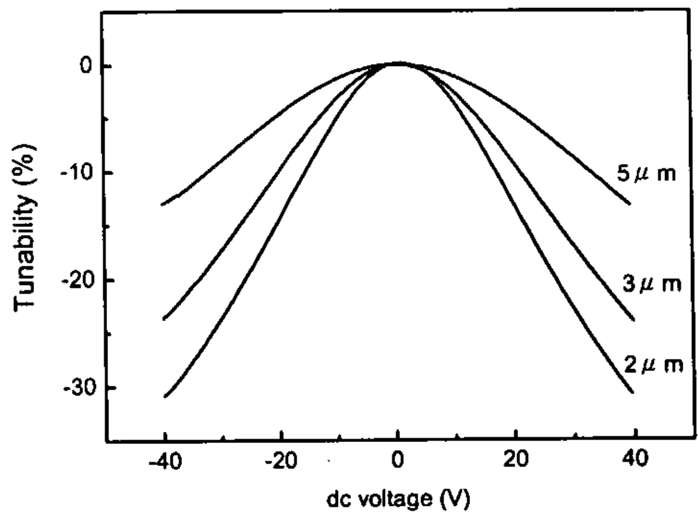


(a)

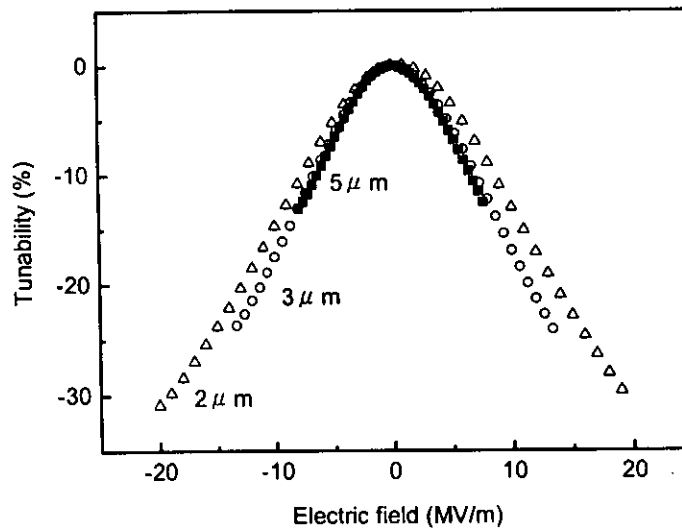


(b)

Figure 5.3.6 BST tunability in IDE/BST/LAO with different electrode spacings under different (a) dc bias voltages and (b) electric fields.

## 5.4 Dependence of BST tunability on film thickness

In the study of ferroelectric thin films, the thickness effect is an important issue. In the literature, the study of such effect is often conducted in the structure of electrode/ferroelectric film/electrode. In this work, a strong thickness dependence of the relative permittivity and tunability of BST in the coplanar structure IDE/BST/LAO has also been studied.

In this experiment, BST thin films of different thickness were prepared: 80 nm, 220 nm and 300 nm. All films were deposited on LAO substrate by rf magnetron sputtering. As shown in Figure 5.4.1, the relative permittivity and the tunability of BST increases with the thickness. For comparison, three groups of data are listed as below:

Table 5.3 Dielectric properties of BST films with different thicknesses.

| Film thickness | 80 nm | 220 nm | 300 nm |
|---|---|---|---|
| ε at zero bias | 285 | 553 | 597 |
| ε at 20 MV/m | 248 | 408 | 414 |
| Tunability under 20 MV/m | 13% | 26.2% | 30.7% |

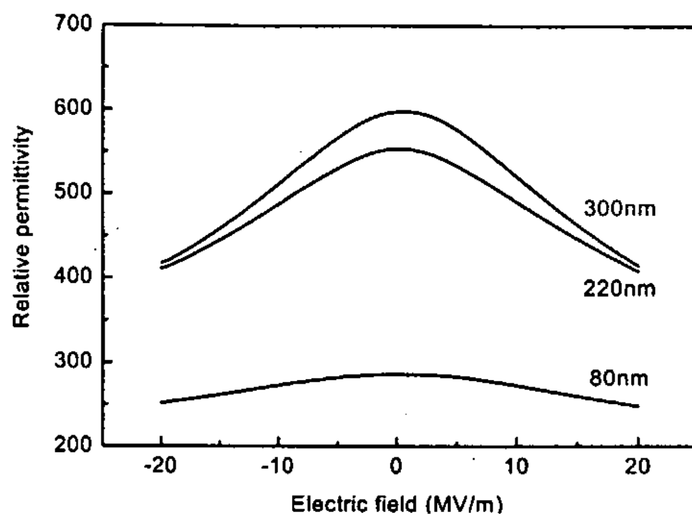


(a)

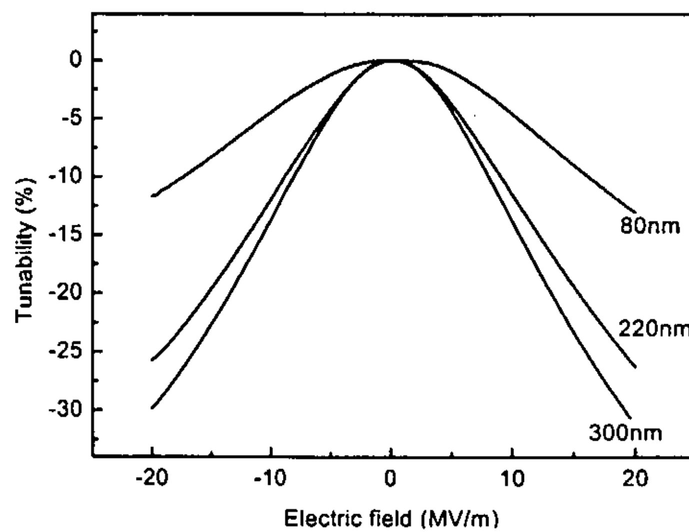


(b)

Figure 5.4.1 Influence of film thickness on the (a) relative permittivity and (b) tunability of BST in IDE/BST/LAO.

Table 5.3 lists the tunability as a function of the BST film thickness. Under a dc bias of 40V, the tunability of a 80 nm, 220 nm and 300 nm thick BST is about 13%, 26.2% and 30.7%, respectively. One main reason of the strong thickness dependence is believed to be contributed from the stress and interface states of the BST thin film. The stress in BST film is a function of the thickness. The thin BST film is subjected to a large stress and thus a strong clamping effect, leading to a poor dielectric tunability. As BST thickness increases, the clamping effect decreases and the tunability increases. The LAO substrate also has a considerable contribution to the total capacitance. Since LAO is not tunable under a dc bias, the overall tunability of the IDC will be lower for thinner BST film on LAO. As BST grows thicker, the contribution of the LAO substrate decreases and its influence on the tunability decreases, hence the device performance gets closer to pure BST.

## 5.5 Summary

In this Chapter, the dielectric tunability of BST thin films in interdigital capacitors was characterized. Under a 20 MV/m electric field, the tunability was found to be about 31%, a value comparable with most literature data. Many processing factors were found to have influences on the tunability of the films. The relative permittivity and tunability of BST exhibited a strong dependence on film thickness. The possible influences coming from the stress were discussed.

# Chapter 6

# BST thin film-based microwave devices

## 6.1 Introduction

BST thin film has attracted much research attention, especially in the microwave applications. BST thin-film based microwave devices such as varactors, resonators and filters offer the advantages of integratability, low cost and low voltage tunability. In this Chapter, BST thin film-based resonators and phase shifters have been studied.

Ring resonators are widely used microwave devices and also are tools for material characterization at high frequency. For example: it acts as a filter resulting in flatter passbands and higher out-of-band signal rejection. Other applications like wavelength-selective switching, amplification, and oscillation are also widely used.

Phase shifters produce various phase shifting of an output signal. They can provide compact and low power devices. The rapid advancement in telecommunication has called for the development of small size and cheap MMIC phased antennas for the information exchange between several satellites. They become key components in modern phased array antenna systems and telecommunication.

## 6.2 Issues on microwave measurement

Microwave testing of the device was performed by a network analyzer 8720ES (Agilent, USA) with a standard probe station Microtech RF-1 (Cascade, USA) and a pair of air coplanar ground-signal-ground (GSG) microprobes (Cascade, USA). For adding dc bias to the microwave measurement, an external dc power supply Agilent 6629A was used. The photographs of the GSG microprobe are shown in Figure 6.2.1. The tips of the microprobe are made of beryllium copper (BeCu), this type of tips are suitable for the use with gold pad as the contact substrate.

### *6.2.1 Important issues before calibration*

When the system has been connected and prior to calibration, the microprobe should be kept clean and there is a need for planarization. Planarization is to ensure all contacts are at the same height. As mentioned before, the gold contact substrate was used to planarize the microprobes. The planarity positioner on the probe station was adjusted to planarize the microprobes until all tips made even contact on the contact substrate. Figure 6.2.1(c) shows the microprobe marks on the contact substrate for even GSG contacts.

### *6.2.2 Calibration of the system*

The forward model of a two-port network analyzer is shown in Figure 6.2.2 [42]. The system was calibrated by short-open-load-through (SOLT) calibration to remove the parasitics of connection wire and probe, etc. This calibration is commonly used

for the two-port network analyzer. The calibration kit (calkit) of "open", "short", "load" and "thru" impedance standard substrates (ISS) was provided by the probe manufacturer and its information must be strictly followed. For example, "open" has negative capacitance and "short" and "load" have inductance. In the calibration, the automatic Cascade Microtech calibration software "WinCal" was used. The software provides the guideline of the calibration step by step. Figure 6.2.3 shows the calibration steps (open→load→short→thru) individually. In order to verify the calibration, it is recommended to re-measure the calibration standards substrates (ISS) and to model them using the calkit data of the probe manufacturer.

### *6.2.3 S-parameters*

Scattering parameters (S-parameters) are inherently linear quantities and often express themselves in a log-magnitude format. They are the reflection and transmission coefficients between the incident and reflection waves. They describe completely the behaviour of a device under linear conditions in the microwave frequency range. Each parameter is typically characterized by magnitude in decibel (dB) and the phase. The expression in dB is $20\log(S_{ij})$ where i, j = 1 or 2 because S-parameters are voltage ratios of the waves. The advantage of S-parameters does not only lie in the complete description of the device performance at microwave frequencies but also in its ability to convert to other parameters such as impedance (Z) parameters. Figure 6.2.4 shows the details of S-parameters such as equations, etc.

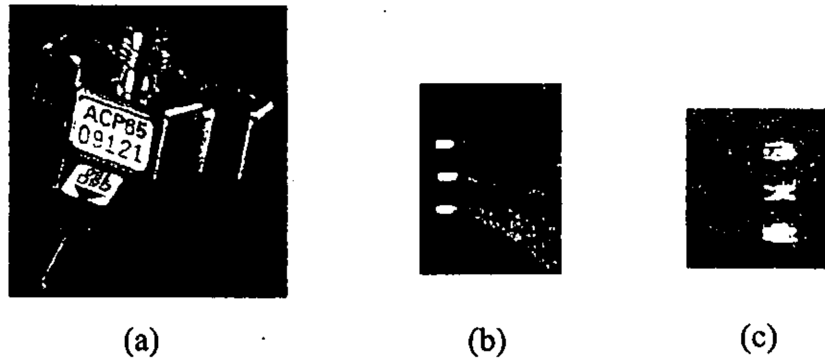


(a) (b) (c)

Figure 6.2.1 Photographs of the (a) GSG microprobe, (b) GSG microprobe tips and (c) GSG microprobe marks on the contact substrate [42].

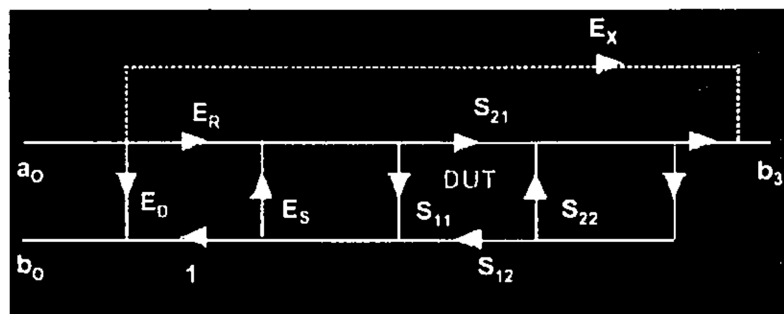


$E_R$ = frequency response of measurement channel, $E_S$ = Port match,
$E_T$ = models imperfections in transmission response, $E_D$ = Directivity of coupler
$E_L$ = models signal reflected back into DUT from P2
Calibrate with short-open-load on each port plus a Thru (SOLT) (use 10 knowns)

Figure 6.2.2 Two-port network analyzer model (Forward Model) [42].

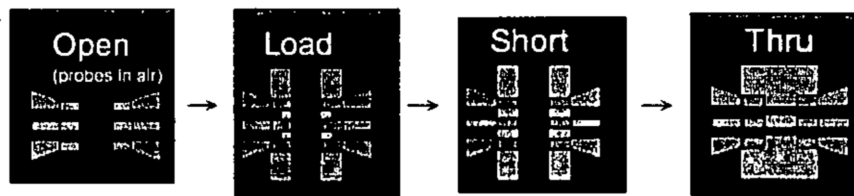


Figure 6.2.3 Different calibration steps: microprobe placed on different standard substrates: (open→load→short→thru) [42].

Measuring S-Parameters

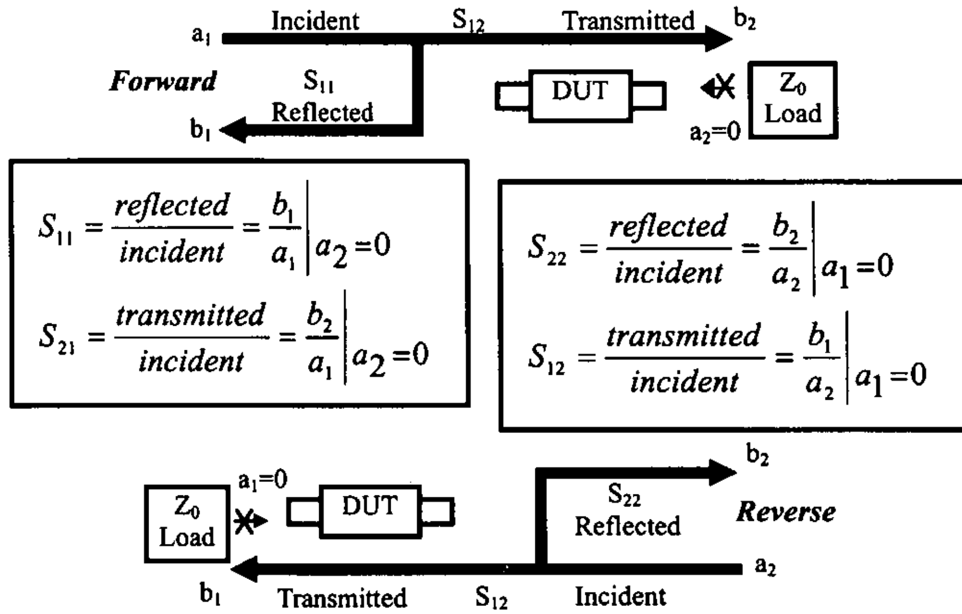


Measurement Terms

$S_{11}$=forward reflection coefficient (input match)

$S_{22}$=reverse reflection coefficient (output match)

$S_{21}$=forward transmission coefficient (gain or loss)

$S_{12}$=reverse transmission coefficient (isolation)

High-Frequency Device Characterization

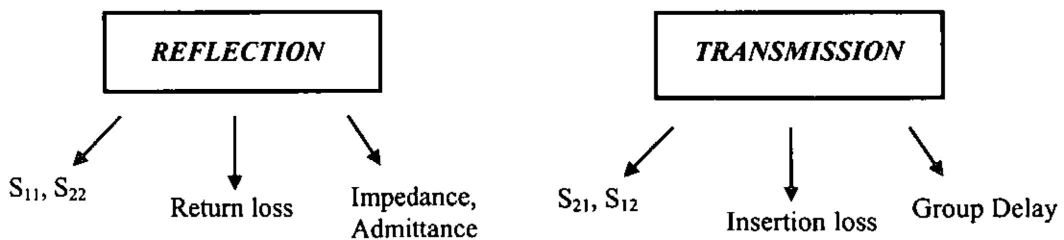


Figure 6.2.4 Detail information of S-parameters and device characterization.

## 6.3 Microwave devices

### *6.3.1 Ring resonator*

#### *6.3.1.1 Basic principle*

The ring resonator is a transmission line formed in a closed loop [43]. The basic circuit consists of the feed lines, coupling gaps and the resonator as shown in Figure 6.3.1. Power is coupled into and out of the resonator through the feed lines and coupling gaps. This type of coupling is referred to in the literature as "loose coupling" [43]. When the mean circumference of the ring resonator is equal to an integral multiple of a guided wavelength, resonance occurs. This may be expressed as:

$$2\pi r = n\lambda_g \tag{6.3.1}$$

for n = 1, 2, 3, ... where r is the mean radius of the ring that equals to the average of the outer and inner radii, $\lambda_g$ the guided wavelength and n is the mode number.

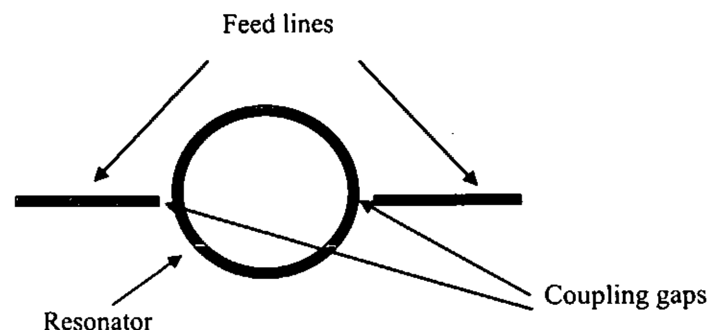


Figure 6.3.1 A ring resonator.

The ring resonators can be used to determine the phase velocity, Q factor and the relative permittivity in microstrip lines [44, 45]. In a nondispersive medium, frequency and the phase constant has a linear relationship. But in our case the microstrip line is on a dispersive medium. The dispersion in a microstrip line can be explained by examining the effective permittivity ($\varepsilon_{eff}$). In a microstrip line the effective permittivity is a measure of the field confined in the region beneath the strip. The effective permittivity is frequency dependent and defined as the square of the ratio of the velocity in free space (c) to the phase velocity in the microstrip ($v_p$),

$$\varepsilon_{eff}(f) = \left(\frac{c}{v_p}\right)^2 \tag{6.3.2}$$

by combining Equations (6.3.1) and (6.3.2) and $v_p = f\lambda_g$, the equation becomes

$$\varepsilon_{eff} = \left(\frac{nc}{2\pi r f}\right)^2 \tag{6.3.3}$$

the effective permittivity can thus be determined. The closed-form expression relating relative permittivity $\varepsilon$ of the substrate to $\varepsilon_{eff}$ has been derived by Hammerstad [46] for low permittivity materials as:

$$\varepsilon_{eff} = \frac{\varepsilon+1}{2} + \frac{\varepsilon-1}{2}\left[\left(1+\frac{12h}{W}\right)^{-1/2} + 0.04\left(1-\frac{W}{h}\right)^{2}\right] \qquad (6.3.4)$$

where W is the width of the microstrip and h is the thickness of the substrate.

*6.3.1.2 Ring resonator on a single crystal substrate*

For the sample in Figure 6.3.2, the ring resonator pattern on the LAO and MgO single crystals were formed by sputtering a layer of Au and then patterned by photolithography (details are given in Chapter 3) . Microwave testing of the resonator was performed by a network analyzer with a pair of GSG microprobes as shown in Figure 6.3.3. The system was calibrated by short-open-load-through (SOLT) calibration standards. The ring resonators were characterized by measuring the reflection and transmission scattering parameters ($S_{11}$ and $S_{21}$).

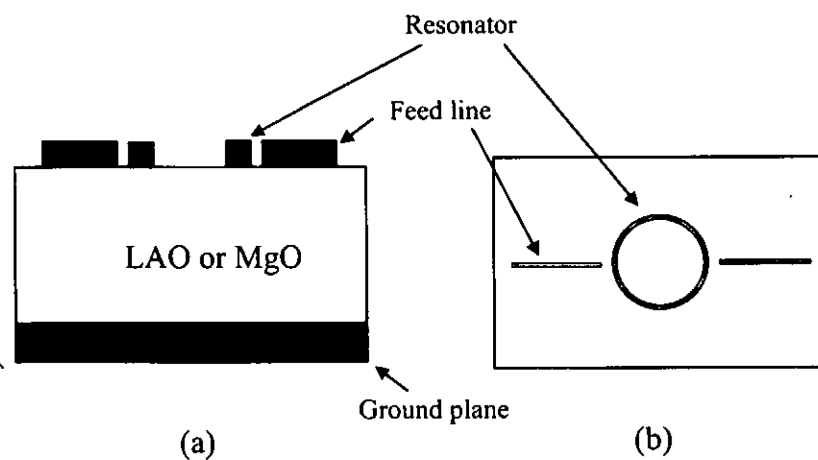


Figure 6.3.2 (a) Cross section and (b) top view of the sample.

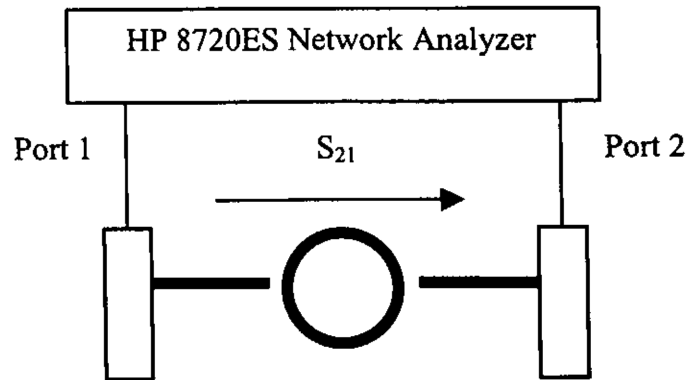


Figure 6.3.3 Experimental setup of the ring resonator measurement.

Figure 6.3.4 shows the result of scattering parameter $S_{11}$ with the change of the frequency. There are several modes of the resonant frequency for both resonators on LAO and MgO substrates. Table 6.1 lists the frequencies of the resonant modes.

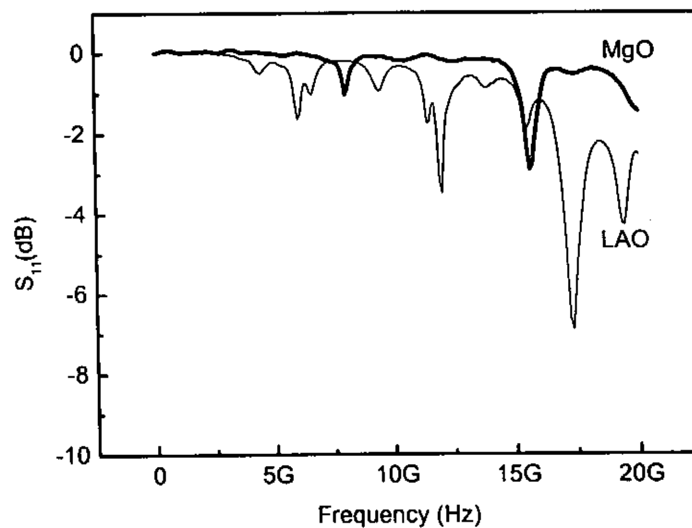


Figure 6.3.4 S-parameter against frequency of resonators on LAO and MgO.

Table 6.1 Resonant frequencies of several modes.

| | Resonant frequency (GHz) | |
|---|---|---|
| Mode number | on LAO | on MgO |
| 1 | 6.05 | 8.05 |
| 2 | 12.1 | 15.7 |
| 3 | 17.4 | - |

By using the data in Table 6.1 and the known dimensions of the ring resonator:

Outside diameter: 5mm
Inside diameter: 4.6mm
Feed line strips: 0.05mm*1mm
Coupling gaps: 0.015mm
Microstrip width: 0.4mm

from Equations (6.3.3) and (6.3.4), relative permittivity of the substrates were calculated and shown in Figure 6.3.5. The calculated relative permittivity was (16.5-18.1) for LAO single crystal and (9.08-9.55) for MgO single crystal. The low-frequency relative permittivity of LAO and MgO single crystals are 24.5 and 9.8 respectively. The results obtained seemed to be quite reasonable.

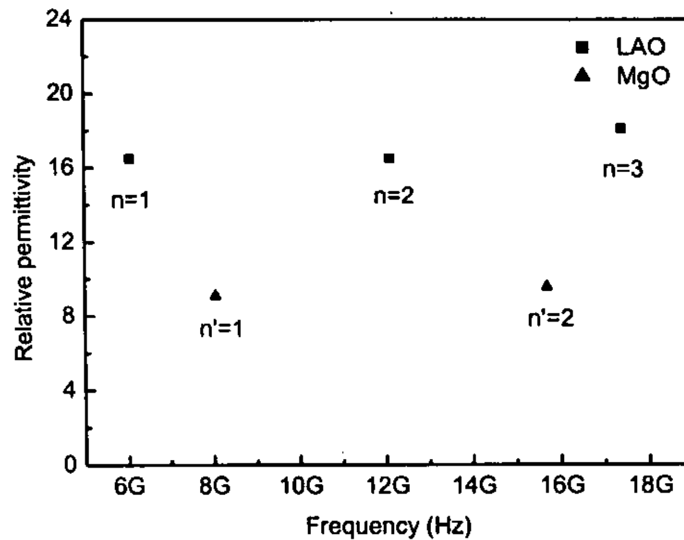


Figure 6.3.5 Calculated relative permittivity at different resonant frequencies.

*6.3.1.3 Resonant frequency vs film thickness*

For the sample with the structure: electrode (resonator)/BST/LAO/electrode (grounding), the overall relative permittivity ($\varepsilon_{overall}$) of the whole sample (BST+LAO) is dependent on the BST film because the relative permittivity of LAO is a constant (~24.5). It is expected that the thicker the BST film, the larger is the relative permittivity. For example: $\varepsilon_{overall}$ of 500 nm BST on LAO should be larger than $\varepsilon'_{overall}$ of 100 nm BST on LAO. From Equation (6.3.3), it indicates that the resonant frequency increases as the effective permittivity decreases. This phenomena is consistent with our results shown in Figure 6.3.6. There is a resonance shift for different thicknesses of BST thin film on LAO with the same resonator structure. For a 180 nm BST film sputtered on LAO, the first resonance occurs at 5.25 GHz while

for a 300 nm BST film sputtered on LAO, the first resonance is found at 4.99 GHz as listed in Table 6.2. These phenomena can be explained as due to the difference in their overall relative permittivity. It provides an ability to tune the position of the resonant frequency by adjusting the thickness of the thin film of the device.

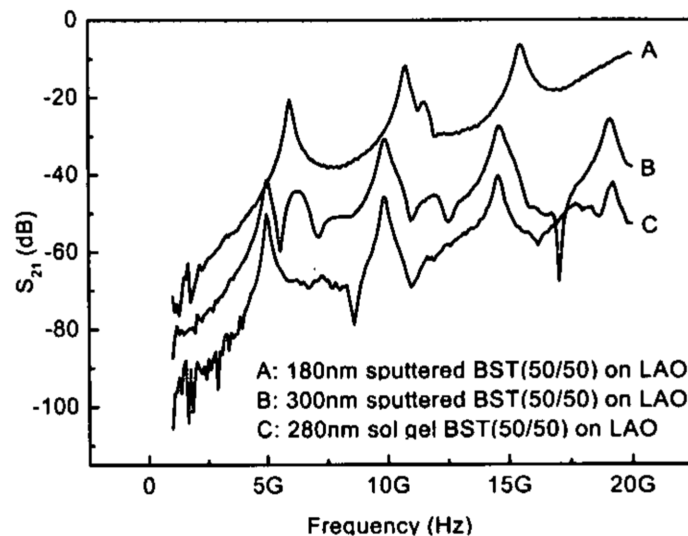


Figure 6.3.6 Film thickness dependence of the resonant frequency.

Table 6.2 Several resonant modes.

| | Resonant frequency (GHz) | | |
|---|---|---|---|
| Mode number | 180 nm BST | 280 nm BST | 300 nm BST |
| 1 | 5.25 | 4.99 | 4.99 |
| 2 | 10.35 | 9.83 | 9.93 |
| 3 | 15.35 | 14.59 | 14.59 |

Because the sample has a multilayer structure, the relative permittivity of BST thin film cannot be directly calculated from Equations (6.3.3) and (6.3.4). A commercial electromagnetic simulator, IE3D (Zeland Software, Inc.) was used to perform the full-wave electromagnetic simulation, which was based on an integral equation obtained through the use of Green's functions and the method-of-moment formulation for a full-wave solution [47]. Electromagnetic simulation is a new technology to yield high accuracy analysis and design of complicated microwave and other electronic components. IE3D is an integrated full-wave electromagnetic simulation and is an optimization package for the analysis and design of 3-dimensional microstrip antennas etc. In our case, it was used to simulate the $S_{21}$ spectra of the ring resonators and fitted the results to obtain the relative permittivity of the BST thin film. Briefly, an incident field was imposed on the ring structure, inducing a current distribution. To make the secondary field created by the induced current satisfy the boundary condition, an integral equation in terms of dyadic Green's functions for the current was obtained. With the use of a set of rooftop basis functions on a triangular and rectangular mixed non-uniform grid, the current distribution on the ring structure was solved by means of the method-of-moment formulation. After the current distribution was solved, the circuit parameters of the structure can be expressed in S-parameter form [47, 48].

In the simulation, it is required to provide some parameters. For example: the dimensions of the ring resonator (feed lines, resonator and size of the gap), dielectric

properties of each layer and operated frequency range etc. By inputting the relevant parameters of sample B in Figure 6.3.6. Figure 6.3.7 shows the result of experimental data with the simulated data. The relative permittivity of 300 nm BST (50/50) thin film sputtered on LAO was found to be 550. This result is reasonable when compared with the literature and previous results obtaining from the IDE pattern.

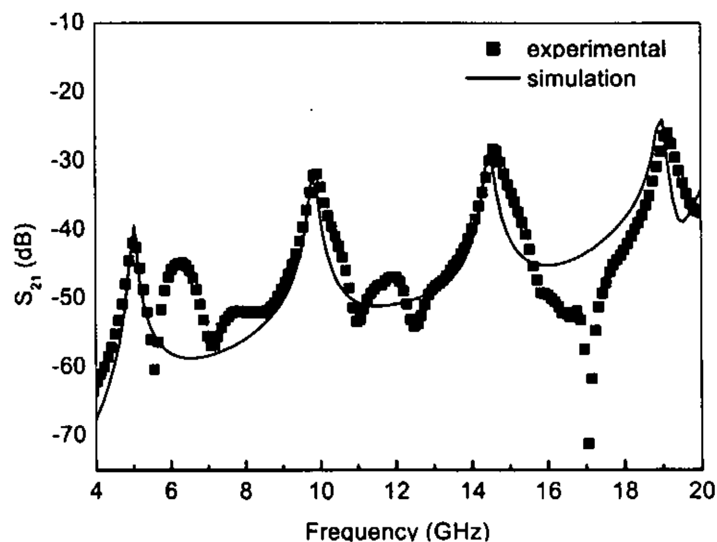


Figure 6.3.7 Experimental data and simulation results of ring resonator on the 300 nm sputtered BST thin film/LAO/Au.

### *6.3.2 Phase shifter*

#### *6.3.2.1 Basic principle*

Figure 6.3.8 shows the structure of a coupled microstrip phase shifter (CMPS). The phase shifter design consists of eight coupled microstrip sections in series. Each section functions as a single pole broadband filter whose passband shifters with the dc bias applied to the ferroelectric film. The phase shift is proportional to the number of coupled microstrips. These phase shifters are fairly narrowband and the optimal frequency $f_{opt}$, depends upon the relative permittivity and the thickness of the ferroelectric film. Considering a simple case of the structure as shown in Figure 6.3.9 [49, 50], the coupled microstrip geometry can be excited in two modes: even and odd. The propagation constant is given by,

$$\beta = \frac{\omega}{v_p} = \left(\frac{\pi}{\lambda_o}\right)\left[\left(\varepsilon_{even}\left(V_{dc}\right)\right)^{0.5} + \left(\varepsilon_{odd}\left(V_{dc}\right)\right)^{0.5}\right] \tag{6.3.5}$$

where $\lambda_o$ is the free space wavelength, $v_p$ the phase velocity, $\varepsilon_{even} = C_e/C_{e-air}$ and $\varepsilon_{odd} = C_o/C_{o-air}$ ; $C_{e\text{-air}}$ and $C_{o\text{-air}}$ are obtained by replacing all dielectrics with air. In the odd mode, the E-fields are concentrated in the ferroelectric film. By applying a dc voltage between the two microstrips, ε of the ferroelectric material between the lines can be tuned. Briefly, a dc bias is applied between the coupled microstrips, strongly affecting the relative permittivity of the ferroelectric film in the gap and causing a

microwave phase shift. Larger phase shifts are obtained by placing several of these coupled microstrip sections in series. However, coupled microstrip phase shifters require careful design because they are inherently filters with a limited bandwidth.

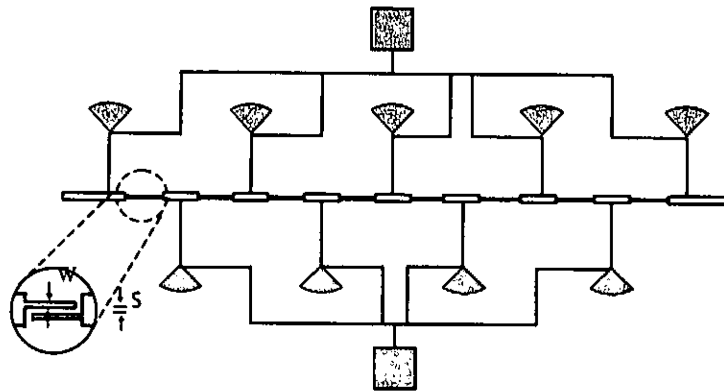


Figure 6.3.8 Schematic diagram of the eight coupled microstrip phase shifter design (W = 25μm and s = 8μm).

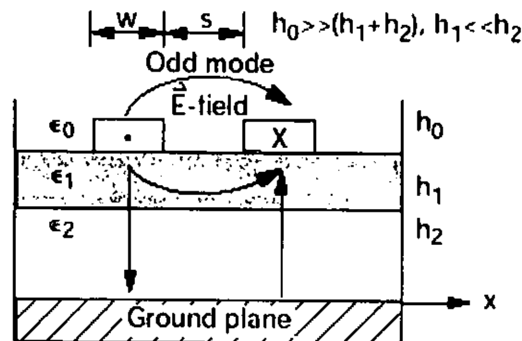


Figure 6.3.9 A coupled microstrip ferroelectric phase shifter. The E-fields are drawn for odd mode propagation [49].

*6.3.2.2 Phase shifter on BST thin film*

The phase shifter has a structure of: electrode (phase shifter)/BST/MgO/Au (grounding). BST (50/50) thin film was deposited on the MgO substrate by rf magnetron sputtering and patterned by the standard photolithography. The performance of the phase shifter was evaluated by measuring the differential phase shift using a network analyzer and a pair of GSG microprobes. Figure 6.3.10 shows the measured phase shift with the change of frequency controlled continuously with dc voltages up to 100 V. As shown in Figure 6.3.11, a maximum differential phase shift of 223° can be obtained at 15.05 GHz. To calculate the figure-of-merit (FoM) of a phase shifter, the equation can be defined as the quotient of the differential phase shift (ΔΦ) and the insertion loss (α):

$$FoM = \frac{\Delta\Phi}{\alpha} \quad [\text{degree/dB}] \tag{6.3.6}$$

At 15.05 GHz, the differential phase shift is 223° and the insertion loss is 21.7dB under a dc bias of 100 V, the figure-of-merit of this phase shifter is about 10°/dB. In fact, this value can be improved:

(1) Through material optimization.

(2) By applying higher dc voltage and using smaller coupled gap in the microstrip ( "s" in Figure 6.3.8) to increase the electric field.

(3) By lowering the microwave metallic losses through increasing the electrode

thickness.

Here, it is aimed at demonstrating the preliminary performance of the BST phase shifter. By tuning the above parameters, better results can be obtained.

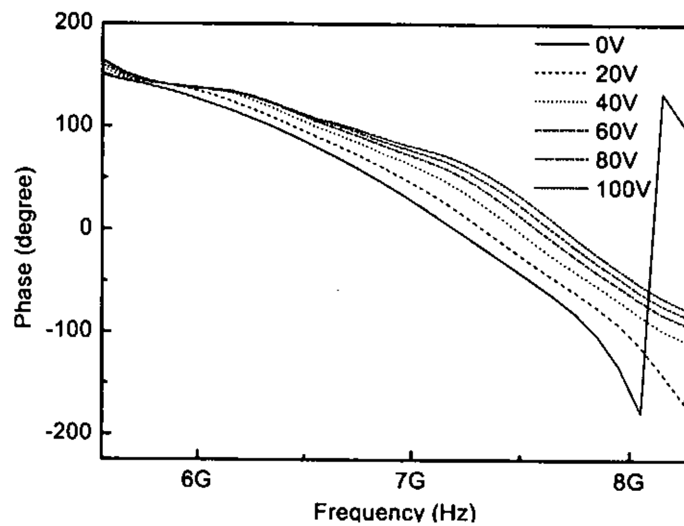


Figure 6.3.10 Phase shift vs frequency for different dc bias.

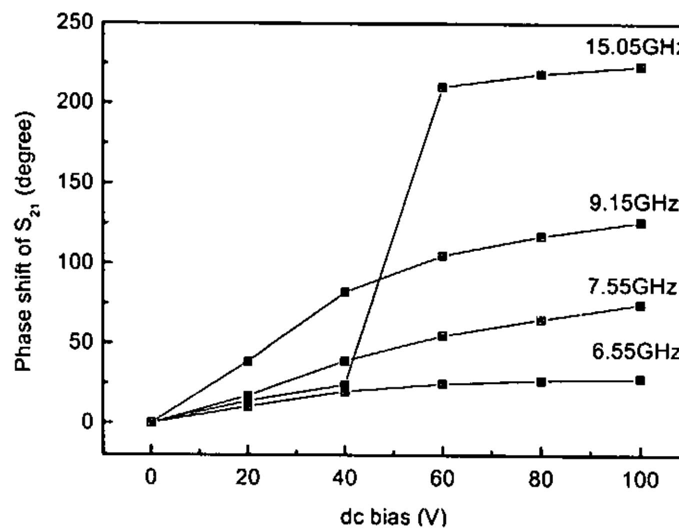


Figure 6.3.11 Differential phase shift vs dc bias at different frequencies.

## 6.4 Summary

In this Chapter, the basic concepts of BST thin-film based microwave devices were introduced. The performance of ring resonator on different structures were investigated and studied with the aid of the commercial simulation software IE3D. Also, the BST thin film-based phase shifter under dc bias has been preliminarily developed and described.

# Chapter 7

# Conclusions

## 7.1 Conclusions

In this study, BST thin films have been deposited by the rf magnetron sputtering and sol gel techniques. Using rf magnetron sputtering, BST (50/50) thin films were deposited on a heated substrate at 450°C and post annealed at 1000°C for 3 hours. XRD showed that the film has the perovskite structure and AFM study indicated that the film has uniform grain size and low roughness. The substrate heating during deposition and post annealing are critical to the properties of the BST thin films. Without substrate heating, the film has poor crystallization and higher post annealing temperature increased the roughness of the film. The parameters of sputtering should be well controlled. For the sol gel techniques, the commercial sol gel solutions BST (70/30/95) and BST (50/50) were spun on the substrates and pyrolyzed in RTA with $O_2$ atmosphere. The spin-coating steps were repeated until the desired thickness has been reached. Finally, the films needed to be post annealed to enhance the crystallization. XRD showed that the films were well crystallized.

The electrode patterning by standard photolithography was described. The layer of Au electrode was first deposited on the top of the sample by magnetron sputtering.

This was followed by spin-coating of photoresist, UV exposure and development. The pattern was defined after the chemical wet etching procedure. The parameter control in the process, such as the development and etching time, was very important, especially for the electrode patterns with smaller dimension.

The relative permittivity of BST thin film at microwave frequency was determined by an interdigital electrode structure. A simple measurement technique of "open" and "short" references was used to remove the parasitic capacitance. The pure capacitance attributed to the "finger" part of the IDE was obtained. Then, Gevorgian's model was introduced to extract the relative permittivity from the capacitance. The relative permittivity of a 200 nm BST (50/50) thin film sputtered on LAO was found to be ~400 and a dielectric relaxation phenomena was observed at higher frequency. The processing-structure-property relationship of the IDC was studied. The films annealed at higher temperature had higher relative permittivity. The relative permittivity increased as the film thickness increased. These observations were consistent with the conventional thin film-based parallel plate capacitors. Other issues on IDC characterization such as the electrode thickness and the dimensions of the IDC have been discussed. The capacitance increased as the electrode and film thickness increased but decreased as the finger gap increased.

The tunability of BST thin film using interdigital electrode structure has been characterized. Under a field of 20 MV/m, in the 300 nm BST thin film sputtered on

LAO substrate, the tunability was found to be 31%. This value is comparable with the literature result. The substrate effects on the tunability of BST thin film have been studied. The tunability of 220 nm BST sputtered on LAO and MgO substrates were found to be ~26% and ~46%, respectively. The 350 nm thick BST film on LAO prepared by the sol gel techniques has a tunability of ~37%. Also, at the same applied voltage the tunability was found to be a function of the electrode spacing, the smaller the spacing of IDE the larger the tunability. The thickness dependence of tunability has been discussed. The thicker the BST thin film the larger the tunability. The possible influences coming from the stress were discussed.

BST thin film-based microwave devices such as resonator and phase shifter have been studied. Ring resonator acted as a tool for materials characterization was discussed. For the ring resonators directly fabricated on LAO and MgO substrates, the relative permittivity of LAO and MgO were found to be (16.5-18.1) and (9.08-9.55), respectively which are reasonable results. The performance of ring resonators on different structures were investigated and studied with the aid of a commercial simulation software IE3D. The resonant frequency shifted with different BST thin film thickness. For a 180 nm BST film sputtered on LAO, the first resonance occured at 5.25 GHz while for a 300 nm BST film sputtered on LAO, the first resonance was found at 4.99 GHz. These phenomena can be explained as due to the difference in their overall relative permittivity. A commercial software IE3D was used to simulate the $S_{21}$ spectra of the ring resonators and fitted the results to obtain the relative

permittivity of the BST thin film. The relative permittivity of a 300 nm BST (50/50) thin film sputtered on LAO was found to be 550. This result is reasonable when compared with the literature and our results obtaining from the IDE pattern. On the hand, the performance of the phase shifter was evaluated by measuring the phase shift with the change of frequency controlled continuously with external dc voltages up to 100 V. A maximum differential phase shift 223° and an insertion loss of 21.7dB can be obtained at 15.05 GHz under a dc bias of 100V. The figure-of-merit of this phase shifter was about 10°/dB. This was a preliminary demonstration of the performance of the BST phase shifter. By tuning some parameters, better results can be obtained.

## 7.2 Suggestions for future work

Further investigations on the IDC and the performance of the BST thin film-based microwave devices suggested for future work include:

(1) To investigate the thickness effect in the IDC to reveal the mechanism causing the relative permittivity increase.

(2) To investigate the mechanisms for the substrate effect in the IDC which give rise to the larger tunability of BST on MgO than that on LAO.

(3) Materials optimization by doping MgO and $Al_2O_3$ etc into the BST thin films to lower the relative permittivity and loss while retaining its tunability for microwave applications.

(4) To optimise the design of the coplanar electrode pattern e.g. using

smaller electrode gap in the phase shifter to obtain higher electric field. This will increase the range of tunability of the device as the applied voltage was limited by the measurement equipment. Fabrication and characterization of other microwave devices preferably those that actually may be used in practical circuits will be our future goal. Also, increasing the electrode thickness will be the most essential part of the work.

(5) To further develop measurement techniques of the microwave testings such as the extraction of useful data by removing the parasitics etc to obtain more accurate properties of the BST thin films and devices. Also, to extend the measurement techniques to cover a wider range of frequencies, dc bias voltages and temperatures.

# References

[1] H. D. Wu, Z. H. Zhang, F. Barnes, C. M. Jackson, A. Kain and J. D. Cuchiaro "Voltage tunable capacitors using high temperature superconductors and ferroelectrics". *IEEE Transactions on Applied Superconductivity,* Vol. 4, pp. 156-160 (1994)

[2] E. J. Cukauskas, S. W. Kirchoefer and J. M. Pond "Magnetron sputtered $Ba_{(1-x)}Sr_xTiO_3$ thin films". In S. K. Streiffer, B. J. Gibbons, T. Tsurumi, ed., *Proceedings of the 2000 12th IEEE International Symposium on Applications of Ferroelectrics*, Honolulu, HI, USA, 21 July-2 Aug., 2000, pp. 875-878 (2001)

[3] J. Im, O. Auciello, P. K. Baumann, S. K. Streiffer, D. Y. Kaufman and A. R. Krauss "Composition-control of magnetron-sputter-deposited $(Ba_xSr_{1-x})Ti_{1+y}O_{3+z}$ thin films for voltage tunable devices". *Applied Physics Letters*, Vol. 76, pp. 625-627 (2000)

[4] W. J. Kim, W. Chang, S. B. Qadri, J. M. Pond, S. W. Kirchoefer, J. S. Horwitz, D. B. Chrisey "Structural and microwave properties of (Ba, Sr)$TiO_3$ films grown by pulsed laser deposition". *Applied Physics A*, Vol. 70, pp. 313-316 (2000)

[5] W. J. Kim, W. Chang, S. B. Qadri, J. M. Pond, S. W. Kirchoefer, D. B. Chrisey and J. S. Horwitz "Microwave properties of tetragonally distorted $(Ba_{0.5}Sr_{0.5})TiO_3$ thin films". *Applied Physics Letters*, Vol. 76, pp. 1185-1187 (2000)



Pao Yue-kong Library
PolyU • Hong Kong

[6] A. Outzourhit, J. U. Trefny, T. Kito, B. Yarar, A. Naziripour and A. M. Hermann "Fabrication and characterization of $Ba_{1-x}Sr_xTiO_3$ tunable thin film capacitors". *Thin Solid Films*, Vol. 259, pp. 218-224 (1995)

[7] W. Chang, C. M. Gilmore, W. J. Kim, J. M. Pond, S. W. Kirchoefer, S. B. Qadri, D. B. Chirsey and J. S. Horwitz "Influence of strain on microwave dielectric properties of (Ba, Sr)$TiO_3$ thin films". *Journal of Applied Physics*, Vol. 87, pp. 3044-3049 (2000)

[8] A. Naziripour, A. Outzourhit, J. U. Trefny, Z. H. Zhang, F. Barnes, J. Cleckler and A. M. Hermann "Fabrication of $Ba_{1-x}Sr_xTiO_3$ tunable capacitors with $Tl_2Ba_2Ca_1Cu_2O_x$ electrodes". *Physica C*, Vol. 233, pp. 387-394 (1994)

[9] C. S. Hwang "(Ba, Sr)$TiO_3$ thin films for ultra large scale dynamic random access memory. A review on the process integration". *Materials Science and Engineering B*, Vol. 56, pp. 178-190 (1998)

[10] D. Roy and S. B. Krupanidhi "Excimer laser ablated barium strontium titanate thin films for dynamic random access memory applications". *Applied Physics Letters*, Vol. 62, pp. 1056-1058 (1993)

[11] J. C. Shin, C. S. Hwang and H. J. Kim "Electrical conduction properties of sputter-grown (Ba, Sr)$TiO_3$ thin films having $IrO_2$ electrodes". *Applied Physics Letters*, Vol. 76, pp. 1609-1611 (2000)

[12] R. E. Jones, Jr., P. Zurcher, P. Chu, D. J. Taylor, Y. T. Lii, B. Jiang, P. D. Maniar and S. J. Gillespie "Memory applications based on ferroelectric and high-permittivity dielectric thin films". *Microelectronic Engineering*, Vol. 29, pp.

3-10 (1995)

[13] J. S. Horwitz, W. Chang, W. Kim, S. B. Qadri, J. M. Pond, S. W. Kirchoefer and D. B. Chrisey "The effect of stress on the microwave dielectric properties of $Ba_{0.5}Sr_{0.5}TiO_3$ thin films". *Journal of Electroceramics*, Vol. 4, pp. 357-363 (2000)

[14] T. Tsurumi, Y. Yamamoto, H. Kakemoto, S. Wada, H. Chazono and H. Kishi "Dielectric properties of $BaTiO_3$-$BaZrO_3$ ceramics under a high electric field". *Journal of Materials Research,* Vol. 17, pp. 755-759 (2002)

[15] J. F. Nye, *Physical properties of crystals: their representation by tensors and matrices*. Oxford university press, London (1957)

[16] K. Uchino, *Ferroelectric Devices.* Marcel Dekker, Inc., New York (2000)

[17] H. Landolt and R. Bornstein, *Numerical data and functional relationships in science and technology. New series, Group III, Crystal and solid state physics : volume 16, Revised, updated and extended edition of volumes III/3 and III/9, Ferroelectrics and related substances : subvolume A, Oxides*. Berlin ; New York : Springer-Verlag, New York (1981)

[18] Y. Gim, T. Hudson, Y. Fan, C. Kwon, A. T. Findikoglu, B. J. Gibbons, B. H. Park and Q. X. Jia "Microstructure and dielectric properties of $Ba_{1-x}Sr_xTiO_3$ films grown on $LaAlO_3$ substrates". *Applied Physics Letters*, Vol. 77, pp. 1200-1202 (2000)

[19] B. A. Baumert, L. H. Chang, A. T. Matsuda, C. J. Tracy, N. G. Cave, R. B. Gregory and P. L. Fejes "A study of barium strontium titanate thin films for use

in bypass capacitors". *Journal of Materials Research*, Vol. 13, pp. 197-204 (1998)

[20] J. S. Lee, J. S. Park, J. S. Kim, J. H. Lee, Y. H. Lee and S. R. Hahn "Preparation of $(Ba,Sr)TiO_3$ thin films with high pyroelectric coefficients at ambient temperatures". *Japanese Journal of Applied Physics, Part 2 (Letters)*, Vol. 38, pp. L574-L576 (1999)

[21] W. Yang, A. M. Chang and B. C. Yang "$Ba_{0.65}Sr_{0.35}TiO_3$ pyroelectric ceramics prepared by microwave sintering". *Journal of Infrared and Millimeter Waves*, Vol. 21, pp. 171-174 (2002)

[22] T. Y. Tseng "$(Ba, Sr)TiO_3$ thin films: preparation, properties and reliability". *Ferroelectrics*, Vol. 232, pp. 1-13 (1999)

[23] W. Chang, J. S. Horwitz, A. C. Carter, J. M. Pond, S. W. Kirchoefer, C. M. Gilmore and D. B. Chrisey "The effect of annealing on the microwave properties of $Ba_{0.5}Sr_{0.5}TiO_3$ thin films". *Applied Physics Letters*, Vol. 74, pp. 1033-1035 (1999)

[24] J. J. Carr, *Microwave & wireless communications technology*. Newnes, USA (1997)

[25] F. W. Van Keuls, R. R. Romanofsky, D. Y. Bohman and F. A. Miranda "Influence of the biasing scheme on the performance of $Au/SrTiO_3/LaAlO_3$ thin film conductor/ferroelectric tunable ring resonators". *10th International Symposium on Integrated Ferroelectrics*, Colorado Springs Monterey, California, March 1-4, 1998, pp. 363-372 (1998)

[26] P. Padmini, T. R. Taylor, M. J. Lefevre, A. S. Nagra, R. A. York and J. S. Speck "Realization of high tunability barium strontium titanate thin films by rf magnetron sputtering". *Applied Physics Letters*, Vol. 75, pp. 3186-3188 (1999)

[27] E. J. Cukauskas, S. W. Kirchoefer and J. M. Pond "Low-loss $Ba_{0.5}Sr_{0.5}TiO_3$ thin films by inverted cylindrical magnetron sputtering". *Journal of Applied Physics*, Vol. 88, pp. 2830-2835 (2000)

[28] Z. Jin, A. Tombak, J. P. Maria, B. Boyette, G. T. Stauf, A. I. Kingon and A. Mortazawi "Microwave characterization of thin film BST materials using a simple measurement technique". *Proceedings of 2002 International Microwave Symposium (MTT 2002)*, pp. 1201-1204 (2002)

[29] S. S. Gevorgian, T. Martinsson, P. L. J. Linner and E. L. Kollberg "CAD models for multilayered substrate interdigital capacitors". *IEEE Transactions on Microwave Theory and Techniques*, Vol. 44, pp. 896-904 (1996)

[30] S. Gevorgian, E. Carlsson, S. Rudner, L. D. Wernlund, X. Wang and U. Helmersson "Modelling of thin-film HTS/ferroelectric interdigital capacitors". *IEE Proceedings-Microwaves, Antennas and Propagation*, Vol. 143, pp. 397-401 (1996)

[31] S. S. Gevorgian, L. J. P. Linner, and E. L. Kollberg "CAD models for shielded multilayered CPW". *IEEE Transactions on Microwave Theory and Techniques*, Vol. 43, pp. 772-779 (1995)

[32] M. A. Chaudhry and R. Schinzinger "A conformal mapping analysis of polygonal planar resistors with curved boundaries". *Hybrid Circuits*, Vol. 27, pp.

21-24 (1992)

[33] F. Yan, P. Bao, Z. G. Zhang, J. S. Zhu, Y. Wang, H. L. W. Chan and C. L. Choy "Dielectric properties of $(Ba_{0.5}Sr_{0.5})TiO_3$ thin films". *Thin Solid Films*, Vol. 357, pp. 184-187 (2000)

[34] I. Lubomirsky, T. Y. Wang, F. DeFlaviis, O. M. Stafsudd "Dielectric relaxation in ceramics with an intragrain concentration gradient". *Journal of the European Ceramic Society*, Vol. 22, pp. 1263-1267 (2002)

[35] S. B. Majumder, M. Jain, A. Martinez, R. S. Katiyar, F. W. Van Keuls and F. A. Miranda "Sol-gel derived grain oriented barium strontium titanate thin films for phase shifter applications". *Journal Applied Physics*, Vol. 90, pp. 896-903 (2001)

[36] B. T. Lee and C. S. Hwang "Influences of interfacial intrinsic low-dielectric layers on the dielectric properties of sputtered (Ba, Sr)$TiO_3$ thin films". *Applied Physics Letters*, Vol. 77, pp. 124-126 (2000)

[37] A. F. Devinshire "Theory of barium titanate (Part 1)". *Philosophical Magazine*, Vol. 40, pp.1040-1048 (1949)

[38] K. M. Johnson "Variation of dielectric constant with voltage in ferroelectrics and its application to parametric devices". *Journal of Applied Physics*, Vol. 33, pp. 2826-2831 (1962)

[39] P. K. Baumann, D. Y. Kaufman, J. Im, O. Auciello, S. K. Streiffer, R. A. Erck and J. Giumarra "MOCVD $(Ba_xSr_{1-x})Ti_{1+y}O_{3+z}$ (BST) thin films for high frequency tunable devices". *Integrated Ferroelectrics*, Vol. 34, pp. 255-262 (2001)

[40] A. Tombak, J. P. Maria, F. Ayguavives, Z. Jin, G. T. Stauf, A. I. Kingon and A. Mortazawi "Tunable barium strontium titanate thin film capacitors for rf and microwave applications". *Microwave and Wireless Components Letters,* Vol. 12, pp. 3-5 (2002)

[41] Y. Liu, A. S. Nagra, E. G. Erker, P. Periaswamy, T. R. Taylor, J. Speck and R. A. York "$BaSrTiO_3$ interdigitated capacitors for distributed phase shifter applications". *IEEE Microwave and Guided Wave Letters*, Vol. 10, pp. 448-450 (2000)

[42] C. Doan, *Introduction to on-wafer characterization at microwave frequencies.* http://www.macs.ece.mcgill.ca/~ktsang/downloads/On-Wafer_Characterization.pdf., University of California, Berkeley

[43] K. Chang, *Microwave Ring Circuits and Antennas. A* Wiley-Interscience publication, USA (1996)

[44] L. H. Hsieh and K. Chang "Compact dual-mode elliptic function bandpass filter using a single ring resonator with one coupling gap". *Electronics Letters*, Vol. 36, pp. 1626-1627 (2000)

[45] E. Semouchkina, W. Cao and M. Lanagan "High frequency permittivity determination by spectra simulation and measurement of microstrip ring resonators". *Electronics Letters*, Vol. 36, pp. 956-958 (2000)

[46] E. Hammerstad "Equations for microstrip circuit design". *5th European Microwave Conference*, Hamburg, West Germany, 1-4 Sept., 1975, pp. 268-272 (1975)

[47] *IE3D user's manual.* Zeland Software, Inc., USA (2001)

[48] J. X. Zheng "Three-dimensional electromagnetic simulation of electronic circuits of general shape". *International Journal of Microwave and Millimeter-Wave Computer-Aided Engineering*, Vol. 4, pp. 384-395 (1994)

[49] F. W. Van Keuls, R. R. Romanofsky, D. Y. Bohman, M. D. Winters, F. A. Miranda, C. H. Mueller, R. E. Treece, T. V. Rivkin and D. Galt "($YBa_2Cu_3O_{7-\delta}$, Au)/$SrTiO_3$/$LaAlO_3$ thin film conductor/ferroelectric coupled microstripline phase shifters for phased array applications". *Applied Physics Letters*, Vol. 71, pp. 3075-3077 (1997)

[50] F. W. Van Keuls, R. R. Romanofsky and F. A. Miranda "Several microstrip-based conductor/thin film ferroelectric phase shifter designs using ($YBa_2Cu_3O_{7-\delta}$, Au)/$SrTiO_3$/$LaAlO_3$ structures". *Integrated Ferroelectrics*, Vol. 22, pp. 893-901 (1998)

# List of publications

Journal papers

[1] Y. L. Cheng, Y. Wang, H. L. W. Chan and C. L. Choy "Preparation and characterization of (Ba,Sr)$TiO_3$ thin films using interdigital electrodes". *Microelectronics Engineering*, Vol. 66, pp.872-879 (2003)

[2] Y. Wang, Y. L. Cheng, Y. W. Zhang, H. L. W. Chan and C. L. Choy "Dielectric behavior of lead zirconate titanate ceramics with coplanar electrodes". *Materials Science and Engineering B*, Vol. 99, pp. 79-82 (2003)

[3] Y. Wang, H. L. W. Chan, Y. L. Cheng and C. L. Choy "Highly oriented $SrTiO_3$ thin film on Si deposited by magnetron sputtering". *Journal of Vacuum Science and Technology A*, Vol. 21, pp. 825-82 (2003)

[4] Y. Wang, N. Chong, Y. L. Cheng, H. L. W. Chan and C. L. Choy "Dependence of capacitance on electrode configuration for ferroelectric films with interdigital electrodes". *Microelectronic Engineering*, Vol. 66, pp. 880-886 (2003)

[5] Y. L. Cheng, N. Chong, Y. Wang, J. Z. Liu, H. L. W. Chan and C. L. Choy "Microwave characterization of BST thin films on LAO interdigital capacitor". submitted to *Integrated Ferroelectrics*

# Appendix

Based on Gevorgian's model, a program was developed for calculating the relative permittivity of the thin film from the capacitance of an interdigital capaitance.

Program in Mathematica:

```
(* CAD models for multilayered substrate IDE *)

KC[x_] := EllipticK[x]
KP[x_] := KC[Sqrt[1-x^2]]
Kratio[x_] := SetAccuracy[KC[x] / KP[x], 100]

(* Cn *)
k0[w_, s_] := SetAccuracy[w / (w + s), 100]
kn[w_, s_, h_] :=
SetAccuracy[Sinh[Pi * w / h / 4] / (Sinh[Pi * (w + s) / h / 4] ) *
  Sqrt[((Cosh[Pi * (w + s) / h / 4]) ^2 + (Sinh[Pi * (w + s) / h / 4]) ^2) /
    ((Cosh[Pi * w / h / 4]) ^2 + (Sinh[Pi * (w + s) / h / 4]) ^2)], 100]

Cn[l_, n_, w_, s_, e1_, e2_, e3_, h1_, h2_, h3_] :=
    SetAccuracy[(n - 3) * (8.854 * 10^-6) * l * (Kratio[k0[w, s]] +
                (e1 - 1) / 2 * Kratio[kn[w, s, h1]] +
                (e2 - e1) / 2 * Kratio[kn[w, s, h2]] +
                (e3 - 1) / 2 * Kratio[kn[w, s, h3]]), 100]
```

```
(* C3 *)
k03[w_, s_, w3_] := SetAccuracy[ w / (w + 2 * s) *
 Sqrt[((w / 2 + w3 + s) ^2 - (w / 2 + s) ^2) /
      ((w3 + w / 2 + s) ^2 - (w / 2) ^2)], 100]

kn3[w_, s_, h_, w3_] := SetAccuracy[
        Sinh[Pi * w / h / 4] / (Sinh[Pi * (w / 2 + s) / h / 2]) *
        Sqrt[
   ((Sinh[Pi * (w3 + w / 2 + s) / h / 2]) ^2 - (Sinh[Pi * (w / 2 + s) / h / 2]) ^2) /
    ((Sinh[Pi * (w3 + w / 2 + s) / h / 2]) ^2 - (Sinh[Pi * w / h / 4]) ^2)], 100]

C3[l_, n_, w_, s_, e1_, e2_, e3_, h1_, h2_, h3_, w3_] :=
SetAccuracy[
        4 * l * (8.854 * 10^-6) * 1 / Kratio[k03[w, s, w3]] *
  (1 + 1 / Kratio[k03[w, s, w3]] * (
                (e1 - 1) / 2 * Kratio[kn3[w, s, h1, w3]] +
                (e2 - e1) / 2 * Kratio[kn3[w, s, h2, w3]] +
                (e3 - 1) / 2 * Kratio[kn3[w, s, h3, w3]])), 100]


(* Cend *)
k0e[wy_, sy_, x_] := SetAccuracy[x / (x + sy) *
            Sqrt[((wy + x + sy) ^2 - (x + sy) ^2) /
     ((wy + x + sy) ^2 - x^2)], 100]

kne[wy_, sy_, h_, x_] := SetAccuracy[
        Sinh[Pi * x / h / 2] / (Sinh[Pi * (x + sy) / h / 2] ), 100]

Ce[n_, w_, e1_, e2_, e3_, h1_, h2_, h3_, sy_, wy_, x_] :=
SetAccuracy[
        2 * n * w * (2 + Pi) * (8.854 * 10^-6) * (Kratio[k0e[wy, sy, x]] +
                (e1 - 1) / 2 * Kratio[kne[wy, sy, h1, x]] +
                (e2 - e1) / 2 * Kratio[kne[wy, sy, h2, x]] +
                (e3 - 1) / 2 * Kratio[kne[wy, sy, h3, x]]), 100]
```

```
wp[w_, t_] := w + (t / Pi) * (1 + Log[4 * Pi * w / t])

CT[t_, l_, n_, w_, s_, e1_, e2_, e3_, h1_, h2_, h3_, w3_, sy_,
  wy_, x_] :=
   Cn[l, n, wp[w, t], s, e1, e2, e3, h1, h2, h3] +
   C3[l, n, wp[w, t], s, e1, e2, e3, h1, h2, h3, w3] +
   Ce[n, wp[w, t], e1, e2, e3, h1, h2, h3, sy, wy, x]

CT1[l_, n_, w_, s_, e1_, e2_, e3_, h1_, h2_, h3_] :=
N[CT[0.1, l, n, w, s, e1, e2, e3, h1, h2, h3, w, 10 * w, 100 * w, 0], 16]

CT[0.3, 501, 60, 7.6, 7.6, 24.5, 24.5, 265, 500, 500, 0.3, 7.6,
 7.6, 100, 0]
5.31254735210731515726578777503164019435644149780273437500000000\
 000000000000000000000000000000000
Ce[60, wp[7.6, 0.3], 24.5, 24.5, 265, 500, 500, 0.3, 7.6, 15.2,
 1.9]
0.50192851999741738833193949176347814500331878662109375000000000\
 000000000000000000000000000000000
C3[500, 60, wp[7.6, 0.3], 7.6, 24.5, 24.5, 1, 500, 500, 0.3,
 7.6]
0.24714527754747758758746556395635707303881645202636718750000000\
 0000000000000000000000000000000000
CT[5, 100, 50, 10, 10, 12.5, 12.5, 1, 500, 500, 1, 10, 10, 100,
 1]
0.47892399776858937329726551013209245866164565086364746093750000\
 000000000000000000000000000000000
CT[0.3, 1500, 12, 28, 16, 24.5, 500, 1, 500, 30, 10, 16, 16,
 100, 7]
40.8158507750895926946554936876054853200912475585937500000000000\
 0000000000000000000000000000000000
(* PLT10/ZrO/SiO/Si Song's *)
CT[0.1, 1446, 40, 10, 20, 11.9, 6670, 1, 500, 0.3, 0.7, 40,
 50, 1000, 0]
50.6480784513642068311867205920862033963203430175781250000000000\
 0000000000000000000000000000000000
CT1[371, 80, 4, 4, 5.7, 12, 1, 500, 2, 1.5]
1.151606730478411
CT1[1000, 200, 4, 4, 5.7, 5.7, 12, 300, 200, 1]
8.048151490333307
CT1[371, 80, 4, 4, 5.7, 22, 1, 300, 1.8, 1]
1.81009344397686
```

```
CT1[1440, 60, 20, 15, 5.7, 22, 1, 300, 1, 1]
2.882576967671854
CT[0.1, 620, 44, 30, 20, 11.9, 6670, 1, 500, 0.7, 10, 30, 50,
 1000, 0]
53.21426677294759910452626172627788037061691284179687500000000000\
 0000000000000000000000000000000000
Plot[CT[0.1, 620, 44, 30, 20, 11.9, e, 1, 500, 0.7, 10, 30, 50,
  1000, 0], {e, 1000, 10000}, PlotDivision -> 10, Frame -> True,
 GridLines -> Automatic]
```

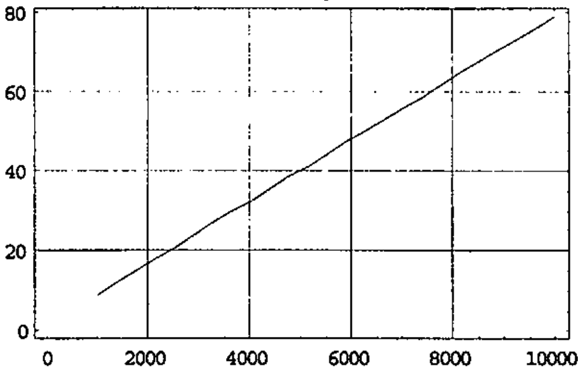


```
- Graphics -
(* BST on LAO *)
CT[0.35, 925, 21, 5, 2, 24.5, 387, 1, 500, 0.3, 1, 5, 55, 20,
 0]
10.06501562086418366526174850150709971785545349121093750000000000\
 0000000000000000000000000000000000
Plot[{CT[0.1, 1446, 80, 10, 5, 24.5, e, 1, 500, 1, 10, 10, 50, 1000, 0],
  CT[0.1, 1446, 80, 10, 5, 24.5, e, 1, 500, 0.5, 10, 10, 50, 1000, 0],
  CT[0.1, 1446, 80, 10, 5, 24.5, e, 1, 500, 0.15, 10, 10, 50, 1000, 0]},
 {e, 20, 1000}, PlotDivision -> 10, Frame -> True,
 GridLines -> Automatic, PlotRange -> {-5, 100}]
```

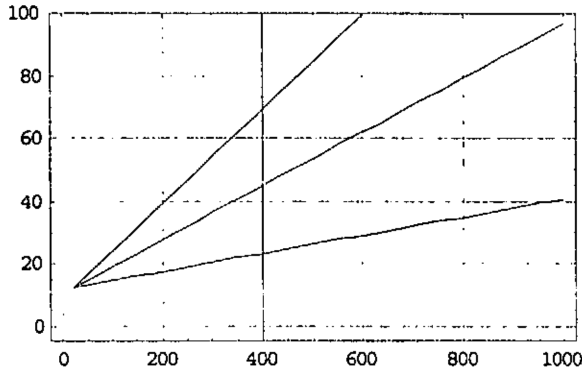


```
- Graphics -
```

```
Plot[{CT[0.1, 1000, 200, 4, 4, 24.5, 210, 1, 500, h, 10, 4, 10, 200, 1],
  CT[0.1, 1000, 200, 2, 2, 24.5, 210, 1, 500, h, 10, 4, 10, 200, 1],
  CT[0.1, 1000, 200, 10, 10, 24.5, 210, 1, 500, h, 10, 4, 10, 200, 1]},
 {h, 0.1, 4}, PlotDivision -> 10, Frame -> True,
 GridLines -> Automatic, PlotRange -> {-5, 175}]
```

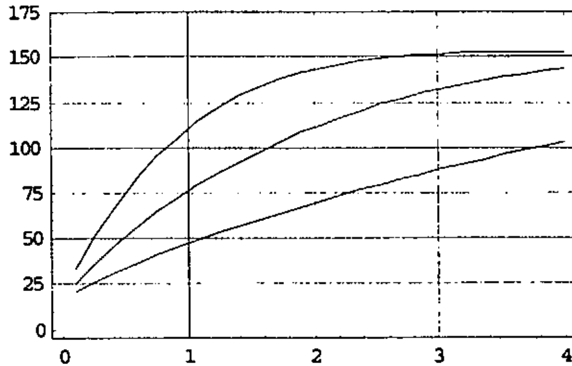


```
- Graphics -
Plot[{CT[0.3, 1500, 12, 28, 16, 24.5, 500, 1, 500, h, 10, 16,
   16, 100, 7], CT[0.3, 1500, 12, 10, 16, 24.5, 500, 1, 500, h,
   10, 16, 16, 100, 7], CT[0.3, 1500, 12, 5, 16, 24.5, 500, 1,
   500, h, 10, 16, 16, 100, 7]}, {h, 0.1, 30}, PlotDivision -> 5,
 Frame -> True, GridLines -> Automatic]
SetAccuracy::accsm :
 Requested SetAccuracy 100 would result in a precision smaller
   than $MinPrecision; bounding by $MinPrecision instead.
SetAccuracy::accsm :
 Requested SetAccuracy 100 would result in a precision smaller
   than $MinPrecision; bounding by $MinPrecision instead.
SetAccuracy::accsm :
 Requested SetAccuracy 100 would result in a precision smaller
   than $MinPrecision; bounding by $MinPrecision instead.
General::stop : Further output of
   SetAccuracy::accsm will be suppressed during this calculation.

- Graphics -
Plot[CT[0.3, 1500, 12, 10, 10, 24.5, 500, 1, 500, h*10, 10,
   16, 16, 100, 7], {h, 0.5, 1.5}, PlotDivision -> 5, Frame -> True,
 GridLines -> Automatic]
```

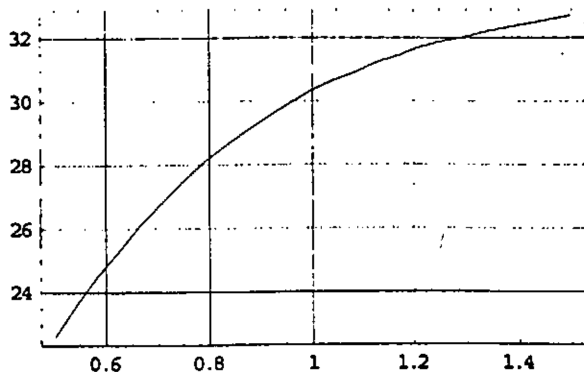

- Graphics -

```
Plot[{CT[0.3, 1500, 60, 10, 10, 24.5, 265, 1, 500, 0.3, 10, 10,
    10, 100, x*10], CT[0.3, 1500, 60, 10, 10, 24.5, 265, 1, 500,
    0.3, 10, 10, 10, 100, 0],
  CT[0.3, 1500, 60, 10, 10, 24.5, 50, 1, 500, 0.3, 10, 10, 10,
    100, x*10], CT[0.3, 1500, 60, 10, 10, 24.5, 50, 1, 500, 0.3,
    10, 10, 10, 100, 0]}, {x, 0, 1}, Frame -> True,
 PlotRange -> {7, 14.5}]
```

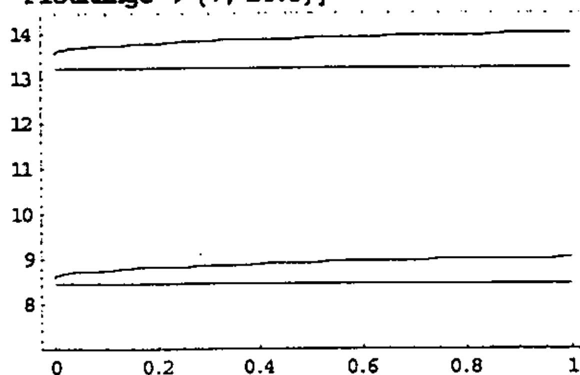

- Graphics -